

Diss. ETH No. 16490

# Modeling and Control of Pressure-Wave Supercharged Engine Systems

A dissertation submitted to the  
SWISS FEDERAL INSTITUTE OF TECHNOLOGY  
ETH ZURICH

for the degree of  
Doctor of Technical Sciences

presented by  
Peter Spring  
Dipl. Masch.-Ing. ETH

born 2 June 1973  
citizen of Reutigen BE

accepted on the recommendation of  
Prof. Dr. L. Guzzella, examiner  
Prof. Dr. L. Eriksson, co-examiner  
Prof. Dr. J. Piechna, co-examiner

2006

contact: [peter.spring@alumni.ethz.ch](mailto:peter.spring@alumni.ethz.ch)

L<sup>A</sup>T<sub>E</sub>X2 $\epsilon$

page size: DIN A4

documentclass: extbook

standard character size: 14 pt

packages: amsmath, amssymb, xspace,  
float, natbib, apalike, psfrag, graphicx, epsfig,  
units, array, textcomp, color, longtable,  
multicol, babel, ifthen, caption,  
makeidx, hyperref

Peter Spring

2006

”It’s not nearly as simple as we thought. – It never is.”

*John. B. Heywood*

To Franziska, with love



## Preface

This thesis is based on my research performed at the Measurement and Control Laboratory (IMRT) of the Swiss Federal Institute of Technology (ETH) in Zurich between 2000 and 2006. It was carried out with the financial support of the Swiss Department of Energy and Robert Bosch GmbH, Germany, and hardware support from Robert Bosch GmbH and from Swissauto Wenko AG, Switzerland.

First of all, I wish to thank my advisor, Professor Dr. Lino Guzzella, for the initiation of the project and for the support throughout the course of this work. Sincere thanks are extended to Dr. Chris Onder for his helpful advice and valuable discussions.

Furthermore I would like to thank Professor Dr. Lars Eriksson for accepting to be my co-examiner, for his interest in my work, for providing me many hints and tools, and for being my host during my visit at the University of Linköping, Sweden.

A special thank you goes to Professor Dr. Janusz Piechna from the Warsaw University of Technology, Poland, for his invaluable support during our cooperation and for accepting to be my co-examiner.

I also thank all the people of the Swiss Department of Energy, Robert Bosch GmbH, and Swissauto Wenko AG who supported me during this work. Especially, my thanks go to Martin Pulfer, Dr. Rainer Ortmann, Dr. Thomas Frenz, Dr. Andreas Eichendorf, Martin Rauscher, Dr. Stephan Tafel, Urs Wenger, Beat Kohler, Hansruedi Jenni, Hanspeter Götti, Roger Martin, and Lucas Flückiger.

Moreover I want to thank Dr. Hansueli Hörler, Thomas Lutz, Andreas Mayer, Dr. Tom Bulaty, Dr. Dobrivoje Ninkovic, and Dr. Herbert Niessner for sharing their knowledge on pressure-wave superchargers and their suggestions for improvement.

I immensely appreciated the fellowship and the support of the entire staff of the Measurement and Control Laboratory. I especially thank Daniel Matter, Oskar Brachs, Hansueli Honegger, and Jan Prikryl for their help with the testbench hardware, Brigitte Rohrbach for reviewing the texts, and Claudia Wittwer for managing the administrative issues.

In particular I would like to name Dr. Daniel Brand, Dr. Simon Frei, Dr. Felix Weber, Dr. Alois Amstutz, Ognyan Yanakiev, Dr. André Niederberger, and Thomas Böhme for their friendship, encouragement, and the many fruitful discussions throughout the years.

However, my deepest thanks and greatest appreciation are reserved for my wife Franziska and for my parents. Their encouragement and support during all the years made this dissertation possible in the first place.

Zürich, February 2006

# Contents

|  |             |
|--|-------------|
| <b>Contents</b>  | <b>vii</b>  |
| <b>Abstract</b>  | <b>ix</b>   |
| <b>Zusammenfassung</b>                                       | <b>xi</b>   |
| <b>Nomenclature</b>  | <b>xiii</b> |
| <b>1 Introduction</b>  | <b>1</b>    |
| 1.1 Downsizing and Supercharging Concept . . . . .           | 1           |
| 1.2 Pressure-wave Supercharger . . . . .                     | 7           |
| 1.3 Model-based Control . . . . .                            | 11          |
| 1.4 Engine System . . . . .                                  | 11          |
| 1.5 Motivation . . . . .                                     | 20          |
| 1.6 Contributions . . . . .                                  | 20          |
| 1.7 Structure of the thesis . . . . .                        | 22          |
| <b>2 Engine System Modeling</b>                              | <b>23</b>   |
| 2.1 Receiver Model . . . . .                                 | 25          |
| 2.2 Flow Restriction Model . . . . .                         | 27          |
| 2.3 Intercooler Model . . . . .                              | 29          |
| 2.4 Engine Mass Flow Model . . . . .                         | 29          |
| 2.5 Engine Torque Model . . . . .                            | 30          |
| 2.6 Engine Outlet Temperature Model . . . . .                | 33          |
| <b>3 Pressure-wave Supercharger Modeling</b>                 | <b>35</b>   |
| 3.1 Finite-difference Modeling . . . . .                     | 37          |
| 3.1.1 Physics and Governing Equations . . . . .              | 37          |
| 3.1.2 Space-Time Discretization and Solving Scheme . . . . . | 40          |
| 3.1.3 Boundary Conditions . . . . .                          | 43          |
| 3.1.4 Pressure and Temperature Distributions . . . . .       | 49          |

|          |   |            |
|----------|---|------------|
| 3.1.5    | Sensitivity Analysis . . . . .                      | 51         |
| 3.1.6    | The Influence of Leakage . . . . .                  | 55         |
| 3.1.7    | Validation of the Finite-Difference Model . . . . . | 57         |
| 3.2      | Mean-Value Modeling . . . . .                       | 63         |
| 3.2.1    | Summary of Linear Wave Theory . . . . .             | 64         |
| 3.2.2    | Modeling the High-Pressure Part . . . . .           | 68         |
| 3.2.3    | Modeling EGR Effects . . . . .                      | 76         |
| <b>4</b> | <b>Closed-Loop Simulation</b>                       | <b>81</b>  |
| <b>5</b> | <b>Control System Design</b>                        | <b>87</b>  |
| 5.1      | Controller I . . . . .                              | 89         |
| 5.1.1    | Realization . . . . .                               | 89         |
| 5.1.2    | Verification . . . . .                              | 92         |
| 5.2      | Controller II . . . . .                             | 95         |
| 5.2.1    | Realization . . . . .                               | 96         |
| 5.2.2    | Verification . . . . .                              | 99         |
| 5.3      | Controller III . . . . .                            | 104        |
| <b>6</b> | <b>Conclusions and Outlook</b>                      | <b>105</b> |
| <b>A</b> | <b>Experiments</b>                                  | <b>109</b> |
| A.1      | Engine Test Rig . . . . .                           | 109        |
| A.2      | Reference Data . . . . .                            | 111        |
| <b>B</b> | <b>Derivation of the Euler Equations</b>            | <b>117</b> |
| <b>C</b> | <b>Basic Equations of the Linear Wave Theory</b>    | <b>121</b> |
| <b>D</b> | <b>The Speed of Sound</b>                           | <b>129</b> |
|          | <b>Bibliography</b>                                 | <b>131</b> |
|          | <b>Index</b>  | <b>138</b> |
|          | <b>Curriculum Vitae</b>                             | <b>141</b> |



# Abstract

This thesis analyzes the application of so-called pressure-wave superchargers (PWS) with spark-ignition (SI) engines. Traditionally, the torque of a gasoline engine has been controlled by throttling the intake air flow. With that method, the density of the charge and hence the mass which is aspirated by the engine is varied. While the method is cheap and has an excellent transient behavior, the efficiency of the engine decreases substantially for part-load operation. In practice, engines powering vehicles are very often operated under part-load conditions so that the resulting fuel consumption becomes high.

Many methods have been proposed to control the load without or with reduced throttling. A good way to increase the overall efficiency of an engine-vehicle system is to reduce the engine displacement and to use a supercharger. Today's standard supercharger is the turbocharger, where the enthalpy in the exhaust gas drives a compressor, which in turn raises the pressure in the intake manifold. In a pressure-wave supercharger, one-dimensional unsteady gas dynamical effects are used to transmit the enthalpy in the exhaust gas to the intake air by short-time direct contact of the fluids in narrow flow channels. Both the fast engine torque response and the high boost pressure over the entire engine speed range are reasons for favoring pressure-wave superchargers for present-day passenger-car applications.

Modern pressure-wave supercharging devices offer to arbitrarily set gas pocket valve position, cell-wheel speed, and the angle offset between air and gas casing. A multitude of cross-couplings towards the mass flows and particularly to the engine torque can be caused thereby.

During rapid transients, critical situations arise when large amounts of exhaust gas are recirculated over the charger from exhaust to intake manifolds. This causes the engine torque to drop sharply and thus severely affects the driveability of the vehicle. In order to prevent such situations, the actuators (throttles, valves, etc.) have to be controlled in a coordinated way.

Accurate models are required to simulate the steady-state and transient physical effects occurring in the charger and in the engine system.

A universally valid first-principle model is developed where a set

of Euler-type partial differential equations is numerically solved using a finite-difference method. One-dimensional unsteady gas dynamics in the cell wheel are simulated, taking into account such phenomena as leakage, heat transfer, friction, and varying actuator inputs. The validation with measurement data from a PWS-boosted engine shows an error of less than 5% in a large operating range.

A control-oriented model is then derived on the basis of that first-principle model. It is restricted to the simulation of the essential physical effects, but it saves considerable computational time. This static PWS model is implemented in a dynamic model in order to simulate the transient behavior of the entire engine system.

On the basis of these models, a new controller system is designed and experimentally verified. The controller prevents exhaust gas recirculation effects and causes the PWS to operate at optimal efficiency.

The future implementation of the control systems presented in this work will increase the acceptance of the fuel-efficient pressure-wave supercharged engines and thus help to reduce fuel consumption of passenger cars.

## Zusammenfassung

In der vorliegenden Arbeit wird der Einsatz von so genannten Druckwellenladern für Ottomotoren analysiert. Traditionell wird die Last von Benzinmotoren über eine Drossel im Ansaugtrakt eingestellt. So wird die Dichte im Einlasskrümmer und schliesslich der vom Motor angesaugte Massenstrom variiert. Diese Methode ist billig und weist ein vortreffliches dynamisches Verhalten auf, aber der Motorwirkungsgrad sinkt massgeblich im Teillastbetrieb. Personenwagen werden aber am häufigsten in der Teillast betrieben, was tiefe Wirkungsgrade beziehungsweise einen hohen Verbrauch bewirkt.

Zahlreiche Massnahmen sind vorgeschlagen worden, um Motoren nur teilgedrosselt oder ungedrosselt zu betreiben. Ein Konzept besteht darin, den Motor-Hubraum zu reduzieren und die Leistung über Aufladung zurück zu gewinnen. Heutzutage werden verbreitet Abgasturbolader eingesetzt, wobei die nach dem Auslasskrümmer im Rauchgas vorhandene Enthalpie dazu verwendet wird, einen Kompressor anzutreiben, welcher seinerseits die Frischluft im Einlasskrümmer verdichtet. Im Gegensatz dazu stehen in Druckwellenladern Rauchgas und Frischluft in direktem Kontakt. Die Enthalpieübertragung erfolgt durch einen gasdynamischen Prozess, wobei Druckwellen in den beiden Medien hin und her laufen. Aufgrund dieses Prinzips zeichnen sich Druckwellenlader durch ein gutes Ansprechverhalten und durch über den gesamten Betriebsbereich hohe Wirkungsgrade aus. Beides steigert die Fahrbarkeit beim Einsatz in Personenwagen.

Moderne Druckwellenladersysteme bieten die Möglichkeit, über drei unabhängige Stellglieder in den Prozess einzugreifen: Gastaschen-Zufluss-Ventil, Rotordrehzahl und Winkelversatz zwischen Luft- und Gasgehäuse lassen eine Vielzahl von Kombinationsmöglichkeiten zu, wie die Massenströme und schliesslich das Motordrehmoment zu beeinflussen sind.

Während hohen Lastsprüngen können dann kritische Situationen entstehen, wenn grosse Mengen an Rauchgas durch den Lader zurück in den Ansaugtrakt transportiert werden. Dieser Effekt, der als Abgasrezirkulation (AGR) bezeichnet wird, bewirkt einen markanten Drehmomenteinbruch und verschlechtert dadurch die Fahrbarkeit merklich. Durch eine koordinierte Betätigung der Steller sind aber solche Situationen vermeidbar.

Diese Arbeit befasst sich deshalb mit der Entwicklung von physikalischen Modellen, mit denen es möglich wird, sowohl stationäre als auch transiente Effekte von Motor und Lader simulieren zu können.

Einführend wird ein Modell vorgestellt, welches auf Grundprinzipien der Gasdynamik aufbaut. Die so genannten Eulergleichungen, ein Satz von partiellen Differentialgleichungen, werden mit Hilfe eines finite-Differenzen-Verfahrens numerisch gelöst. Das Modell berücksichtigt die eindimensionale Gasdynamik und auch Effekte wie Leckage, Wärmeübergang, Reibung und veränderliche Stellgrößen. Ein Vergleich mit Messresultaten von einem Motor mit Druckwellenlader zeigt, dass die Resultate über einen grossen Betriebsbereich innerhalb von 5% liegen.

Ausgehend von diesem finite-Differenzen-Modell wird ein vereinfachtes, regelungstechnisch orientiertes Mittelwertmodell abgeleitet. Der daraus resultierende verringerte Rechenaufwand ermöglicht den Einsatz dieses statischen Druckwellenlader-Modells in einer Simulationsumgebung, womit das dynamische Verhalten des gesamten Motorsystems nachgebildet werden kann.

Basierend auf diesen Modellen wird ein Regelkonzept entworfen und experimentell am Motor überprüft. Der Regler vermag die während Lastsprüngen auftretenden AGR-Effekte zu verhindern, und der Lader wird wirkungsgrad-optimal betrieben.

Die Implementierung der in dieser Arbeit präsentierten Regelsysteme wird die Akzeptanz von effizienten druckwellenaufgeladenen Motoren steigern und dadurch mithelfen, den Verbrauch von Personenzügen zu senken.

# Nomenclature

## Abbreviations, Acronyms, Names

|                 |  |
|-----------------|--|
| ACEA            | Association des Constructeurs Européens d'Automobiles<br>(European automobile manufacturers association) |
| BBC             | Brown Boveri Company (former name of<br>Asea Brown Boveri, ABB)  |
| BMEP            | brake mean effective pressure  |
| CI              | compression-ignited (engines)  |
| CO              | carbon oxides  |
| CX              | Comprex PWS  |
| DSC             | downsizing and supercharging concept   |
| DT <sub>1</sub> | first-order derivative lag element   |
| ECU             | electronic control unit  |
| EGR             | exhaust gas recirculation  |
| ETH             | Eidgenössische Technische Hochschule<br>(Swiss Federal Institute of Technology)                          |
| FDMdl           | finite-difference model  |
| GP              | gas pocket   |
| GPV             | gas pocket valve   |
| HC              | hydrocarbons   |
| HX              | Hyprex PWS <sup>1</sup>  |
| IC              | internal combustion  |
| MIMO            | multiple-input multiple-output   |
| MSC             | mechanical supercharger  |
| MVMdl           | mean-value model   |
| NEDC            | new European driving cycle   |
| NO              | nitrogen oxides  |

---

<sup>1</sup>HYPREX<sup>®</sup> is a Registered Trademark of SESA, Swissauto Engineering SA, Etagnières, Switzerland

|                 |  |
|-----------------|--|
| ODE             | ordinary differential equation                         |
| PWS             | pressure-wave supercharger                             |
| PWE             | pressure-wave exchanger                                |
| PT <sub>1</sub> | first-order lag element                                |
| rpm             | revolutions per minute                                 |
| SAVE            | small advanced vehicle engine (concept)                |
| SESA            | Swissauto Engineering Société Anonyme (company)        |
| Sc              | scavenging   |
| SI              | spark-ignited (engines)                                |
| SmILE           | small intelligent light and efficient engine (concept) |
| TC              | turbocharger   |
| Th              | throttle   |
| TWC             | three-way catalytic converter                          |
| Wenko           | company name (Wenger & Kohler)                         |
| WR              | wave rotor   |

## Symbols

Multiple occurrence of letters may be resolved in the context and by checking the subscripts.

| Symbol             | Description                      | Unit   |
|--------------------|----------------------------------|--|
| $a$                | speed of sound                   | m/s  |
| $A$                | cross-section (area)             | m <sup>2</sup>   |
| $(A/F)_s$          | stoichiometric air-to-fuel ratio | -  |
| $\overline{B}$     | vector of source terms           | kg/m <sup>3</sup> s ; kg/m <sup>2</sup> s <sup>2</sup> ; kg/m s <sup>3</sup> |
| $c$                | molar concentration              | -  |
| $c_p$              | constant pressure specific heat  | J/kg K   |
| $c_v$              | constant volume specific heat    | J/kg K   |
| $c_d$              | discharge coefficient            | -  |
| $c_{\text{frict}}$ | friction coefficient             | -  |
| $D$                | diameter                         | m  |
| $d$                | distance                         | m  |
| $E$                | energy                           | J  |
| $e$                | specific energy                  | J/kg   |
| $e_T$              | specific total energy            | J/kg   |
| $\overline{F}$     | vector of numerical streams      | kg/m <sup>2</sup> s ; kg/m s <sup>2</sup> ; kg/s <sup>3</sup>                |
| $F$                | force                            | N  |
| $f_{\text{frict}}$ | specific friction                | m/s <sup>2</sup>   |
| $H$                | height                           | m  |
| $H$                | enthalpy                         | J  |
| $h$                | specific enthalpy                | J/kg   |
| $j$                | counter                          | -  |
| $K_{\text{fr}}$    | flow restriction constant        | Pa <sup>2</sup> s <sup>2</sup> /kg <sup>2</sup> K                            |
| $k$                | constant                         |  |
| $L$                | length                           | m  |
| $M$                | momentum                         | Nm   |
| $m$                | mass                             | kg   |
| $n$                | rotational speed                 | rpm  |
| $n$                | counter                          | -  |
| $n$                | rotational speed                 | rpm  |
| $p$                | pressure                         | Pa   |

|                |                                  |   |
|----------------|----------------------------------|---|
| $Q$            | heat                             | J   |
| $q$            | specific heat                    | J/kg  |
| $R$            | specific gas constant            | J/kg K  |
| $Re$           | Reynolds number                  | -   |
| $r$            | radius                           | m   |
| $S$            | sensitivity                      | -   |
| $s$            | specific entropy                 | J/kg K  |
| $T$            | temperature                      | K   |
| $Tq$           | torque                           | Nm  |
| $t$            | time                             | s   |
| $u$            | velocity                         | m/s   |
| $u$            | system input vector              | -   |
| $U$            | internal energy                  | J   |
| $\overline{U}$ | vector of conservative variables | kg/m <sup>3</sup> ; kg/m <sup>2</sup> s ; kg/m s <sup>2</sup> |
| $V$            | volume                           | m <sup>3</sup>  |
| $V_d$          | displaced volume                 | m <sup>3</sup>  |
| $W$            | work                             | J   |
| $x$            | spatial dimensions               | m   |
| $x$            | rate or system state vector      | -   |
| $xx$           | (interpolation) ratio            | -   |
| $y$            | system output vector             | -   |
| $y$            | actuator opening indicator       | -   |
| $yy$           | (interpolation) ratio            | -   |
| $zz$           | (interpolation) ratio            | -   |
| $\alpha$       | angle                            | °   |
| $\beta$        | artificial viscosity parameter   | -   |
| $\Delta$       | difference                       | -   |
| $\eta$         | efficiency                       | -   |
| $\kappa$       | ratio of specific heats          | -   |
| $\lambda$      | air-to-fuel ratio                | -   |
| $\lambda_{ht}$ | heat transfer coefficient        | W/m <sup>2</sup> K  |
| $\Pi$          | pressure or entropy ratio        | -   |
| $\rho$         | density                          | kg/m <sup>3</sup>   |
| $\omega$       | rotational speed                 | rad/s   |
| $\partial$     | partial derivative (operator)    | -   |



## Subscripts

Subscripts denote components or refer to states in the control volumes after the corresponding component. Numbers in subscripts refer to the enumerations of receivers, channels, and throttles. Zero relates to nominal values.

### Subscript    Description

|         |   |
|---------|---|
| a       | air side  |
| a       | position  |
| air     | air   |
| amb     | ambient   |
| b       | position  |
| c       | close   |
| cas     | casing offset   |
| cell    | cell  |
| ch      | channel: cross-sectional area where fluid flows into and out of the PWS |
| che     | expansion pocket  |
| chg     | gas pocket channel  |
| conv    | convection  |
| cyl     | cylinder  |
| crit    | critical  |
| downstr | downstream  |
| d       | displaced   |
| D       | discharge   |
| EL      | expansion wave, moving towards the left                                 |
| ER      | expansion wave, moving towards the right                                |
| e       | engine  |
| e       | exhaust side  |
| eg      | exhaust gas   |
| egr     | recirculated exhaust gas  |
| em      | exhaust manifold  |
| FL      | full load   |
| fl      | fuel  |
| frict   | friction  |

|          |                                      |
|----------|--------------------------------------|
| gap      | gap (width)                          |
| gas      | gas (generally: fluid)               |
| geo      | geometric                            |
| gp       | gas pocket                           |
| gpv      | gas pocket valve                     |
| hpl      | high-pressure loop                   |
| ht       | heat transfer                        |
| hv       | (lower) heating value                |
| ic       | intercooler                          |
| im       | intake manifold                      |
| in       | input                                |
| L        | left-hand side                       |
| leak     | leakage                              |
| max      | maximum                              |
| me       | brake mean effective                 |
| mf       | fuel mean effective                  |
| min      | minimum                              |
| nom      | nominal                              |
| out      | output                               |
| OxCat    | oxidation catalytic converter        |
| o        | open                                 |
| PL       | part load                            |
| p        | piston                               |
| PolyExpo | polytropic exponent                  |
| pws      | pressure-wave supercharger           |
| R        | right-hand side                      |
| rec      | receiver: manifold, tube             |
| ref      | reference                            |
| restr    | restriction                          |
| rot      | (PWS) rotor                          |
| SL       | shock wave, moving towards the left  |
| SR       | shock wave, moving towards the right |
| s        | stoichiometric                       |
| s        | start                                |
| s        | stroke                               |

|       |                               |
|-------|-------------------------------|
| sc    | scavenging                    |
| th    | throttle                      |
| tot   | total                         |
| tq    | torque                        |
| T     | total                         |
| Temp  | temperature                   |
| TWC   | three-way catalytic converter |
| upstr | upstream                      |
| Velo  | velocity                      |
| vol   | volumetric                    |
| wall  | wall (of the cell)            |
| WOT   | wide open throttle            |
| z     | zone                          |

## Notational Conventions

### Derivatives

Time derivatives are represented by their respective fractions (Eq. (1)). The flow, which is a quantity transported through a certain area ( $A$ ) per time unit ( $dt$ ), is represented by an asterisk (Eq. (2)).

$$\frac{dx}{dt} \quad (1)$$

$$x^* = \frac{x_{A \rightarrow}}{dt} \quad (2)$$

### Initial capitalizations

Numbered devices such as *Receiver 1*, *Channel 2*, and *Throttle 2* are used as fixed terms and written with initial capitals. However, when they are used in subscripts, lower case initial letters are used to improve legibility.



## Chapter 1

# Introduction

In this chapter, the *downsizing and supercharging concept* is introduced, and the pressure-wave supercharger (PWS) is proposed as one possible device to boost internal combustion engines. The engine system and its actuators are specified and initial experiments are described which refer to the problems that motivated this research. The chapter highlights the main contributions of this research effort and details the organization of the text.

### 1.1 Downsizing and Supercharging Concept

Engine downsizing became one of the buzz phrases in Europe as soon as the European automobile manufacturers association (ACEA) made the commitment to reduce average carbon dioxide emissions to 140 grams per kilometer (g/km) for new passenger cars sold in Europe starting in 2008. Nowadays, passenger cars in urban areas are mostly operated under part-load conditions. In these operating conditions gasoline engines inherently suffer from a lower efficiency than compression-ignited engines since the load is controlled by throttling the engine's mass flow, i.e., by reducing the pressure in the intake manifold. This method is simple and entails excellent dynamic behavior, but it induces pumping losses (Heywood, 1988). Particularly for low loads the efficiency of the engine becomes very poor.

The three dominant parameters of the power production are constituted by the rotational speed of the engine, the engine displacement, and the intake manifold pressure. As the displaced volume directly

correlates with the friction losses, it has to be reduced for better efficiency. An engine concept resulting in the same nominal power as the standard engine requires either the pressure in the intake manifold or the rotational speed of the engine to be increased. Since high rotational speeds are not accepted well by consumers, the only practicable way is to increase the pressure before the engine. This approach is known as the *downsizing and supercharging concept*.

The potential of this concept has already been demonstrated experimentally in the *SmILE* engine concept (Guzzella and Martin, 1998; Guzzella et al., 2000) as well as later in several series production cars. In such an engine system, the maximum engine torque reduced by a smaller displaced volume is recovered by a higher density of the air mass flow of the engine. The efficiency of the downsized engine for a set of typical operating points, such as the European driving cycle (MVEG-95), is higher than that of the naturally aspirated engine with a similar maximum torque (see Fig. 1.1). Thus, the cumulative fuel consumption at the end of the cycle is lower.

Three main types of superchargers are in use today with the purpose of achieving a higher intake manifold pressure: mechanical superchargers (MSC), turbochargers (TC), and pressure-wave superchargers (PWS). Whereas MSC such as blowers, compressors, or pumps are driven by the crank shaft or by an electric motor, for TC and PWS some of the exhaust gas enthalpy is transmitted to the air mass flow entering the engine to raise the intake manifold pressure above the ambient level. For turbocharging, a turbine in the exhaust path is used to drive a radial compressor, which pumps air into the intake manifold. In contrast, the core of the PWS is the so-called cell wheel, a set of open-ended channels arranged on a rotor between two casings. During a cycle, a cell is passing the exhaust manifold, where the entering gas triggers a shock wave that runs through the cell and compresses the fresh air. This compressed air then leaves the cell in the direction of the intake manifold.

The essential advantages and drawbacks of the three types of chargers are summarized in Table 1.1 and explained in the following:

**Efficiency:** Pressure-wave superchargers (PWS) demonstrate a better downscaling behavior in terms of efficiency than turbochargers (TC) and mechanical superchargers (MSC). In the case

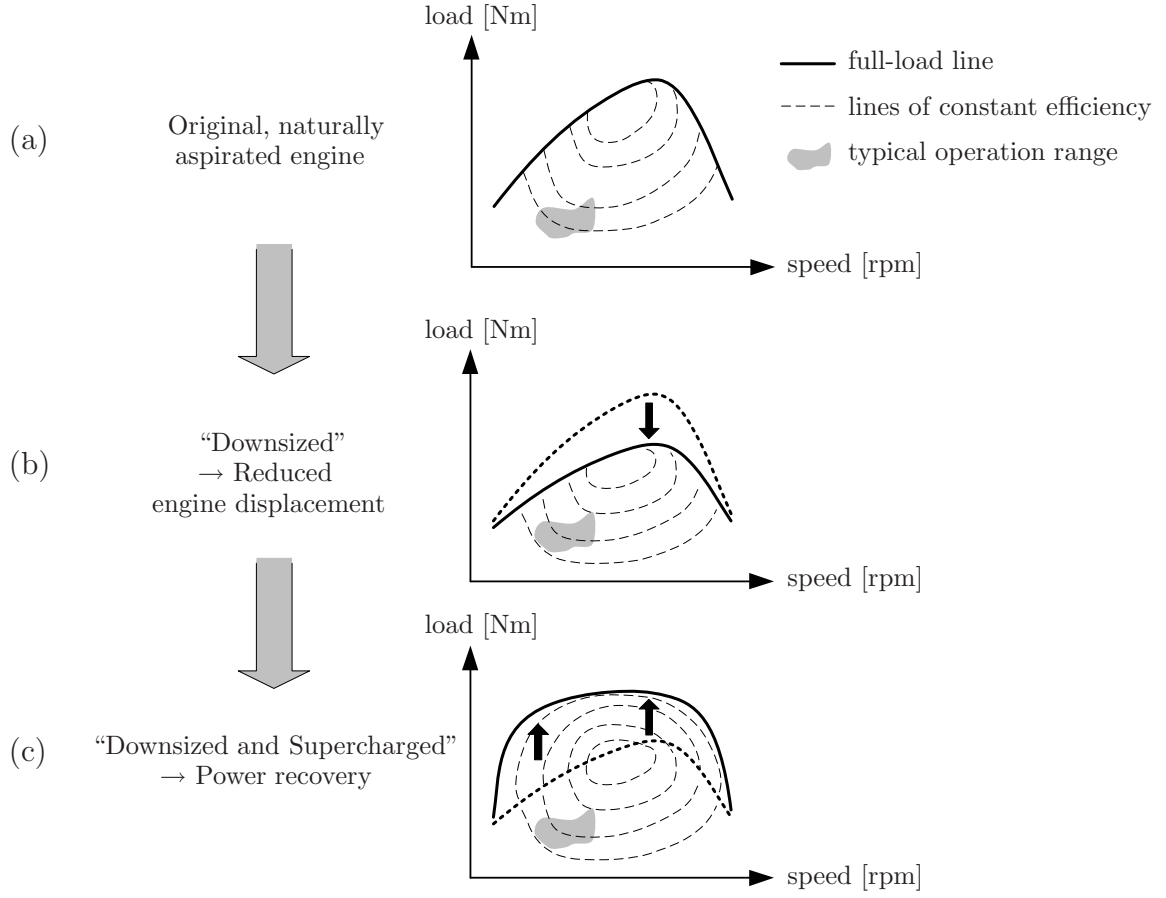


**Figure 1.1:** Downsizing and Supercharging Concept (DSC): The downsized and supercharged engine (c) achieves the same performance characteristics as the original, naturally aspirated engine with a higher engine displacement (a). But the cumulated fuel consumption during a typical driving cycle (“typical operation range”) is lower for (c) since the load/speed points lie on a higher efficiency level.

of a small engine displacement, leakage over the turbine and compressor is high compared to the mass flow. Due to these effects, a relatively high pressure in the exhaust manifold is required to generate the boost pressure. The higher pressure in the exhaust manifold in turn causes pumping losses for the spark-ignition engine, which result in increased fuel consumption. In contrast, the operating efficiency of a PWS is independent of the absolute value of the exhaust gas mass flow. Although a TC might have a higher efficiency at its best operating point, the average efficiency of a PWS over its entire operating range is higher. Secondly, the leakage losses are smaller than those of a TC since the rotational speed of the PWS is 10 to 20 times lower.

**Table 1.1:** Comparison of three possible supercharging devices: advantages (+) and drawbacks (−) of mechanical supercharger (MSC), turbocharger (TC), and pressure-wave supercharger (PWS). The EGR possibility could be ideal for compression-ignited engines.

| criterion   | MSC | TC | PWS |
|---|-----|----|-----|
| Downscaling-efficiency behavior                     | −   | −  | +   |
| Back pressure in exhaust manifold                   | +   | −  | −   |
| Part-load efficiency                                | +   | −  | +   |
| Torque reduction (crank shaft)                      | −   | +  | +   |
| Boost capacity at low engine speeds                 | +   | −  | +   |
| Driveability  | +   | −  | +   |
| Space demand/packaging                              | +   | +  | −   |
| Driving belt/connections                            | −   | +  | +   |
| Noise   | −   | +  | +   |
| Integrated catalytic converter                      | −   | −  | +   |
| Manufacturing costs                                 | −   | +  | ?   |
| Exhaust gas recirculation (EGR)                     | +   | +  | +/− |
| Back pressure sensitivity in the exhaust gas system | +   | +  | −   |
| Heat loss in the exhaust manifold                   | +   | −  | −   |
| Effort for applicability and controllability        | ?   | +  | −   |

Moreover, small TCs are subject to incidence losses (Traupel, 1988) since engine mass flow in spark-ignition engines may vary over a wide range, e.g. a factor of 30 and more. For mechanically supercharged engines the gross horsepower is reduced by the power used for driving the charger. More fuel is therefore used to produce the same power measured at the flywheel.

**Driveability:** A good driveability is attained for a fast dynamic torque response to a driver request, which manifests itself as a fast, steady, and smooth rising of the engine torque at low engine speeds. PWSs can produce high charging ratios even for small mass flows. Whereas the TC may suffer from a so-called “turbo



lag”, caused by the inertia of the turbine-compressor-shaft, leakage, and incidence losses, in a PWS the energy is transmitted instantaneously and directly from one fluid to the other. Since for MSC there is always “enough” power available, the boost capacity at low engine speeds is excellent. A combination of MSC and TC is favorable in terms of driveability, but it is a rather complex and expensive solution (Krebs et al., 2005).

**Packaging and drive:** The installation space demand of a PWS is approximately twice that of a TC. Moreover, a bigger exhaust manifold is necessary to reduce the cyclic pulsations caused by the engine valves (Endres, 1985; Mayer and Kirchhofer, 1985). However, the bigger exhaust manifold causes a higher heat transfer and thus a longer torque build-up time. One possibility to reduce pulsations is to integrate the three-way catalytic converter between the engine and the PWS. Similarly to MSC, earlier PWS used to be belt-driven from the crank shaft. The power demand for PWS – mainly to overcome bearing friction – is negligible in comparison to that required for MSC. However, the belt drive restricts the possible positioning of both devices. Modern PWS are either free-running or driven by an electric motor.

**Noise, catalytic converter, costs:** Experiments showed that noise, caused by pressure pulsations in the engine exhaust manifold is reduced by the PWS. The muffler in the exhaust system can be smaller. High conversion rates may be achieved when the PWS rotor itself is coated and used as catalytic converter (Mayer, 1988). The cost for manufacturing a PWS in the 1980s was about double that of a TC. This ratio was mainly due to the facts that, first, the rotor was fabricated by casting metal alloys and, second, the total costs for the TC development could be transferred to a much higher number of pieces produced. The higher price might be a continuing problem. But modern extruding technologies and ceramic materials might reduce the costs of the rotor. The reduction in the number of components such as mufflers and catalytic converters might increase the competitive position of the PWS

versus the TC.

**EGR, back pressure, control:** Exhaust gas recirculation (EGR) is a phenomenon often encountered in PWS since in a PWS fresh air and exhaust gas are in direct contact in the cell wheel (rotor). Depending on the concept, EGR has to be reduced (in spark-ignited engines) or forced (in compression-ignited engines). If it is controllable, the EGR feature therefore may be an advantage. Flow resistances in the *exhaust system*, i.e., where the exhaust gas is released to the ambient, have to be minimized since the pressure-wave process only works with very low back pressures. Moreover, the problem is exaggerated during the engine warm-up since much of the energy in the exhaust gas is transferred to the walls. As will be explained below, modern versions of PWS present an additional actuator to overcome that problem. Considering EGR, back-pressure problems, and the system complexity, the effort for application and control of pressure-wave supercharged engines might be higher than for turbocharged engines.

Still, the PWS seems to be the simplest and most preferable charging device for spark-ignition engines, if the engine displacement and the driveability are of major importance.

Although the PWS concept of boosting diesel engines lost out to turbocharged engines in the 1990s, the PWS with its potential and advantages keeps being proposed as a viable alternative. State-of-the-art PWSs are quite different from those of earlier times. Modern devices such as the HYPREX<sup>®</sup> PWS have been basically redesigned, and research in materials has made considerable progress as well. More freedom in the positioning of the device and maximum efficiency can be obtained over the entire operating range if the cell wheel is driven separately using an electric motor. The cold-start behavior is improved by the reduction of the angular offset between gas and air casing. Last but not least, substantial progress has been made in the last twenty years in providing powerful computers such that even complex on-board computations are now feasible in real time. They permit effects such as those appearing in a PWS to be predicted with sufficient accuracy such that they can be controlled.

## 1.2 The Pressure-wave Supercharger

In pressure-wave machines such as the PWS, pressure-wave exchanger (PWE) or wave-rotor (WR) energy is transferred between two gaseous fluid streams by short-time direct contact of the fluids in narrow flow channels, the so-called cells. Pressure-wave machines make use of the physical fact that if two fluids of different pressures are brought into direct contact, pressure equalization is faster than mixing. These devices use unsteady waves to produce steady flows of gas, whereby the stagnation pressure of the output stream may be higher than that of the input stream.

The idea of a direct pressure exchange has been investigated for almost a century (Akbari et al., 2004). First experiments of the wave rotor application as a topping unit for locomotive gas turbines made by Brown Boveri Company (BBC) were documented in the 1940s by Real (1946), Meyer (1947a,b), and Seippel (1942, 1946). Under the supervision of Kantrowitz and Berchtold (Berchtold and Gardiner, 1958; Berchtold, 1959; Berchtold and Gull, 1960), several units were successfully manufactured and tested on vehicle diesel engines from 1947 to 1955. As a result of their success, a co-operative program between those researchers and BBC was started in 1955. In the 1970s, the first prototypes were installed on truck engines (Wunsch, 1970; Doerfler, 1975), on passenger car diesel engines, on tractors, and even on bulldozers (Mayer, 1981; Jenny, 1993). BBC built up an impressive heterogeneous test fleet of passenger cars to collect statistical material: brands like Daimler Benz (1974, 1983), Opel (1979), Ford (1985), Volvo, BMW, Volkswagen (1986), Peugeot, and Ferrari are named in Hoepke (1988), Taussig and Hertzberg (1984), Hiereth (1989), and Janssens (1992). A massive test with a limited edition of 700 Opel Senator cars was started in 1985 (Gygax and Schneider, 1988). Those cars were equipped with COMPRES supercharged 2.3 liter diesel engines. The concept to charge diesel passenger cars was ready for series production (Schruf and Kollbrunner, 1984; Zehnder and Mayer, 1984). In 1987, when Asea and BBC merged to form ABB, the PWS activity was sold to Mazda. That company then produced 150,000 diesel passenger cars (“Mazda 626 Capella”) equipped with PWSs (Mayer, 1988; Zehnder et al., 1989; Tatsutomi et al., 1990).

Since the basic concept was not essentially improved any further,

the outdated PWS engine type series was abandoned when Mazda was taken over by Ford in 1994. All the rights were later transferred to Caterpillar. In collaboration with Comprex AG, a company founded by former employees of BBC, PWS have been used to boost diesel engines in order to lower  $NO_x$  emissions (Pauli and Amstutz, 1989; Amstutz, 1991). Recently, the COMPREX device has been installed on spark-ignition engines in order to test its usefulness to lower fuel consumption and to improve driveability of those engines also (Cortona, 2000; Soltic, 2000; Pfiffner, 2001; Weber, 2001; Weber et al., 2002; Spring et al., 2003). Swissauto Engineering SA (SESA), Etagnières, is the only company known to the author that is currently producing modern versions of PWSs. The new generation of wave rotors known as HYPREX<sup>®</sup> PWS is designed for small gasoline engine applications. Both their fast engine torque response and high boost pressure over the entire engine speed range are reasons for reconsidering PWSs for present-day passenger-car applications.

Modern PWS versions for automotive applications allow the angle between the casings at the left end (exhaust gas) and at the right end (fresh air) of the cell wheel to be varied within a certain range (see Fig. 1.2). This additional feature can guarantee a robust behavior under difficult operating conditions, such as those occurring during cold start and transient operations. Independently of engine speed, the PWS rotational speed can be adjusted by an electrical motor. In steady-state conditions this motor requires less than 150 W of electric power.

The PWS-engine system under consideration consists of a four-stroke spark-ignition engine (see also Appendix A), a PWS with gas pocket valve (GPV) (Croes, 1979; Mayer et al., 1990), two throttle bodies, and two catalytic converters (Weber and Guzzella, 2000) as depicted in Fig. 1.3. Throttle 2 (Th2) controls the engine torque in the naturally aspirated mode, whereas the gas pocket valve is the actuator in the supercharged mode in which Throttle 2 is fully open in order to avoid any throttling losses. Throttle 1 is used to control the pressure in Channel 1.

Basically, the pressure-wave process of the PWS can be divided into two main parts: the *high-pressure* and the *low-pressure part*. In the former, the exhaust gas enthalpy available in Channel 3 is used for supercharging the fresh air flowing into Channel 2. Leading a

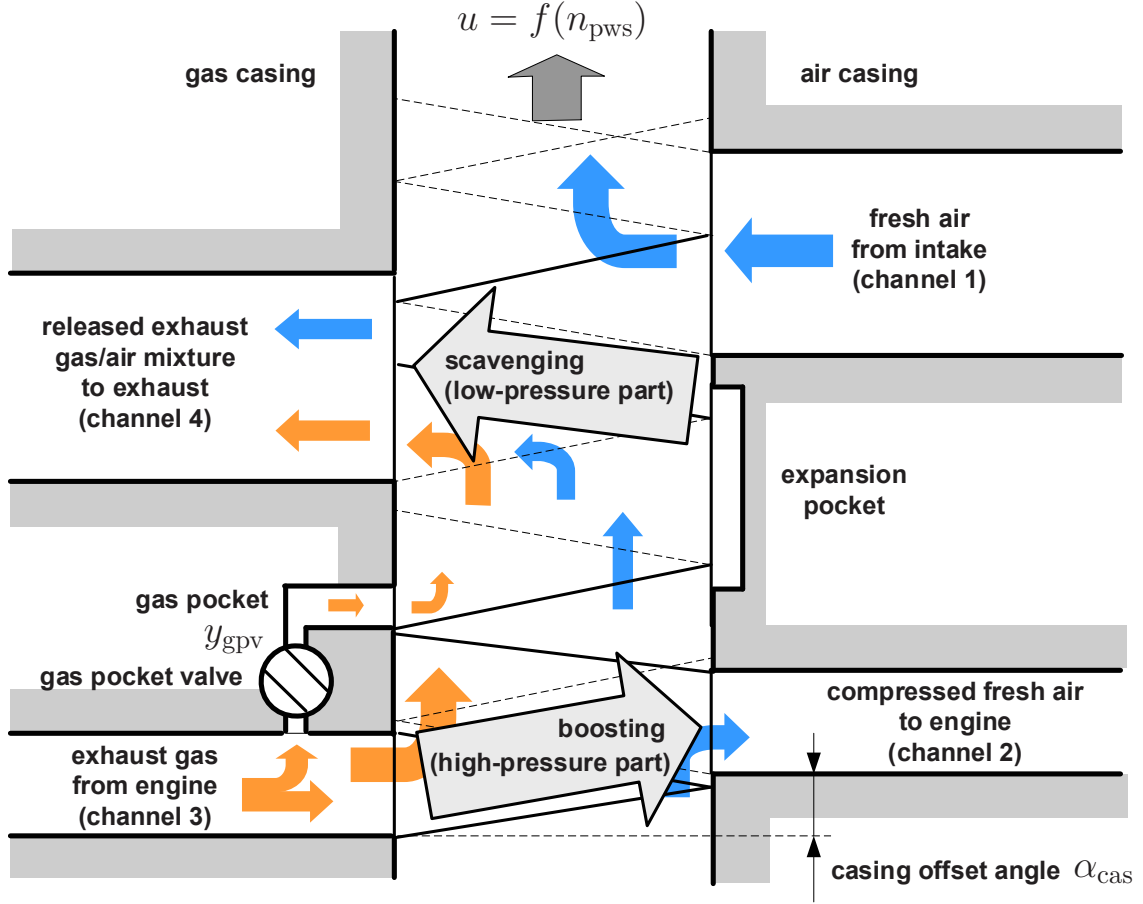


**Figure 1.2:** Schematic overview of the PWS: four channels (Channel 1, ..., Channel 4) and two pockets (gas pocket, expansion pocket) are linked to the rotating cell-wheel. Three actuators affect the pressure-wave processes: The gas pocket valve ( $y_{gpv}$ ) controls the amount of energy required for boosting to that necessary for scavenging. The cell-wheel speed ( $n_{pws}$ ) and the offset angle of the casing ( $\alpha_{cas}$ ) guarantee the best charging efficiency. This optimum is reached for well-tuned operating conditions, i.e., when the opening and closing events of the channels correspond to the running times of the pressure waves.

portion of the exhaust gases through the gas pocket valve on the one hand reduces the exhaust gas pressure in Channel 3 and therefore lowers the compression of the fresh air in Channel 2. On the other hand, the exhaust gas enthalpy flowing through the gas pocket valve increases the pressure in the cell just before the low-pressure part starts, which improves scavenging (Croes, 1979; Mayer et al., 1990; Weber, 2001). The target of the low-pressure part is to scavenge the cell towards Channel 4 and to fill it up again with fresh air from Channel 1. Under normal operating conditions, Channel 4 is not only

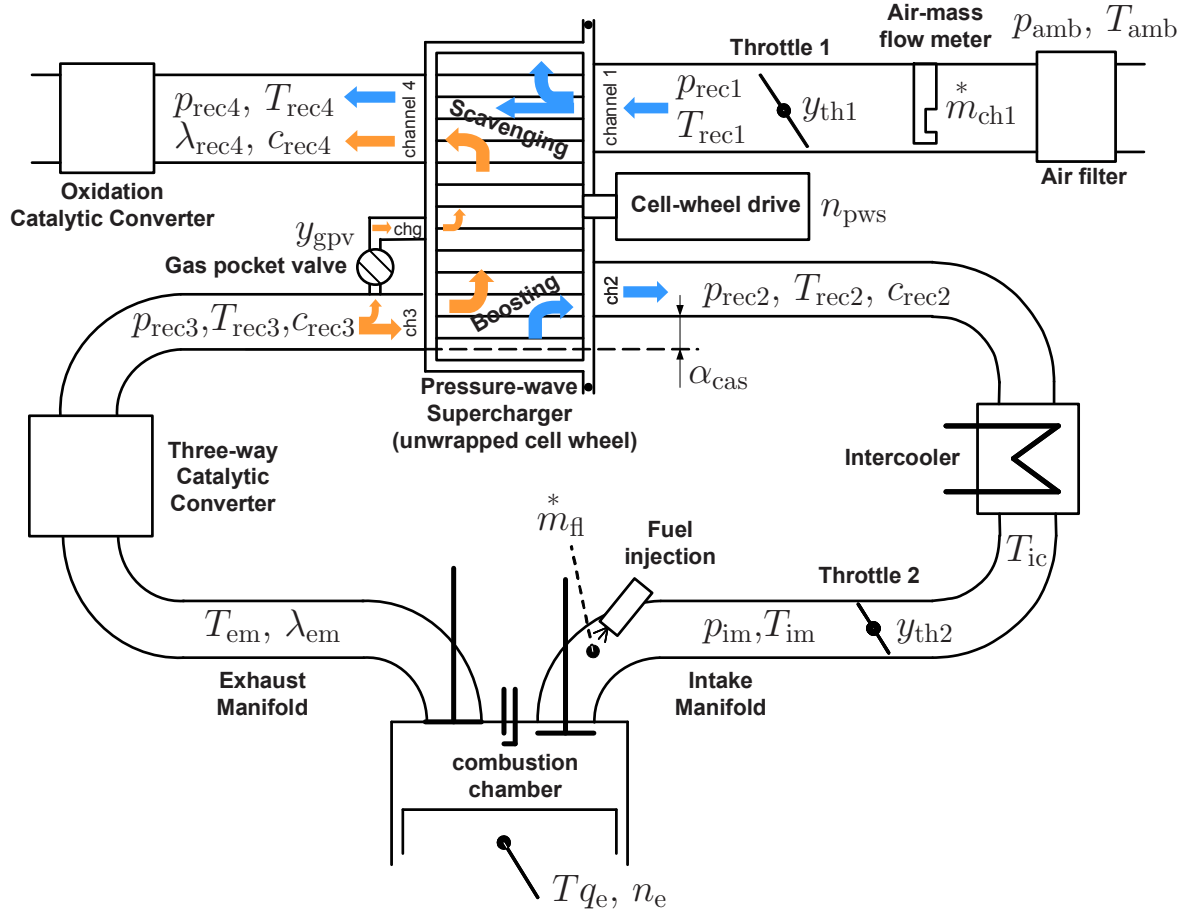


**Figure 1.3:** Pressure-wave supercharged engine system structure

filled with exhaust gases, but also with fresh air that was compressed in the high-pressure part, but did not flow into Channel 2. The part of fresh air in Channel 4 is called *scavenging air*. It can be reduced by lowering the pressure in Channel 1. The less scavenging air is present, the higher the temperature is in Channel 4. This improves oxidation conditions in the catalytic converter.

The large number of actuators, which constitute system inputs, can cause a multitude of cross couplings towards the mass flows (system outputs), particularly in the mass flow through Channel 2, which directly affects the engine torque.

Therefore, it is important to understand the main effects and phenomena that take place in PWS. Moreover, a model-based control strategy may guarantee a high performance and a robust system behavior.



## 1.3 Model-based Control

Modern combustion engine systems can be understood as multiple-input multiple-output (MIMO) systems. Throttle positions, injected fuel mass, and brake torque are regarded as system inputs. The output contains the absolute values and time derivatives of the engine output torque and items such as emissions, noise, vibrations, etc. During the development and calibration of an engine, the overall engine system behavior has to be optimized in terms of performance, robustness, and physical or legal constraints. An experimental search for these optima is very time-consuming and expensive since many parameters need to be varied and the search has to be repeated for numerous operating conditions in the engine map (engine load over engine speed).

Nowadays, sufficiently accurate models are available based on both basic physical principles and on measurement data obtained from existing systems.

There are many different ways of modeling a PWS considering accuracy, computational burden, and the possibility of extrapolation to operation modes that cannot be measured.

In this work, two approaches are followed, trading off accuracy versus computational burden. In Section 3.1, a first-principle, finite-difference model (FDMdl) is derived that furnishes detailed insights into the processes and phenomena of PWSs and that allows the analysis of the sensitivity of model parameters and system inputs. This model is compared with measurement data from a real engine system. Since the FD model is far from being usable in real-time applications, a simplified model is derived in Sect. 3.2 (MVMdl).

The engine and its auxiliary components except for the supercharger are modeled in Chapter 2.

## 1.4 The Engine System

As depicted in Fig. 1.3, the following inputs of the PWS engine system are to be considered as main influences on the output torque:

- Throttle 2 represents the main actuator to control the engine load in the naturally aspirated mode. The variable  $y_{th2}$  indicates how much the throttle is *opened*. The throttle is closed for  $y_{th2} = 0$

and wide open for  $y_{th2} = 1$ . An increased engine torque goes with increasing  $y_{th2}$ .

- The gas pocket valve adjusts the ratio of exhaust gas enthalpy that is bypassed by the charging process. It therefore controls the degree of supercharging. The variable  $y_{gpv}$  indicates how much the throttle is *closed*. The valve is closed for  $y_{gpv} = 1$  and wide open for  $y_{gpv} = 0$ . Again, an increased engine torque goes with increasing  $y_{gpv}$ .
- The adjustments of the cell-wheel speed ( $n_{pws}$ ) and the offset angle of the casing ( $\alpha_{cas}$ ) can guarantee a well-tuned pressure-wave process. This directly affects the charging efficiency.
- The position of Throttle 1 ( $y_{th1}$ ) is a means to control the scavenging air mass flow and therefore the temperature in Channel 4.

The output of interest in this work is the temporal behavior of the engine torque. As described in Guzzella and Onder (2004), the torque of a stoichiometric spark-ignition engine is controlled by the quantity of air/fuel mixture in the cylinder during each stroke, assuming a constant air/fuel ratio. Typically, this mass flow is varied by changing the intake manifold pressure. Hence, the main focus in this text is on the dynamics of the pressures and temperatures in the system.

As depicted in Fig. 1.4, the system is split into a number of mass and energy reservoirs, the so-called *receivers*. The receivers are subject to a filling-and-emptying process caused by flows through throttle-similar connectors such as flow restrictions and compressors. The relevant dynamics are described by ordinary differential equations (ODEs) in the lumped pressures and temperatures in Receiver 1 to Receiver 4, intake, and exhaust manifolds. The computations of the mass and energy flows through the connectors between the receivers are simplified as static functions. The connectors are Throttle 2, intercooler, three-way catalytic converter (TWC), engine, and supercharger. In a mean-value approach, the reciprocating behavior of the cylinders of an engine is replaced by a continuously working volumetric “pump” that produces hot exhaust gases and torque. As the Sankey diagram (Fig. 1.5) clearly shows, a PWS



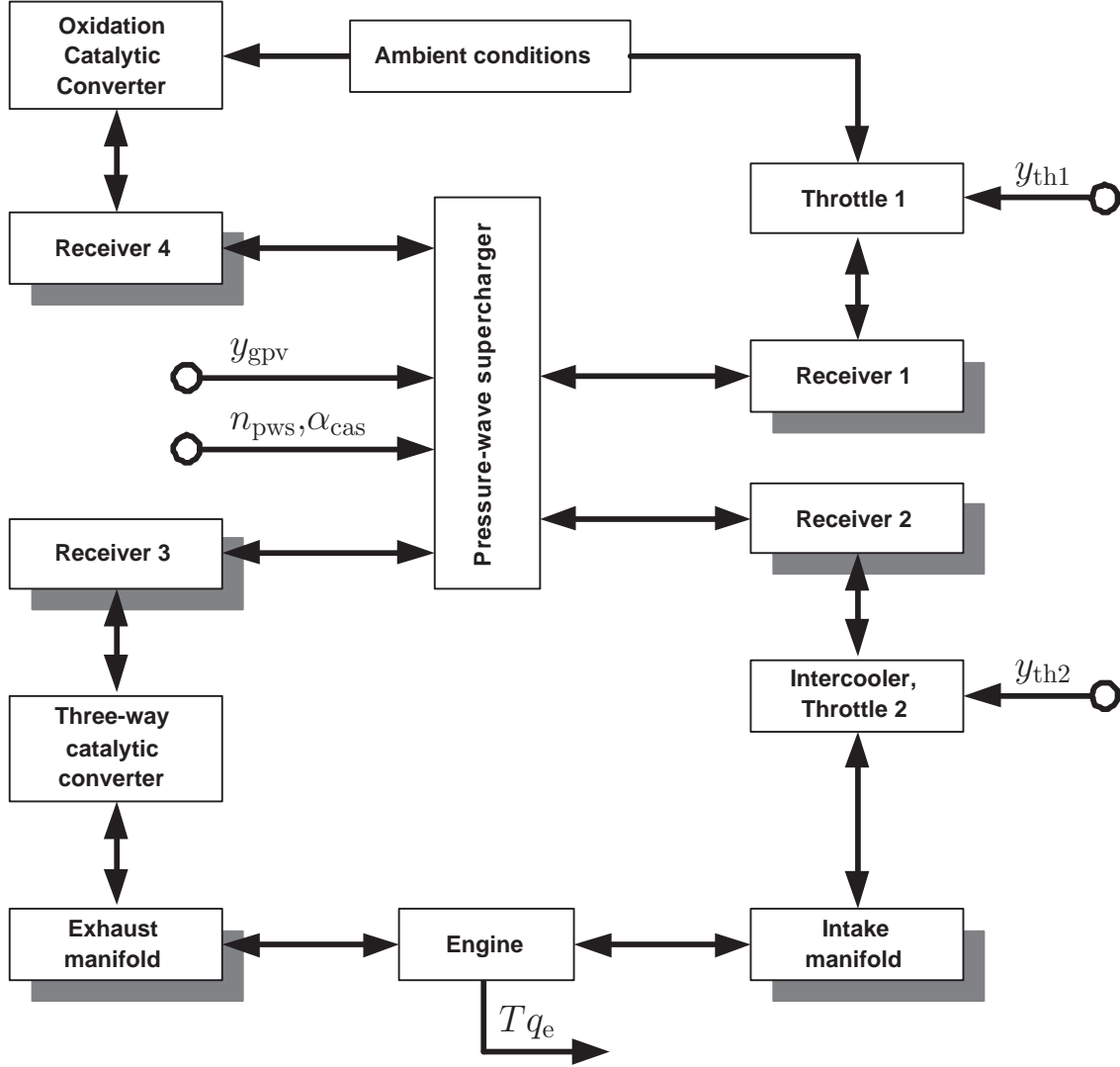


**Figure 1.4:** A simplified control-oriented system structure. The shadowed blocks cause the system dynamics. The detailed cause and effect diagrams will follow in Figs. 1.6 and 2.1.

functions similarly to a “generalized throttle”. The device basically includes four channels which are connected to four receivers. The pressures  $p_{\text{rec}1}$  to  $p_{\text{rec}4}$ , the temperatures  $T_{\text{rec}1}$  and  $T_{\text{rec}3}$ , and the actuator input signals  $y_{\text{gpv}}$  (gas pocket valve),  $n_{\text{pws}}$  (cell-wheel speed), and  $\alpha_{\text{cas}}$  (casing offset) thus define the mass flows as follows:

- $\dot{m}_{\text{ch}1}^*$ : fresh air mass flow entering the PWS through Channel 1
- $\dot{m}_{12}^*$ : compressed air mass flow exiting through Channel 2

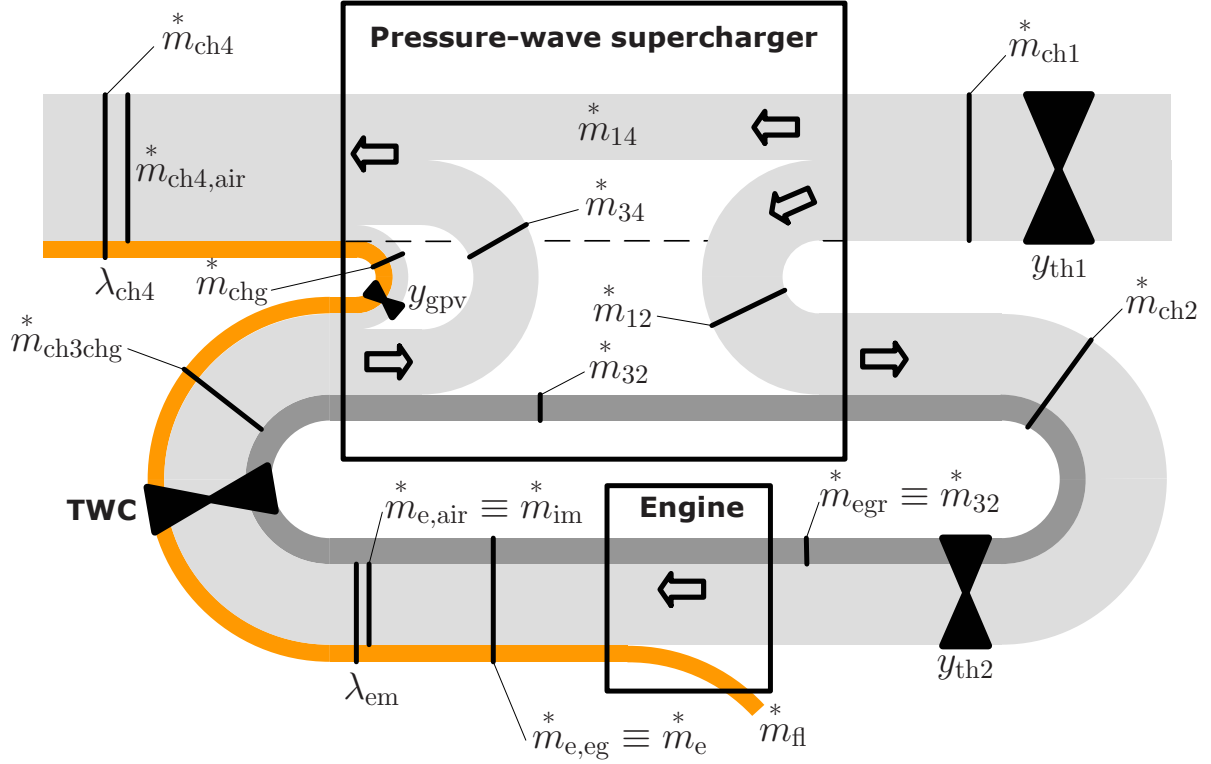


Figure 1.5: The PWS as a generalized throttle

- $\dot{m}_{14}^*$ : scavenging air mass flow exiting through Channel 4 instead of Channel 2
- $\dot{m}_{34}^*$ : exhaust gas mass flow exiting through Channel 4; part of its energy is transmitted to  $\dot{m}_{12}^*$
- $\dot{m}_{32}^*$ : recirculated exhaust gas mass flow exiting through Channel 2 instead of Channel 4
- $\dot{m}_{chg}^*$ : exhaust gas mass flow that is bypassed by the boosting process
- $\dot{m}_{ch3chg}^*$ : hot exhaust gas mass flow from three-way catalytic converter through Channel 3 and gas pocket
- $\dot{m}_{ch2}^*$ : mixture of compressed air and recirculated exhaust gas exiting through Channel 2

- $\dot{m}_{\text{ch4}}^*$ : mixture of released exhaust gas and fresh air exiting through Channel 4

In an abstract way, the Sankey diagram conveniently serves to summarize all the mass flow *quantities* through the channels, the PWS device, and the engine. However, the *directions* of those mass flows are more exactly represented by Fig. 1.3.

Figure 1.4 can be redrawn as the cause-and-effect diagram shown in Fig. 1.6, denoting the signal flow paths. It shows the driving and the driven variables. For throttles, typically pressures are driving variables and mass flows are driven variables, while for receivers the reverse is true.

One goal of this text is to derive a controller that can handle the described engine system in the following way:

- maximum efficiency
- optimal driveability: fast torque response to driver request, particularly a fast, steady, and smooth rise after a “tip-in” command by the driver (curve (b) in Fig. 1.7)
- optimal exhaust gas aftertreatment conditions ( $T_{\text{rec4}}$ )

For the second point, the EGR problem in particular needs to be taken into account. Since in PWSs fresh air and exhaust gas are in direct contact in the cell wheel, unwanted and excessive EGR over the PWS has to be limited by appropriate control actions. The most critical situation arises whenever large amounts of exhaust gas are recirculated from the exhaust to the intake manifolds of the engine during a rapid transient. This causes the engine torque to drop sharply and thus to severely affect driveability (curve (c) in Fig. 1.7).

Whereas curve (c) in Fig. 1.7 schematically shows such a load step, in Fig. 1.8 the actuator positions Throttle 2 ( $y_{\text{th2}}$ ) and gas pocket valve position ( $y_{\text{gpv}}$ ) as well as the engine torque formation are plotted over time for two typical load steps. A minor change in the gas pocket valve closing trajectory causes the engine torque to drop due to a temporary peak in the EGR rate  $x_{\text{egr}}$ .

In Fig. 1.9 the influence of the cell-wheel speed  $n_{\text{pws}}$  and the casing offset  $\alpha_{\text{cas}}$  on the engine torque is displayed for one engine operating

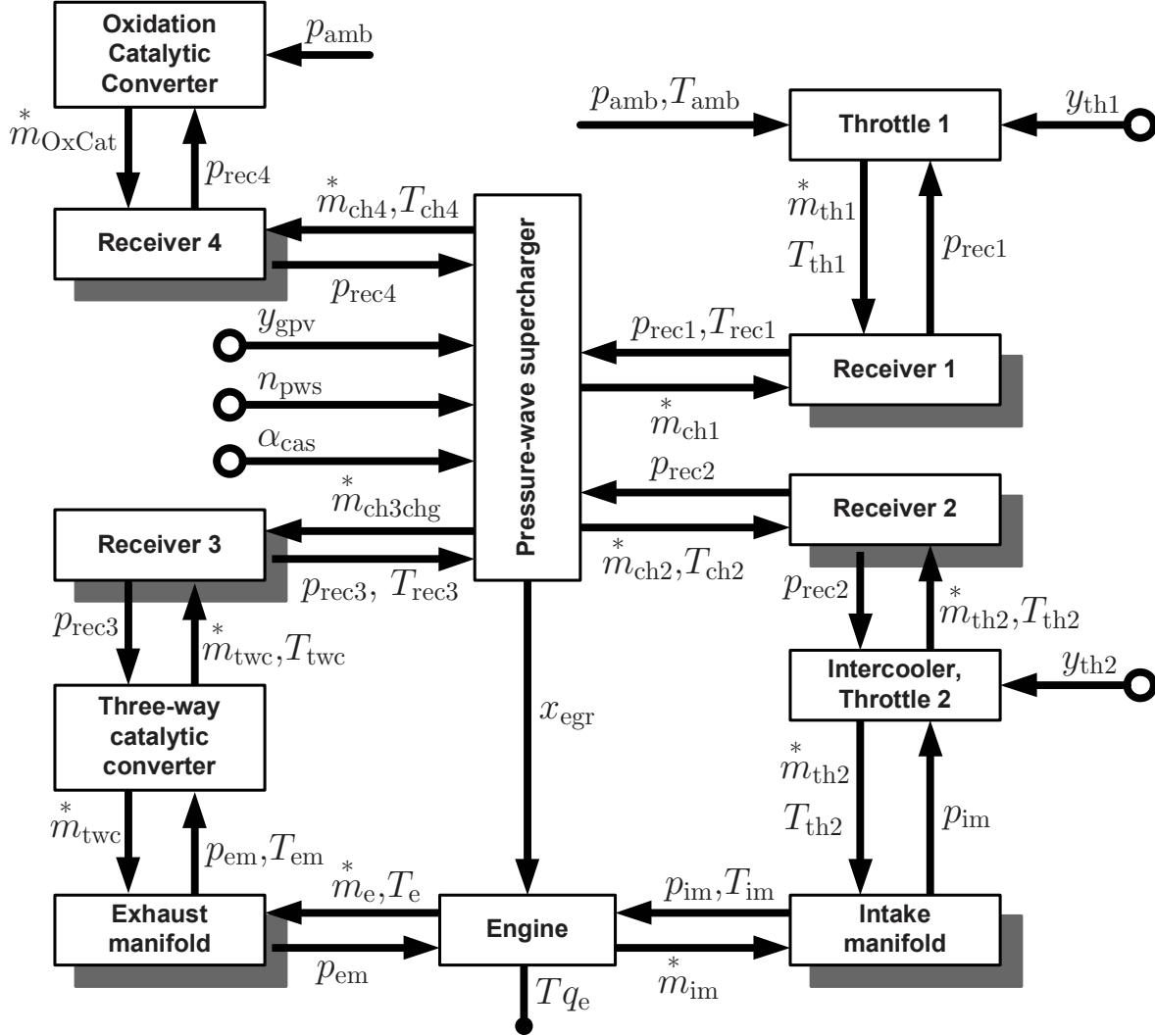


**Figure 1.6:** Cause-and-effect diagram of the engine system. Inputs into blocks constitute the causes and outputs the effects. Whereas for “receiver blocks” (shaded) inputs may be mass and energy flows and outputs are pressure and temperature, for static blocks usually the reverse is true.

point. All actuator inputs are kept constant, except for  $\alpha_{cas}$  and  $n_{pws}$ . Evidently, there exists one maximum only. Any speed variation of 1,000 rpm or an angle variation of  $3^\circ$  reduces the torque value by at least 5% for this specific operating point.

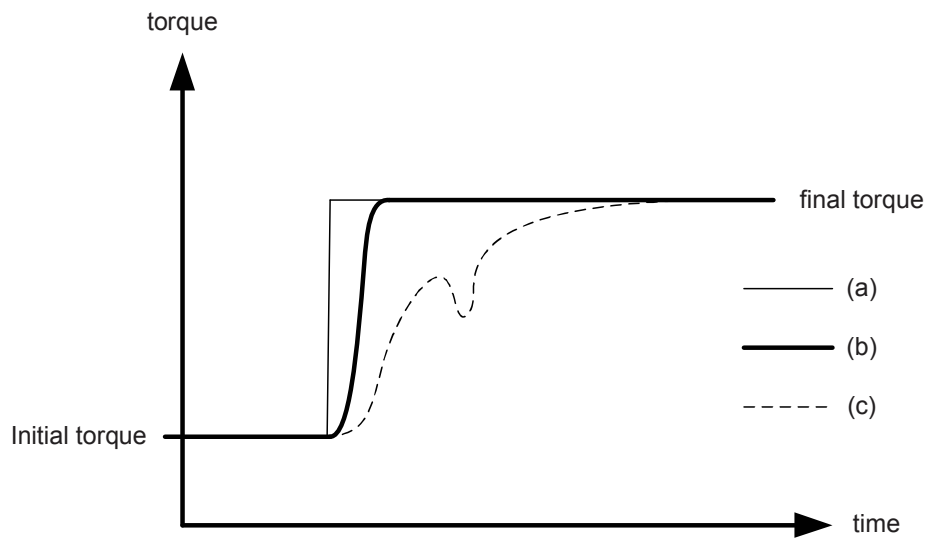


**Figure 1.7:** Desired input/output behavior: (a) Driver's requested torque (tip-in), (b) driveability-optimal torque build-up, (c) torque build-up when transient EGR occurs (torque drop)

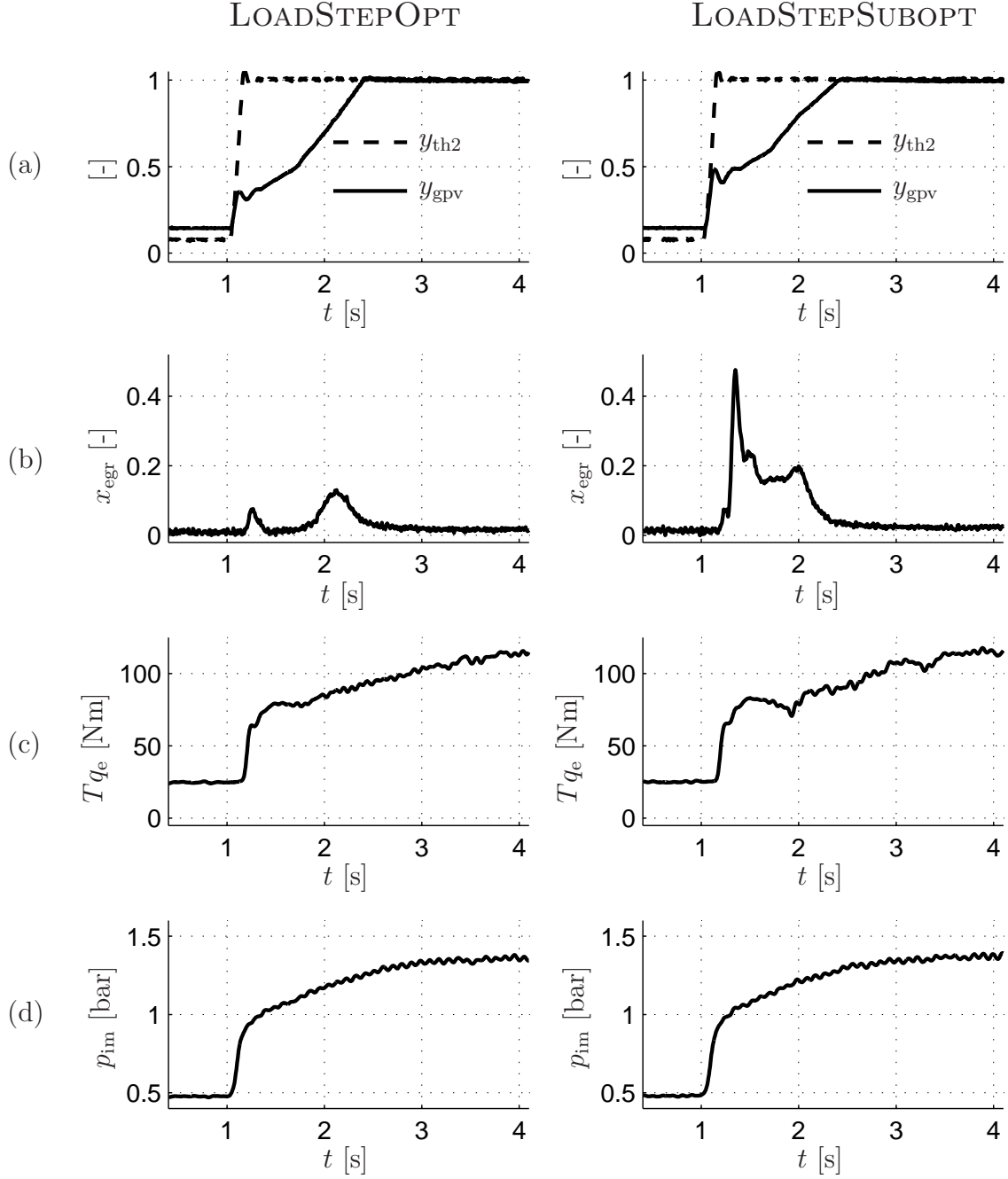


**Figure 1.8:** Optimal and sub-optimal load steps at 1500 rpm on the EA111/HX95 engine (see Appendix A): (a) Actuator positions (Throttle 2, gas pocket valve), (b) EGR rates  $x_{egr} := \dot{m}_{egr}^*/\dot{m}_{ch2}^*$ , and (c) torque formations without (left) and with (right) transient EGR occurring. (d) No difference visible in the intake manifold pressure build-up.

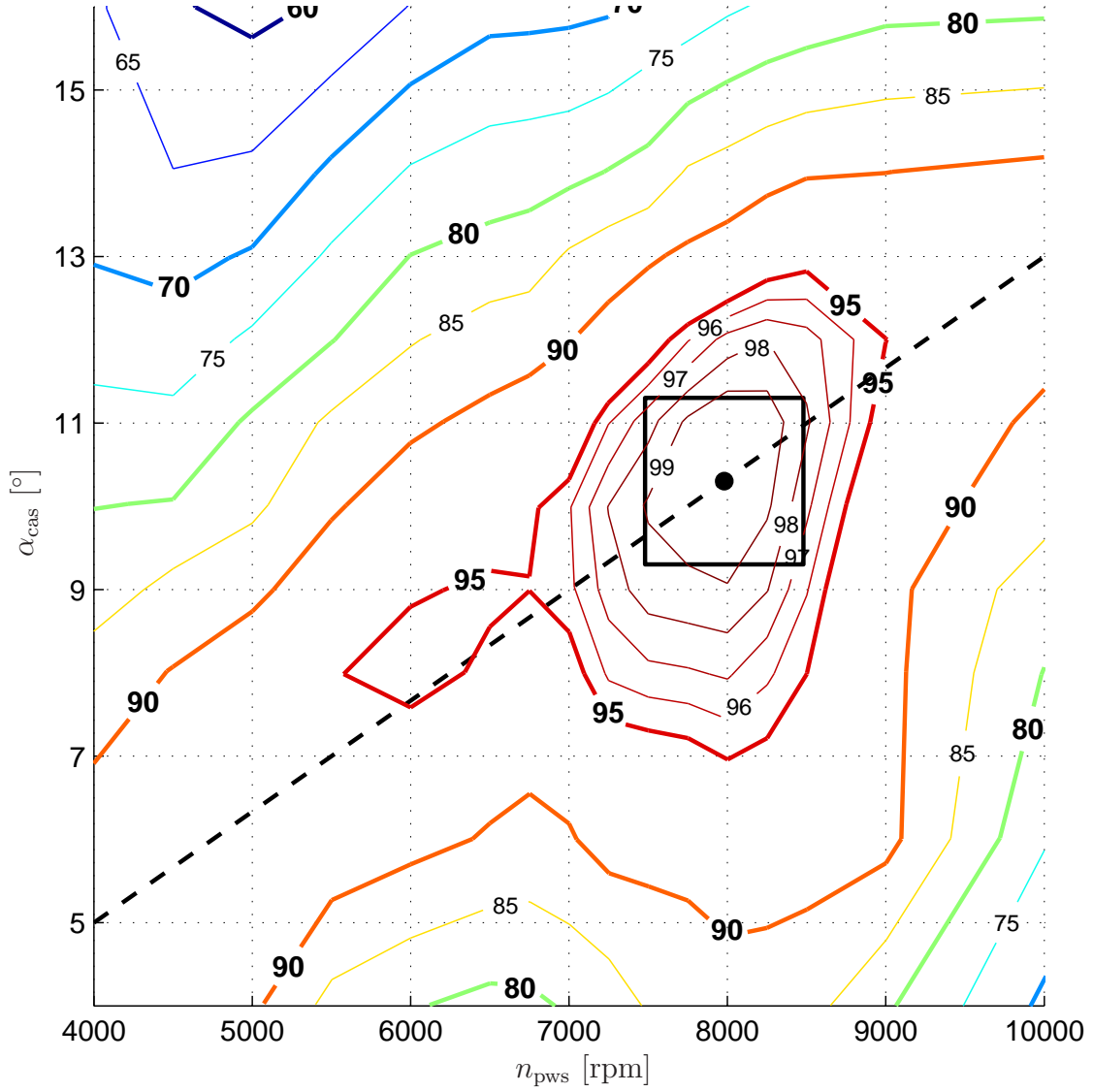


**Figure 1.9:** Engine torque (in unit Nm) over cell-wheel speed and casing offset angle variation on the EA111/HX95: The engine torque drops from the nominal (best) value (100 Nm) indicated by the dot for any “out-of-tune” condition. However, within the boundary  $\pm 500$  rpm and  $1^\circ$  (indicated by solid box) the torque drop is less than 4%. (Operating point:  $y_{th1} = 1$ ,  $y_{th2} = 0.3$ ,  $y_{gpv} = 1$ ,  $n_e = 1500$  rpm)

## 1.5 Motivation

The concept of pressure-wave supercharged engines is being considered as an alternative to turbo concepts by several car manufacturers. Modern turbocharged engines have become complex and costly structures such that a general tendency towards simpler systems has become noticeable mainly in the low-price passenger car market. However, the acceptance of PWSs is still low in the automotive industry. This may be due to earlier unfortunate experiences with Comprex-diesel passenger cars or from the unfamiliar physical principles on which this device is based. These doubts may be allayed if it is possible to explain and control the processes and phenomena of PWSs.

## 1.6 Contributions

A universally valid PWS-model is developed with respect to geometry, leakage, heat transfer, friction, and varying actuator inputs.

Based on this first-principle finite difference model (FDMdl) and assuming that the PWS is operated under efficiency-optimal conditions, a simplified, control-oriented mean-value model (MVMdl) is derived and validated with experiments.

In order to guarantee the proper operation of the engine system, a control concept is proposed which takes into account efficiency, driveability, and emissions.

- I. Cell-wheel speed and casing offset are set using a model for the running times of the first two essential shock waves. This results in a model-based open-loop controller.
- II. Concerning driveability, the control concept is based on the fact that the EGR rate  $x_{\text{egr}} = \dot{m}_{\text{egr}}^* / \dot{m}_{\text{ch2}}^*$  is linked to the scavenging rate  $x_{\text{sc}} = \dot{m}_{14}^* / \dot{m}_{\text{ch2}}^*$ , an indicator for the amount of compressed air leaving through Channel 4 instead of Channel 2. Thus, it is possible to substitute the scavenging rate  $x_{\text{sc}}$  for the EGR rate  $x_{\text{egr}}$  as a control variable. A fast, steady, and smooth torque formation, achieved by avoiding EGR therefore can be guaranteed by maintaining the scavenging rate  $x_{\text{sc}}$  above a certain level  $x_{\text{sc,min}}$ . The scavenging rate  $x_{\text{sc}}$  is estimated using



$y_{th2}$  and  $y_{gpv}$  as the main inputs. During fast acceleration maneuvers a precise prediction of  $x_{sc}$  is necessary since the feedback signals for estimating  $x_{sc}$  (i.e.  $\dot{m}_{ch1}^*$  and  $\dot{m}_{ch2}^*$ , or  $\lambda_{em}$  and  $\lambda_{rec4}$ ) are subject to time delays. The required predictor is realized using a linear first-order derivative lag element, also known as a  $DT_1$  element, in combination with a non-linear static function.

- III. With respect to emissions, it is proposed that  $T_{rec4}$  be kept as high as possible, i.e. to hold  $x_{sc}$  as low as possible, a goal contrary to the driveability postulation. The trade-off is solved by maintaining – in the normal case –  $x_{sc}$  below a certain limit  $x_{sc,max}$  using Throttle 1, but to open the throttle completely during fast acceleration maneuvers.

The three parts that constitute the control concept are implemented and verified on the EA111/HX95 engine test rig (see Appendix A). The design and realization of that test bench was another important part of the preparations for this work. Particularly the realization of a fast and fully flexible control system presented quite a challenge.

## 1.7 Structure of the thesis

The model of the engine and its auxiliary components except for the supercharger are described in Chapter 2.

Two approaches for modeling the PWS are at the core of this work. They are detailed in Chapter 3, Section 3.1 treating a finite-difference model (FDMdl), which then forms the basis for the development of a simplified, control-oriented mean-value model (MVMdl) described in Section 3.2. The FDMdl presented is subject to a minimum of assumptions and requires only a few parameters to be identified. It is computationally very demanding, but it is a versatile tool for visualizing and investigating the pressure-wave processes for very different types of PWSs and for very different operating conditions.

Chapter 4 covers the closed-loop simulation and validation of the entire engine system model, i.e., the simulation of the blocks introduced in Chapter 2 together with the MVMdl.

Chapter 5 deals with the control system design and verification. Starting from basic requirements, a control strategy is derived. Using the engine system model, the controllers were initially tested off-line. The approaches are then implemented and verified on the engine test rig.

Chapter 6 draws the conclusions of this work. The limits of the presented concepts are discussed and future research directions are proposed.

All models are validated by measurements and by reference data that is derived in Appendix A. The Appendices B, C, and D contain the derivations of the governing equations for the two PWS models.

## Chapter 2

# Modeling and Validation of the Engine System

Whereas the idea of pressure-wave machines is a very interesting one, its potential simplicity is misleading since the mechanisms and behavior of this device are not that easy to understand.

Experiments demonstrated that both the casing offset angle  $\alpha_{\text{cas}}$  and the cell-wheel speed  $n_{\text{pws}}$  affect the behavior of the *steady-state* PWS and thus of the engine (Fig. 1.9). As shown in Fig. 1.8, the *transient* influence of the gas pocket valve is critical.

The challenge of this work is to understand, visualize, explain, and finally control the processes of a pressure-wave supercharged engine. Therefore, a model is needed that is able to reproduce data such as pressures, temperatures, mass flows that are measured at the real engine system. But additionally, it has to deliver information about quantities that require extensive effort to be measured or that are virtually non-measurable in series production engines.

### Overview

The aspects of special interest modeled here are those that directly affect the engine torque. Therefore, Fig. 2.1 reduces Fig. 1.6 to the following points:

- Apart from engine speed, the engine mass flow and the engine torque mainly depend on the pressure and temperature of the intake manifold ( $p_{\text{im}}$ ,  $T_{\text{im}}$ ) and on the EGR rate  $x_{\text{egr}}$ . Thus the high-pressure loop is modeled, going from PWS to Receiver 2 to intercooler/Throttle 2 to intake manifold to engine to exhaust

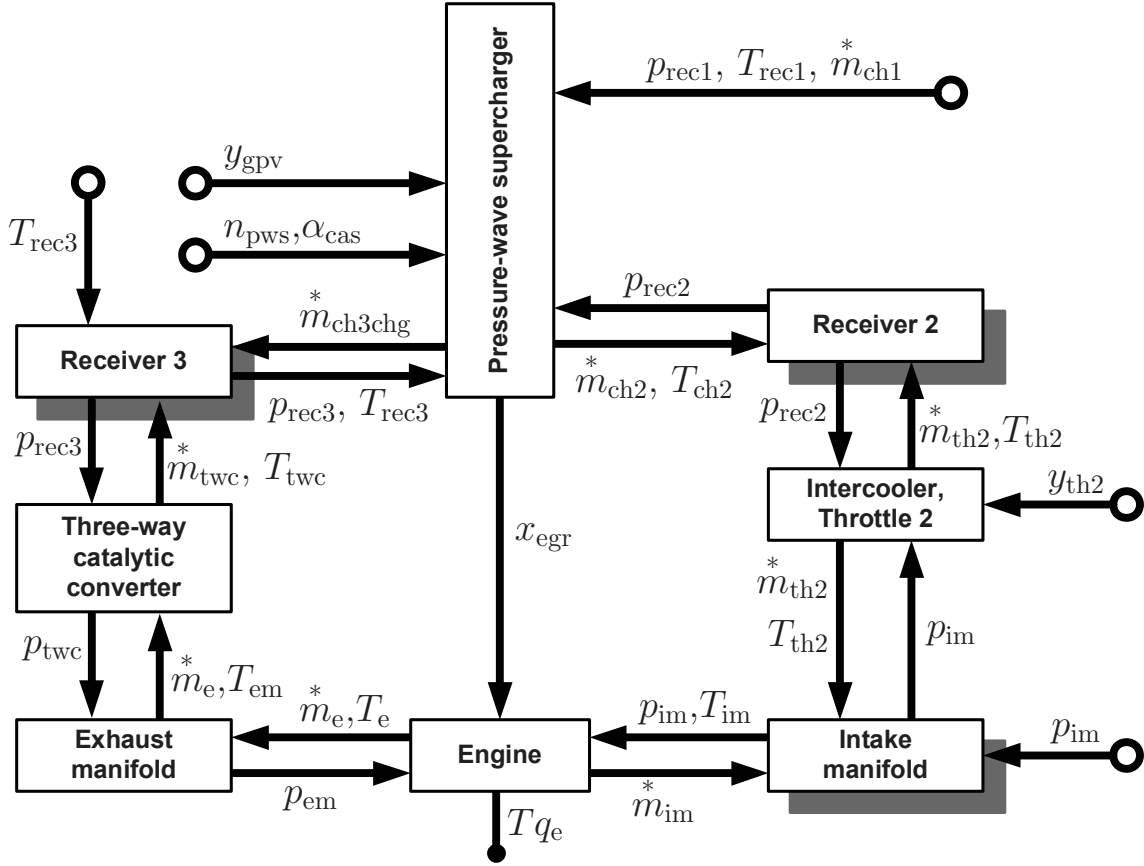


**Figure 2.1:** Cause-and-effect diagram of the engine system (with simplifications). For instance, for the block *Receiver 2* the signals  $\dot{m}_{\text{ch2}}^*, T_{\text{ch2}}, \dot{m}_{\text{th2}}^*$ , and  $T_{\text{th2}}$  are the causes from the blocks *Pressure-wave Supercharger* and *Intercooler, Throttle 2*, whereas  $p_{\text{rec2}}$  is the effect.

manifold to TWC to Receiver 3 and back to the PWS. In contrast, the EGR rate ( $x_{\text{egr}}$ ) is derived from both the high-pressure and the low-pressure part. A simple EGR model may be derived if the inputs  $p_{\text{rec1}}$  to  $p_{\text{rec4}}, T_{\text{rec1}}$ , and  $T_{\text{rec3}}$  are replaced by  $\dot{m}_{\text{ch1}}^*$  as input signals.

- Modern engine control systems feature sensors in the engine outlet to feed back pressure and temperature values. The temperature  $T_{\text{rec3}}$  is therefore not predicted in the model.
- Another problem may arise with instabilities due to modeling errors. On the one hand, the errors of the submodels in the high-pressure loop are cumulative. On the other hand, the PWS is modeled as a static function and therefore immediately transmits

the errors without time lag or damping effect. The simulation of the closed (high-pressure) loop can become unstable when the cumulative errors of each submodel become too high. The problem is solved by taking the measured signal  $p_{\text{im}}$  as another system input to control the simulated  $p_{\text{im}}$  value. Both increasing precision and guaranteed stabilization of the simulation is achieved this way.

- The dynamics of the low-pressure Receivers 1 and 4 may be neglected since they are much faster than those of Receivers 2 and 3. The in- and outgoing mass flows for Receivers 1 and 4 are high compared to the receiver volumes. As will be shown in Sect. 3.1, the sensitivity of  $\dot{m}_{\text{ch1}}^*$  and  $\dot{m}_{\text{ch4}}^*$  towards pressures  $p_{\text{rec1}}$  and  $p_{\text{rec4}}$  is very high.

The receivers are modeled with lumped parameters for temperature and pressure (0-dimensional approach). Flow restrictions are modeled as static functions. Sections 2.1 and 2.2 contain the descriptions of receiver and flow restriction models. An approach for modeling the mass flow through the engine is presented in Sect. 2.4. The engine is considered to be basically a “generalized pump”. The PWS is described in greater detail in Chapter 3, with Sect. 3.1 containing a model where the governing equations are partial differential equations which are numerically solved using a finite-difference method and Sect. 3.2 containing a model where the linearized governing equations yield explicit solutions.

Finally, in Chapter 4, simulation results of the closed high-pressure loop are presented and validated with measurement data.

## 2.1 Receiver Model

The relevant *dynamic parts* in the engine system are represented by the mass and energy storage in the receivers. With the assumptions of perfect gas behavior and perfect mixing temperature and pressure are constant over the receiver. As depicted in Fig. 2.1, the engine system generally consists of three receivers who may be modeled the same way:

- Receiver 2 containing compressed fresh air and exhaust gas from the PWS
- The intake manifold between intercooler/Throttle 2 and the engine
- Receiver 3 leading the hot exhaust gas from the TWC to the PWS

The model for the receiver is based on mass and energy conservation laws. Two lumped parameters,  $p$  and  $T$ , represent the states. The mass balance yields the following time derivative for the mass in the receiver:

$$\frac{dm_{\text{rec}}}{dt} = \dot{m}_{\text{in}}^* - \dot{m}_{\text{out}}^* \quad (2.1)$$

The receiver temperature is derived from the energy balance. The internal energy in the receiver is:

$$U_{\text{rec}} = m_{\text{rec}} c_v T_{\text{rec}} \quad (2.2)$$

The complete time derivative of the inner energy must be equal to the sum of the energy flows crossing the system border

$$\begin{aligned} \frac{dU_{\text{rec}}}{dt} &= \frac{dm_{\text{rec}}}{dt} c_v T_{\text{rec}} + \frac{dT_{\text{rec}}}{dt} c_v m_{\text{rec}} \\ &\stackrel{!}{=} \dot{H}_{\text{in}}^* - \dot{H}_{\text{out}}^* + \dot{Q}_{\text{in}}^* \end{aligned} \quad (2.3)$$

and the enthalpy flow is

$$\dot{H} = \dot{m}^* c_p T \quad (2.4)$$

This yields the following expression for the time derivative of the temperature:

$$\frac{dT_{\text{rec}}}{dt} = \frac{1}{m_{\text{rec}} c_v} \left( \dot{m}_{\text{in}}^* c_p T_{\text{upstr}} - \dot{m}_{\text{out}}^* c_p T_{\text{rec}} - \frac{dm_{\text{rec}}}{dt} c_v T_{\text{rec}} + \dot{Q}_{\text{in}}^* \right) \quad (2.5)$$

Finally, based on the ideal gas law, the pressure is determined from mass and temperature:

$$p_{\text{rec}} = \frac{m_{\text{rec}} R T_{\text{rec}}}{V_{\text{rec}}} \quad (2.6)$$

## 2.2 Flow Restriction Model

Flow restrictions between the receivers are described by *static* algebraic relations and are found in several places along the air flow path of the engine. The TWC and the exhaust system (wall friction) is modeled as a pressure drop for an *incompressible* fluid (Eriksson et al., 2001) (no backflow expected).

$$\Delta p = p_{\text{em}} - p_{\text{rec3}} = K_{\text{fr}} \frac{T_{\text{em}}^* m_e^2}{p_{\text{em}}} \quad (2.7)$$

The *compressible* fluid model is used when high velocities occur in the flow through the restriction. This is the case for Throttle 2 and the gas pocket valve. The acceleration of the flow is then modeled as being isentropic and the energy dissipation as being isobaric such that the complete state change over the restriction shows approximately an *isenthalpic* behavior (Heywood, 1988; Baehr, 1992). The mass flow through the restriction is computed as a function of its geometric opening area  $A_{\text{geo}}$ , the discharge coefficient  $c_d$ , and of the states of the surrounding receivers. If the upstream pressure is defined as  $p_1$ , the downstream pressure as  $p_2$ , and the pressure ratio over the restriction as  $\Pi = p_2/p_1 \leq 1$ , the mass flow through the throttle in the subsonic case

$$1 \geq \Pi \geq \left( \frac{2}{\kappa + 1} \right)^{\frac{\kappa}{\kappa - 1}} \quad (2.8)$$

can be estimated according to

$$m_{\text{restr}}^* = A_{\text{geo}} c_d \frac{p_1}{\sqrt{RT_1}} \sqrt{\frac{2\kappa}{\kappa - 1} \left[ (\Pi)^{\frac{2}{\kappa}} - (\Pi)^{\frac{\kappa+1}{\kappa}} \right]} \quad (2.9)$$

In the sonic case

$$\Pi < \left( \frac{2}{\kappa + 1} \right)^{\frac{\kappa}{\kappa - 1}} \quad (2.10)$$

the flow is choked and the mass flow yields

$$m_{\text{restr}}^* = A_{\text{geo}} c_d \frac{p_1}{\sqrt{RT_1}} \sqrt{\kappa} \left( \frac{2}{\kappa + 1} \right)^{\frac{\kappa+1}{2(\kappa-1)}} \quad (2.11)$$

As proposed in Guzzella and Onder (2004), for many working fluids such as intake air and exhaust gas at lower temperature ( $\kappa \approx 1.4$ ), Eq. (2.11) can be approximated by

$$\dot{m}_{\text{restr}}^* = A_{\text{geo}} c_d \frac{p_1}{\sqrt{RT_1}} \frac{1}{\sqrt{2}} \quad (2.12)$$

for sonic conditions ( $\Pi < 0.5$ ), and Eq. (2.9) by

$$\dot{m}_{\text{restr}}^* = A_{\text{geo}} c_d \frac{p_1}{\sqrt{RT_1}} \sqrt{2 \Pi (1 - \Pi)} \quad (2.13)$$

for subsonic conditions ( $0.5 \leq \Pi < 0.95$ ). In order to avoid any problems solving the resulting ordinary differential equations due to the infinite gradient at  $p_1 = p_2$ , for  $\Pi > \Pi_{\text{crit}} = 0.95$ , Eq. (2.13) is replaced by the linear approach

$$\dot{m}_{\text{restr}}^* = A_{\text{geo}} c_d \frac{p_1}{\sqrt{RT_1}} \left( 1 - \frac{\Pi - \Pi_{\text{crit}}}{1 - \Pi_{\text{crit}}} \right) \sqrt{2 \Pi_{\text{crit}} (1 - \Pi_{\text{crit}})} \quad (2.14)$$

The geometric restriction area  $A_{\text{geo}}$  is a function of the restriction control input  $y_{\text{th2}}$  and  $y_{\text{gpv}}$ , respectively, both ranging within  $[0, 1]$ . For Throttle 2, the area is calculated from the geometric opening angle  $\alpha$ .

$$A_{\text{geo,th2}} = \frac{\pi d_{\text{th2}}^2}{4} \left( 1 - \frac{\cos(\alpha)}{\cos(\alpha_0)} \right) \quad (2.15)$$

The signal  $y_{\text{th2}}$  is arranged by a linear function between the minimum and maximum angle  $[\alpha_0, \alpha_1]$ .

$$\begin{aligned} \text{fully closed:} & \quad y_{\text{th2}} = 0 \quad \Leftrightarrow \quad \alpha = \alpha_0 \approx 15^\circ \\ \text{linear function:} & \quad 0 < y_{\text{th2}} < 1 \quad \Leftrightarrow \quad \alpha = \alpha_0 + y_{\text{th2}} (\alpha_1 - \alpha_0) \\ \text{fully open:} & \quad y_{\text{th2}} = 1 \quad \Leftrightarrow \quad \alpha = \alpha_1 \approx 85^\circ \end{aligned}$$

The gas pocket valve is designed as a cylinder featuring a rectangular millcut at right angle to the center line. The restriction area  $A_{\text{geo}}$  therefore can be assumed to be linearly related to  $y_{\text{gpv}}$  as well. Since for both  $y_{\text{th2}}$  and  $y_{\text{gpv}}$ , increasing values should result in increasing engine torque,  $y_{\text{gpv}}$  is defined to be zero for the fully open gas pocket valve restriction area.



$$\begin{aligned}
\text{fully closed:} & \quad y_{\text{gpv}} = 1 \quad \Leftrightarrow \quad A_{\text{geo,gpv}} = 0 \\
\text{linear function:} & \quad 0 < y_{\text{gpv}} < 1 \quad \Leftrightarrow \quad A_{\text{geo,gpv}} = A_{0,\text{gpv}} (1 - y_{\text{gpv}}) \\
\text{fully open:} & \quad y_{\text{gpv}} = 0 \quad \Leftrightarrow \quad A_{\text{geo,gpv}} = A_{0,\text{gpv}}
\end{aligned}$$

As the state change over the restriction is assumed to be isenthalpic, the fluid temperature right after the restriction is the same as before the restriction.

$$T_{\text{restr}} = T_1 \quad (2.16)$$

## 2.3 Intercooler Model

The intercooler is placed between Receiver 2 and Throttle 2. It cools down the compressed air/exhaust gas mixture from the PWS. In the existing test bench setup, the intercooler is realized using a water-air heat exchanger. Its output temperature is controlled such that it cannot exceed a certain level. In the model, the pressure drop over the intercooler is added to the pressure drop of Throttle 2. A separate model of the heat exchanger is thus not necessary.

## 2.4 Engine Mass Flow Model

Regarding the air system, the engine itself may be approximated as a volumetric pump, which is a device that enforces a volume flow approximately proportional to its rotational speed. Thus, the four-stroke engine aspirates its displacement volume every two revolutions.

$$V_e^* = \frac{n_e}{60} \frac{V_d}{2} \quad (2.17)$$

The volumetric efficiency  $\eta_{\text{vol}}$  describes how much the engine differs from a perfect volumetric device. Sufficient precision is reached by setting  $\eta_{\text{vol}}$  as a function of the pressure ratio over the engine.

$$\eta_{\text{vol}} = f\left(\frac{p_{\text{em}}}{p_{\text{im}}}\right) \quad (2.18)$$

The density of the gas at the engine's intake is calculated from the intake manifold pressure and temperature using the ideal gas law.

$$\rho_{\text{im}} = \frac{p_{\text{im}}}{R T_{\text{im}}} \quad (2.19)$$

The air mass flow aspirated by the engine may thus be calculated as follows:

$$\dot{m}_{\text{e,air}}^* \equiv \dot{m}_{\text{im}}^* = \rho_{\text{im}} \dot{V}_{\text{e}}^* \eta_{\text{vol}} = \frac{p_{\text{im}}}{R T_{\text{im}}} \frac{n_{\text{e}}}{60} \frac{V_{\text{d}}}{2} \eta_{\text{vol}} \quad (2.20)$$

The exhaust gas mass flow expelled by the engine is simply calculated by comparing the stoichiometric air-to-fuel ratio  $(A/F)_{\text{s}}$  with the measured air-to-fuel ratio  $\lambda_{\text{em}}$  in the exhaust manifold, neglecting the sensor dynamics of the  $\lambda$  sensor.

$$\dot{m}_{\text{e,fl}}^* \equiv \dot{m}_{\text{fl}}^* = \frac{\dot{m}_{\text{e,air}}^*}{(A/F)_{\text{s}} \cdot \lambda_{\text{em}}} \quad (2.21)$$

$$\begin{aligned} \dot{m}_{\text{e,eg}}^* \equiv \dot{m}_{\text{e}}^* &= \dot{m}_{\text{e,fl}}^* + \dot{m}_{\text{e,air}}^* = \\ &= \frac{p_{\text{im}}}{R T_{\text{im}}} \frac{n_{\text{e}}}{60} \frac{V_{\text{d}}}{2} \eta_{\text{vol}} \left( 1 + \frac{1}{(A/F)_{\text{s}} \cdot \lambda_{\text{em}}} \right) \end{aligned} \quad (2.22)$$

## 2.5 Engine Torque Model

The torque produced by the engine generally is a nonlinear function of many variables such as fuel mass in the cylinder, air-to-fuel ratio, engine speed, ignition or injection time, EGR rate, etc. In the current implementation, a useful simplification of the engine's torque and efficiency characteristics is made by the *Willans Approximation* (Heywood, 1988; Guzzella and Onder, 2004). A plot of the *brake mean effective pressure*

$$\text{BMEP} \equiv p_{\text{me}} := \frac{T q_{\text{e}} 4 \pi}{V_{\text{d}}} = \frac{T q_{\text{e}} \cdot 2 \cdot 2 \pi}{A_{\text{p}} \cdot H_{\text{s}}} \quad (2.23)$$

against the *fuel mean effective pressure*

$$p_{\text{mf}} := \frac{q_{\text{hv}} m_{\text{fl,cyc}}}{V_{\text{d}}} = \frac{q_{\text{hv}} \cdot \dot{m}_{\text{fl}}^* \cdot 2 \cdot \frac{1}{n_{\text{e}}/60}}{A_{\text{p}} H_{\text{s}}} \quad (2.24)$$

shows the affine relation between these two quantities (Fig. 2.2). Both  $p_{\text{me}}$  and  $p_{\text{mf}}$  immediately result from an energy balance over one engine cycle, i.e. two revolutions, assuming a four-stroke engine.

- The brake mean effective pressure BMEP ( $\equiv p_{\text{me}}$ ) is the pressure that has to act on the piston area ( $A_p$ ) during one full expansion stroke ( $H_s$ ) to produce the same amount of work as the real engine delivers as flywheel torque ( $Tq_e$ ) in two engine revolutions ( $2 \cdot 2\pi$ ).
- Similarly, the fuel mean effective pressure ( $p_{\text{mf}}$ ) is the pressure that has to act on the piston area ( $A_p$ ) during one full expansion stroke ( $H_s$ ) to produce the same amount of work as the real engine consumes in the form of chemical energy in the fuel mass flow ( $\dot{m}_{\text{fl}}^* \cdot q_{\text{hv}}$ ) during two engine revolutions ( $2 \cdot \frac{1}{n_e/60}$ ).

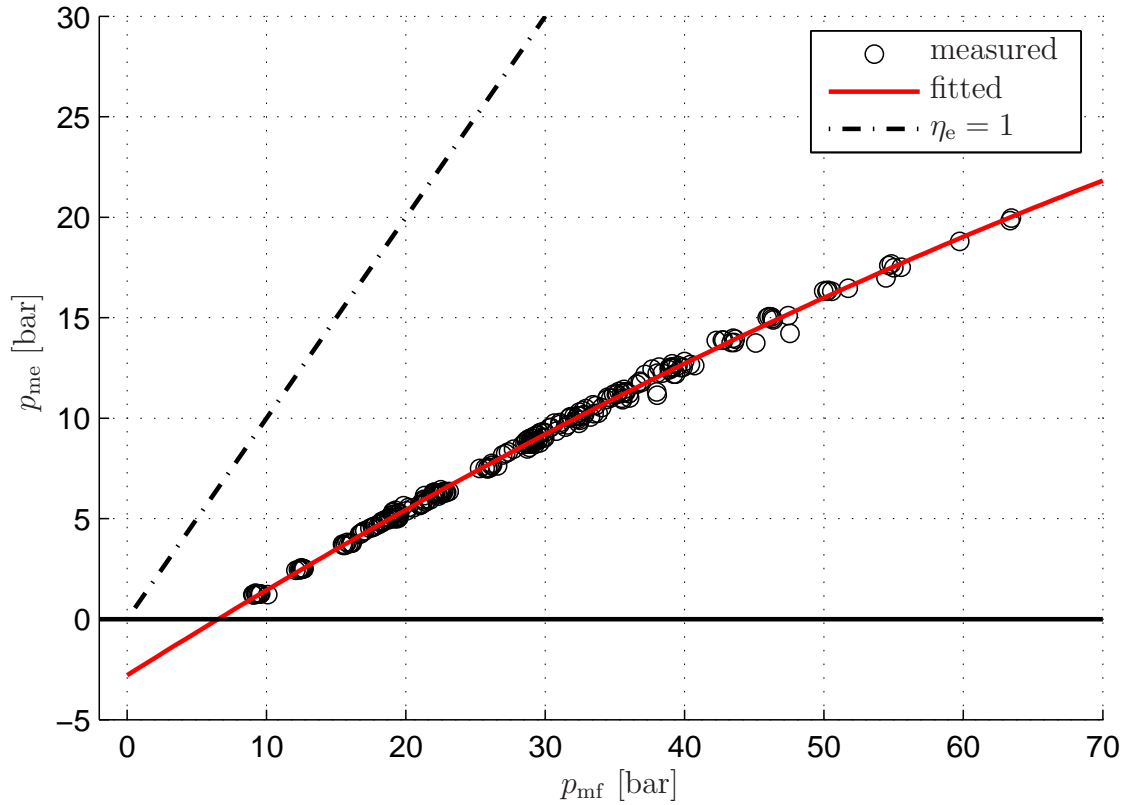


**Figure 2.2:** Identified affine Willans model of the engine efficiency for the EA111/HX95 engine

Since for some high-load operating points the measured air-to-fuel ratio  $\lambda_{\text{em}}$  significantly diverges from one (e.g. for reasons of thermal

protection of components), Equation (2.24) is augmented by the factor  $\lambda_{\text{em}}$ .

$$p_{\text{mf}} = \frac{q_{\text{hv}}^* m_{\text{fl}} 2^{\frac{1}{n_e/60}}}{V_{\text{d}}} \lambda_{\text{em}} \quad (2.25)$$

In pressure-wave supercharged engines as presented in this text, there is a high probability of occurring steady-state or transient external exhaust gas recirculation. External or internal EGR may reduce the formation of nitrogen oxide (Amstutz, 1991), but it negatively affects the thermodynamic efficiency of SI engines. In fact, increased EGR rates lead to slower burning speeds and, therefore, to a reduced thermodynamic efficiency, and thus a reduced engine torque.

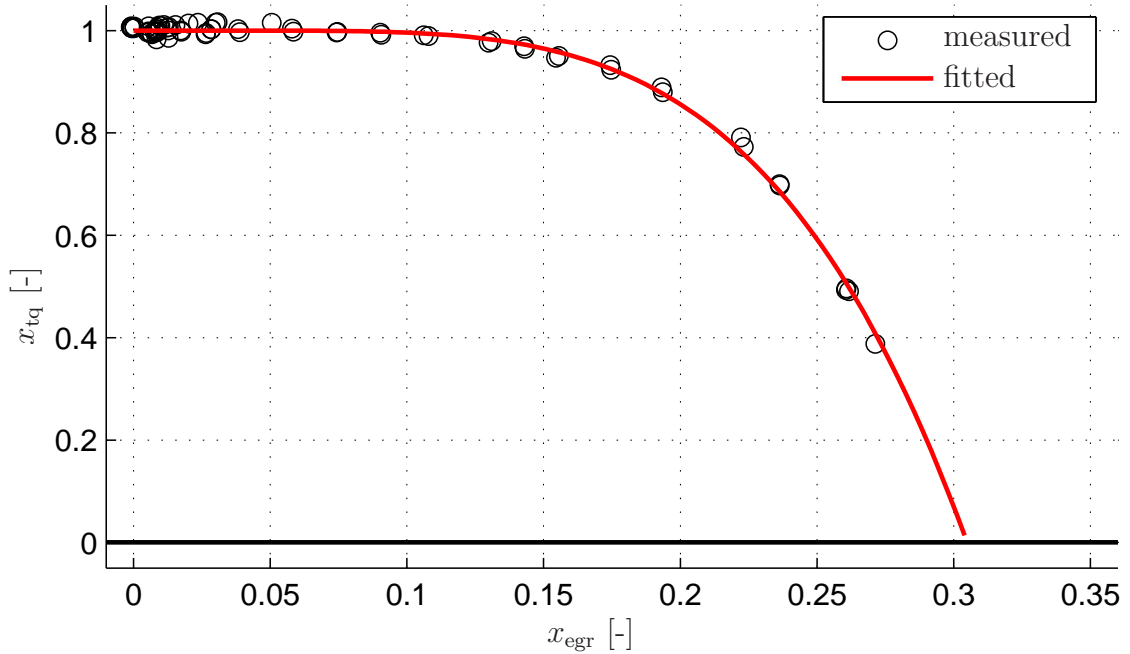


**Figure 2.3:** Identified influence of the EGR rate on the engine torque on the EA111/HX95 engine (1500 rpm)

As presented in Fig. 2.3 the EGR-dependent formulation

$$x_{\text{tq}} = 1 - k_{\text{egr}} x_{\text{egr}}^4 \quad (2.26)$$

proved to be a useful approximation for  $x_{\text{tq}}$ , describing the fraction

$$x_{\text{tq}} := \frac{Tq_{\text{e,meas}}}{Tq_{\text{e,nominal}}} = \frac{\text{measured torque}}{\text{nominal torque at } x_{\text{egr}} = 0} \quad (2.27)$$

where  $Tq_{\text{e,nominal}}$  is computed using the Willans approximation, i.e. Eqs. 2.23 to 2.25.

## 2.6 Engine Outlet Temperature Model

Eriksson (2002) suggests an affine approach for the engine-out temperature over the engine mass flow.

$$T_e = T_{e0} + \underbrace{\frac{\Delta T}{m_{e,\max}^*}}_{=c_{Te,m}^*} m_e^* \quad (2.28)$$

However, since the temperature sensors at the engine test bench could not be placed right next to the exhaust valves but only at a distance of  $\approx 80$  mm, the measured exhaust gas temperature is slightly lower. Heat transfer to the walls has a greater effect on small mass flows. An exponential model shows the measured temperature variations in Receiver 3 (Fig. 2.4).

$$T_e = T_{e0} + k_{Te,1} e^{k_{Te,2} m_e^*} \quad (2.29)$$

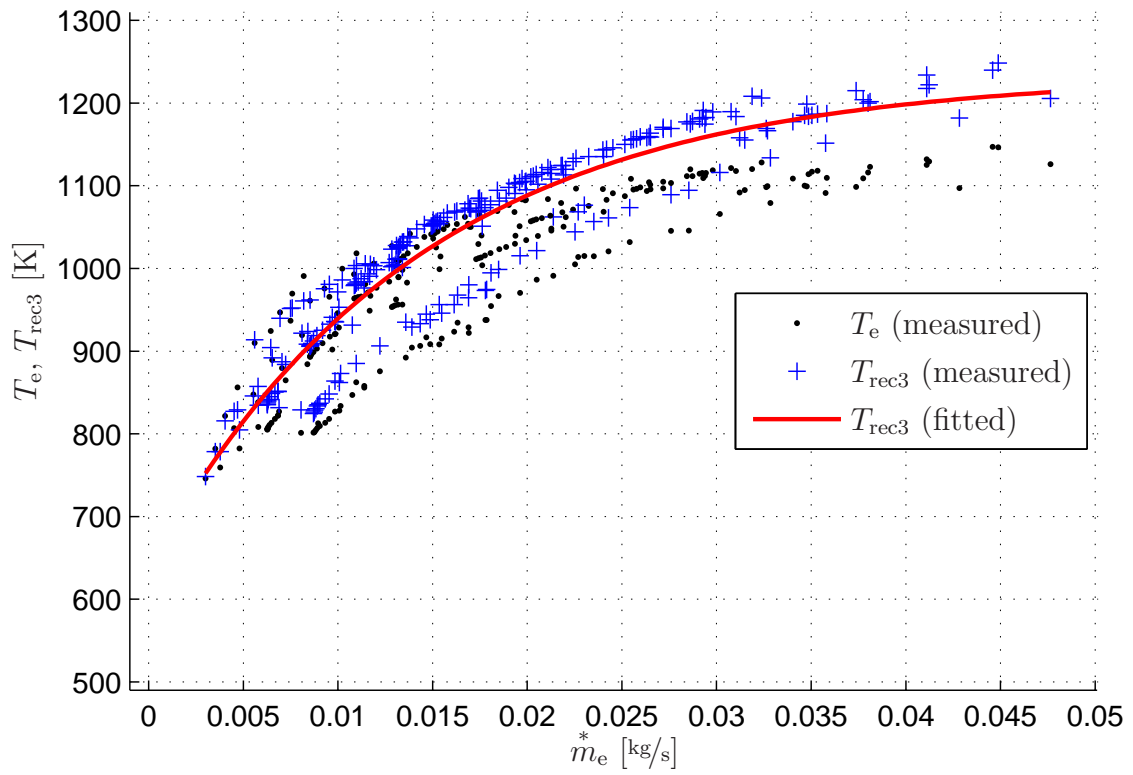


**Figure 2.4:** Measured temperatures in the exhaust manifold and in Receiver 3 on the EA111/HX95 engine: the results of an exponential approach fits the data well.

## Chapter 3

# Modeling and Validation of the Pressure-Wave Supercharger

The PWS closes the high-pressure loop between Receiver 2 and Receiver 3. Its primary objective is to transmit some of the abounding enthalpy available in the exhaust gases in Receiver 3 to the fresh air entering the PWS through Channel 1. The dynamics of this process are ten to twenty times faster than the dynamics of interest, i.e. the pressure dynamics and torque formation, which are in the order of 100 ms (Amstutz, 1991).

Modeling the PWS turned out to be the real challenge in this work. The problem is the large number of system inputs (such as  $p_{\text{rec1}}$ ,  $p_{\text{rec2}}$ ,  $p_{\text{rec3}}$ ,  $p_{\text{rec4}}$ ,  $p_{\text{gp}}$ ,  $T_{\text{rec1}}$ ,  $T_{\text{rec3}}$ ,  $T_{\text{gp}}$ ,  $y_{\text{gpv}}$ ,  $n_{\text{pws}}$ , and  $\alpha_{\text{cas}}$ ), and their sensitivity to the system outputs ( $\dot{m}_{\text{ch1}}^*$ ,  $\dot{m}_{\text{ch2}}^*$ ,  $\dot{m}_{\text{ch3}}^*$ ,  $\dot{m}_{\text{chg}}^*$ ,  $\dot{m}_{\text{ch4}}^*$ ,  $T_{\text{ch2,out}}$ ,  $T_{\text{ch4,out}}$ ). Initial experiments proved that even a small change in the value of a certain input may immediately have an effect on *all* the outputs. The high sensitivity of parts of the inputs demand special attention.

Detailed thermodynamic simulations are necessary to correctly predict the PWS mass flows and outflow temperatures. For control purposes, however, such simulations are too time-consuming. Thus, alternative approaches have been investigated. An obvious (but not feasible) solution would be to grid the space of all possible operating conditions, to measure or compute each mass flow and outflow temperature in each vertex, and to store that information for later on-line use in appropriate maps (Brand, 2005). Another

approach is to use some physical insights to separate the different influencing variables and to divide the modeling task into several low-dimensional problems. This method is applied in the work at hand.

Many different approaches have been used over the years to design pressure-wave devices. Among them, the so-called *method of characteristics* has been popular (Berchtold, 1961; Hörler, 1969; Croes, 1979; Gyarmathy, 1983; Janssens, 1992; Weber, 2001) since it offers the possibility to derive solutions graphically. Working with two diagrams in parallel, a skeleton diagram (wave diagram) and a state diagram, an estimation of the in- and outgoing mass flows is possible. Effects such as leakage, heat transfer, and friction are included in lumped parameters. More recently, however, that method has been superseded by more efficient numerical methods and have thus been reduced to determining the boundary conditions. A numerical simulation of several PWSs is presented in the works of Piechna, Paxson, and Nalim where a formulation with partial differential equations in one spatial dimension is used (Piechna, 1998b; Piechna and Lisewski, 1998; Selerowicz and Piechna, 1999; Paxson, 1995b,a, 1996; Nalim, 2000).

Currently, a powerful software called FLUENT<sup>1</sup> is available to simulate the gas dynamics of wave rotors along one, two, or three dimensions in greater detail (Piechna et al., 2004; Fraokowiak et al., 2004; Iancu et al., 2005).

In this work, both detailed thermodynamic simulations using numerical methods and a simplified approach using the method of characteristics are presented. In Section 3.1, a finite-difference model (Spring et al., 2004) is presented that is subject to a minimum of assumptions and where only a few parameters need to be identified. The model is computationally very demanding, but the method is universally applicable to very different types of PWSs and to very different operating conditions.

in Section 3.2, on the basis of this first-principle finite-difference model (FDMdl) and assuming that the PWS is operated under efficiency-optimal “tuned-in” conditions, a simplified, control-oriented mean-value model (MVMdl) is then developed.

---

<sup>1</sup>[www.fluent.com](http://www.fluent.com)



## 3.1 First-principle, Finite-difference Model (FDMdl)

After the basic principles and their application to the PWS-modeling problem are pointed out, the boundary conditions are derived and a numerical scheme for solving the partial differential equations is presented. Finally, the resulting simulated mass flows and outflow temperatures are compared with measurement data.

### 3.1.1 Physics and Governing Equations

In order to numerically simulate the unsteady processes taking place inside the wave rotor, the physics of the processes of compression and expansion need to be considered. The main principle of the wave rotor operation is based on the difference between the velocities of the compression wave and the exhaust-gas-to-air contact surface. The compression wave can move 3-4 times faster than the contact surface. This fact may be utilized to compress the air located between the compression wave and the contact surface. However, although in theory the basic compression process is very simple, in practice several secondary effects have to be taken into account.

- In practical applications, the cell has a finite width and the processes of opening and closing the cell proceed gradually.
- At the initial stage of the opening process, locally two-dimensional phenomena exist which progress with the generation of compression waves that eventually form a shock wave (Piechna and Lisewski, 1998).
- The entering hot exhaust gases transfer some energy to the colder rotor walls, while the cold fresh air is heated up by the wall.
- Existing wave rotor designs are equipped with compensating pockets, such as the gas pocket and the expansion pocket. They expand the range of the cell-wheel operating speed to still attain a reasonable efficiency and scavenging rate. The existence of such pockets connecting groups of cells demands the use of a

model that can cope with the simultaneous calculation of all cells.

- In the gap between the static casing and the rotating cell wheel, a leakage mass flow must be expected.

All these physical phenomena have to be modeled mathematically.

The main processes taking place in each cell of the cell wheel of a PWS include the formation and propagation of pressure and shock waves in the presence of moving contact surfaces and the heat transfer to the cell walls. Since the ratio of the cell length to its diameter is typically greater than ten, the simulation of these unsteady processes may be approximated by one-dimensional problem formulations.

The governing equations of gas dynamics are expressions of the law of conservation and the second law of thermodynamics (Laney, 1998). The former requires that the three fundamental quantities – mass, momentum, and energy – are neither created nor destroyed but are only redistributed or, except for mass, converted from one form to another. For a derivation of the three equations 3.1 to 3.3, please refer to Appendix B.

Conservation of mass:

$$\frac{\partial \rho}{\partial t} + \frac{\partial(\rho \cdot u)}{\partial x} = 0 \quad (3.1)$$

Conservation of momentum:

$$\frac{\partial(\rho \cdot u)}{\partial t} + \frac{\partial(\rho \cdot u^2)}{\partial x} + \frac{\partial p}{\partial x} = 0 \quad (3.2)$$

Conservation of energy:

$$\frac{\partial(\rho \cdot e_T)}{\partial t} + \frac{\partial(\rho \cdot u \cdot e_T)}{\partial x} + \frac{\partial(p \cdot u)}{\partial x} = 0 \quad (3.3)$$

As another supplement to the law of conservation, the *equations of state for a perfect gas* specify the nature and type of gas.

Ideal gas law:

$$p = \rho R T \quad (3.4)$$

Caloric equation of state:

$$e = c_v T = \frac{R}{\kappa - 1} T \quad (3.5)$$

The ideal gas law (Eq. (3.4)) can be rewritten as:

$$p = (\kappa - 1) \rho e \quad (3.6)$$

Using Eq. (3.6) together with the definition for the total energy, the expression  $e_T$  in Eq. (3.3) can be replaced by:

$$e_T = e + \frac{u^2}{2} = \frac{1}{\kappa - 1} \frac{p}{\rho} + \frac{u^2}{2} \quad (3.7)$$

The three conservation laws, Eqs. (3.1, 3.2, 3.3), and the two equations of state (3.4, 3.5) can be summarized as the *conservation form* of the *Euler equations*:

$$\frac{\partial \bar{U}}{\partial t} + \frac{\partial \bar{F}}{\partial x} = 0 \quad (3.8)$$

where

$$\bar{U} = \begin{pmatrix} \rho \\ \rho u \\ \rho e_T \end{pmatrix} \quad (3.9)$$

and

$$\bar{F} = \begin{pmatrix} \rho u \\ \rho u^2 + p \\ \rho u e_T + p u \end{pmatrix} \quad (3.10)$$

Note that the right-hand side in Eq. (3.8) is not equal to zero if effects such as leakage, friction, and heat transfer have to be considered as well. Equation (3.8) then needs to be modified by appending an additional term  $\bar{B} \neq 0$ :

$$\frac{\partial \bar{U}}{\partial t} + \frac{\partial \bar{F}}{\partial x} + \bar{B} = 0 \quad (3.11)$$

where

$$\bar{B} = \begin{pmatrix} \frac{\dot{m}_{\text{leak}}^*}{A_{\text{cell}} dx} \\ \rho f_{\text{frict}} + u \frac{\dot{m}_{\text{leak}}^*}{A_{\text{cell}} dx} \\ - \frac{\dot{Q}_{\text{conv}}^*}{A_{\text{cell}} dx} + e_T \frac{\dot{m}_{\text{leak}}^*}{A_{\text{cell}} dx} \end{pmatrix} \quad (3.12)$$

**Leakage:** Leakage through the gap between cell wheel and casing is considered at the left and right ends of a cell. The leakage term  $\dot{m}_{\text{leak}}^*$  is defined positively for a mass flowing out of the control volume:

$$\dot{m}_{\text{leak}}^* = c_d A_{\text{geo}} \sqrt{p_{\text{upstr}} \rho_{\text{upstr}}} \sqrt{\frac{2 \kappa}{\kappa - 1}} \sqrt{\Pi^{\frac{2}{\kappa}} - \Pi^{\frac{\kappa+1}{\kappa}}} \quad (3.13)$$

The pressure ratio  $\Pi$  here is defined as

$$\Pi = \frac{p_{\text{downstr}}}{p_{\text{upstr}}} \quad (3.14)$$

**Friction:** The specific friction  $f_{\text{frict}}$  is computed using the approach

$$f_{\text{frict}} = c_{\text{frict}} \frac{u |u|}{2} \frac{1}{D_{\text{cell}}} \quad (3.15)$$

where  $u$  is the gas speed,  $D_{\text{cell}}$  is the mean diameter of the control volume, and  $c_{\text{frict}}$  is the friction coefficient.

**Heat transfer:** The heat  $\dot{Q}_{\text{conv}}^*$  (convection) is transferred from fluid to wall over the boundaries of the control volume:

$$\dot{Q}_{\text{conv}}^* = -\lambda_{\text{ht}} \pi D_{\text{cell}} dx (T_{\text{gas}} - T_{\text{wall}}) \quad (3.16)$$

The heat transfer coefficient  $\lambda_{\text{ht}}$  is calculated using an approach by Woschni (1967, 1970):

$$\lambda_{\text{ht}} = 820 \cdot D_{\text{cell}}^{-0.2} \cdot p^{0.8} \cdot u^{0.8} \cdot T_{\text{gas}}^{-0.53} \quad (3.17)$$

using the units:  $D$  [m],  $p$  [MPa],  $u$  [m/s],  $T$  [K].

The set of equations condensed in Eq. (3.11) provides the core of the PWS model presented in Sect. 3.1.

### 3.1.2 Space-Time Discretization and Solving Scheme

The concurrence of compression, shock, and expansion waves in the flow field, mathematically described by the Euler Equations, requires

a method that can resolve both the shock wave motion and the gas-air contact surface motion in parallel. Tests have shown (Piechna, 1998a) that a robust technique is on hand in the *two-step Lax-Wendroff method*, which was described in 1960 by Peter D. Lax and Burton Wendroff (Lax and Wendroff, 1960).

Using this method, the space-time plane is discretized taking a finite number of nodes ( $N_{\text{nodes}}$ ) in the x-direction (space) and the t-direction (time) as depicted in Fig. 3.1. The space-time grid may also be interpreted as the movement of a cell over the time passing each channel during a complete charging/scavenging cycle.

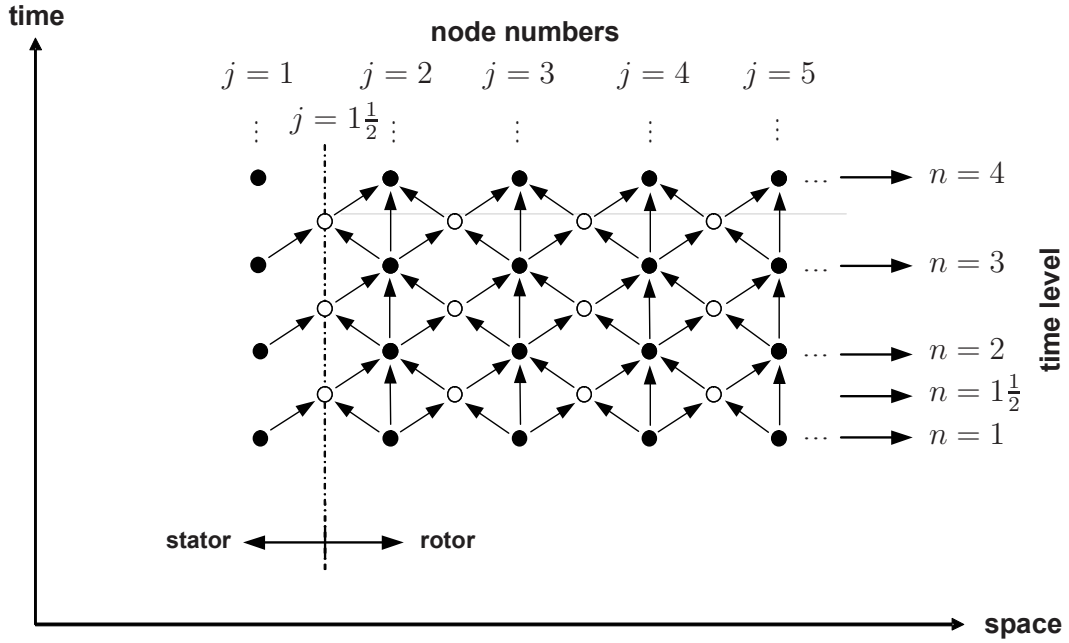


**Figure 3.1:** Space-time grid for the two-step Lax-Wendroff scheme

In the Lax-Wendroff scheme, the partial differential equations condensed in (3.11) are solved by handling the space-time grid row by row from the bottom ( $n = 1$ ) to the top. In the first (Lax) step, the intermediate points on level ( $n + 1/2$ ) are calculated using Equation (3.18).

$$\mathbf{U}_{j+1/2}^{n+1/2} = \frac{1}{2}(\mathbf{U}_j^n + \mathbf{U}_{j+1}^n) - \dots \quad (3.18)$$

$$\frac{\Delta t}{2 \Delta x}(\mathbf{F}_{j+1}^n - \mathbf{F}_j^n) + \frac{\Delta t}{4}(\mathbf{B}_{j+1}^n + \mathbf{B}_j^n)$$

For the second “Leapfrog” step, Equation (3.19) specifies the algorithm for the points on the new level ( $n + 1$ ).

$$\mathbf{U}_j^{n+1} = \mathbf{U}_j^n - \dots + \frac{\Delta t}{\Delta x}(\mathbf{F}_{j+1/2}^{n+1/2} - \mathbf{F}_{j-1/2}^{n+1/2}) + \frac{\Delta t}{2}(\mathbf{B}_{j-1/2}^{n+1/2} + \mathbf{B}_{j+1/2}^{n+1/2}) \quad (3.19)$$

The expressions  $\mathbf{U}$ ,  $\mathbf{F}$ , and  $\mathbf{B}$  are defined in Eqs. (3.9), (3.10), and (3.12). The spatial distance  $\Delta x$  is defined by the rotor length and the specified number of grid points  $N_{\text{nodes}}$  in the space direction.

$$\Delta x = \frac{L_{\text{rot}}}{N_{\text{nodes}} - 1} \quad (3.20)$$

Finding the optimal number of nodes to discretize the spatial dimension is mainly a trade-off between precision and computational costs. A large mesh width causes high numerical diffusion errors, i.e. the solutions smooth out. Other than that, there exists a numerical phenomenon called dispersion. Dispersion occurs when different spatial frequency components travel at different (frequency-dependent) speeds. Considering a shock wave or pressure step (which theoretically consist of all frequencies), dispersion errors can produce solutions with severe oscillations just upstream of the shock as shown in Fig. 3.2.

Moreover, the temporal distance  $\Delta t$  in the time direction has to be recomputed for each time step, using the stability criterion (Eq. (3.21)), where  $u$  is the local fluid speed and  $a$  is the local speed of sound.

$$\Delta t_n = \frac{\Delta x}{\max_j(|u_j^n| + a_j^n)} \quad (3.21)$$

The stability criterion Eq. (3.21) accounts for the fastest wave propagation of the values in a row of grid points of the respective time level  $n$  (Fig. 3.1). Oversized time steps can cause instabilities and can amplify dispersion errors. There exist methods that can smooth such solution areas of high gradients like e.g. the *flux corrected transport method* of Boris and Book (1973). Alternatively, in the model presented the simple and efficient method of *artificial viscosity* (Sod, 1985) is used. This scheme influences the solution in areas of high frequency oscillations only, and thus accompanies the shock wave

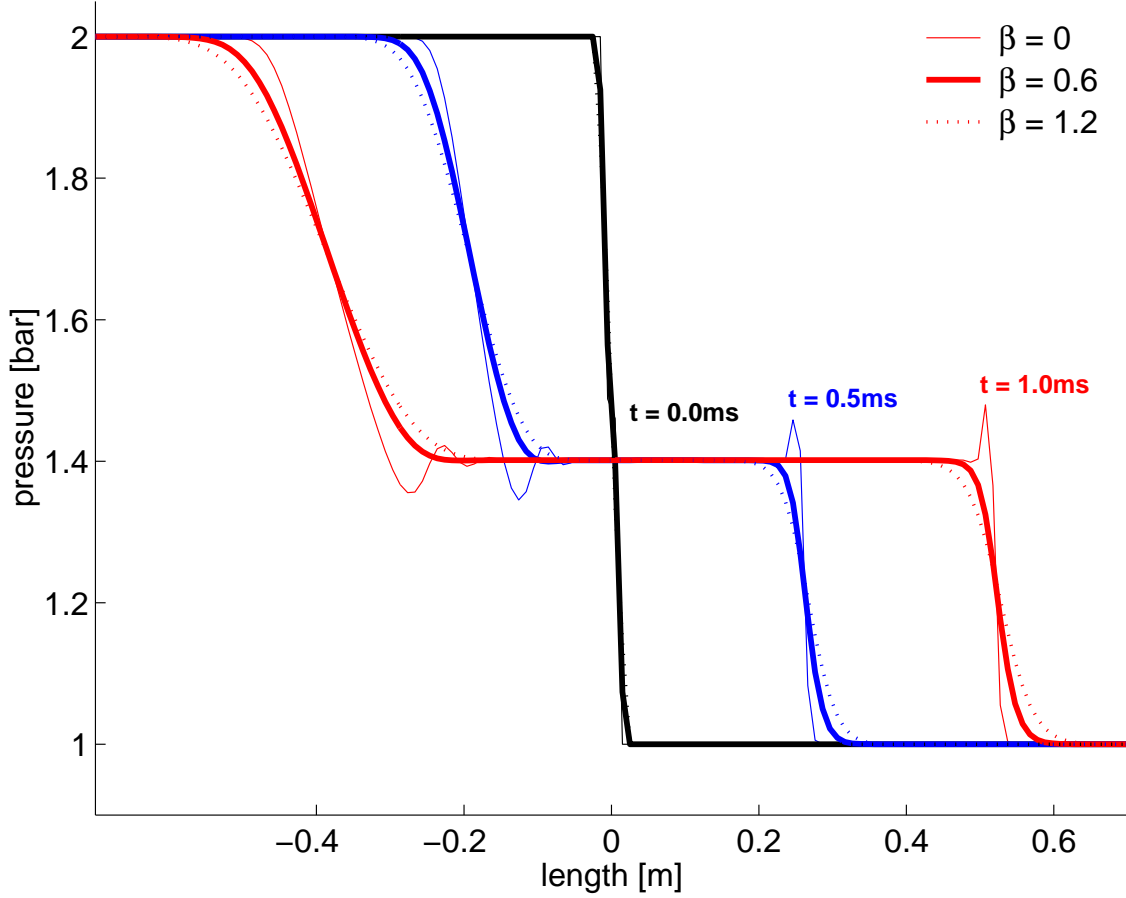


**Figure 3.2:** Dispersion errors of the Lax-Wendroff scheme. Simulated pressure in the cell for  $\beta = 0$  and smoothed solution by introducing an artificial viscosity ( $\beta = 0.6, \beta = 1.2$ )

front. The vector  $\mathbf{U}$  is then modified in a third step in the following way:

$$\begin{aligned} \mathbf{U}_j^{n+1} &= \mathbf{U}_j^{n+1} + 0.25 \beta (\mathbf{U}_{j+1}^{n+1} - 2 \mathbf{U}_j^{n+1} + \mathbf{U}_{j-1}^{n+1}) \\ 0 &\leq \beta \leq 1 \end{aligned} \quad (3.22)$$

The best results were obtained taking  $\beta = 0.6$ .

### 3.1.3 Boundary Conditions

One important issue in solving any partial differential equation is the determination of the boundary conditions. In the case at hand, there are not only inflows to and outflows from the cell, but the cells also can be closed. The reader may have recognized that the numerical

scheme described before is fully symmetrical and thus needs well-defined values for all nodes of the first time level ( $n = 1$ ) as well as for the two nodes on the far left ( $j = 1$ ) and far right-hand side ( $j = N_{\text{nodes}}$ ) of each time level, respectively. The columns at the far left and far right ends of the space-time grid are considered to lie “outside” of the cell wheel and to contain the boundary conditions used to solve the partial differential Equation (3.11) for each time step. Different cases have to be distinguished when the cell is passing along the channels:

**Active cross-section:** Both ends of the cell may be partially or fully opened or closed. It is also possible that two adjacent channels are touched by the same cell at the same time, e.g. Channel 3 and the gas pocket channel.

**Flow direction:** The fluid at the end of any channel may change its general flow direction. The outflow from the cell to the receiver may be choked, which would mean that the fluid velocity has reached sound velocity, if the stagnation pressure in the receiver is very low. The model also must describe overflow effects over the cell from one channel to another, an effect that may occur when groups of channels pass the expansion pocket.

**Fluid parameters:** Gas parameters in the receiver may be different from that of the fluid in the cell, resulting in a discontinuity in entropy, temperature, and density.

In Fig. 3.3, the three possible cases for the left end of the cell are presented in greater detail:

(a) The cell is **closed** by the casing wall. For the prediction of the boundary conditions here, the mirror principle is used, which means that the boundary values for  $\rho$ ,  $u$ , and  $p$  of the “new” time level ( $n + 1$ ) are mirrored from the second node (inside the cell wheel) to the first node (outside the cell wheel) of the “new” time level ( $n + 1$ ):

$$\begin{aligned}\rho_1^{\text{new}} &= \rho_2^{\text{new}} \\ u_1^{\text{new}} &= -u_2^{\text{new}} \\ p_1^{\text{new}} &= p_2^{\text{new}}\end{aligned}\tag{3.23}$$



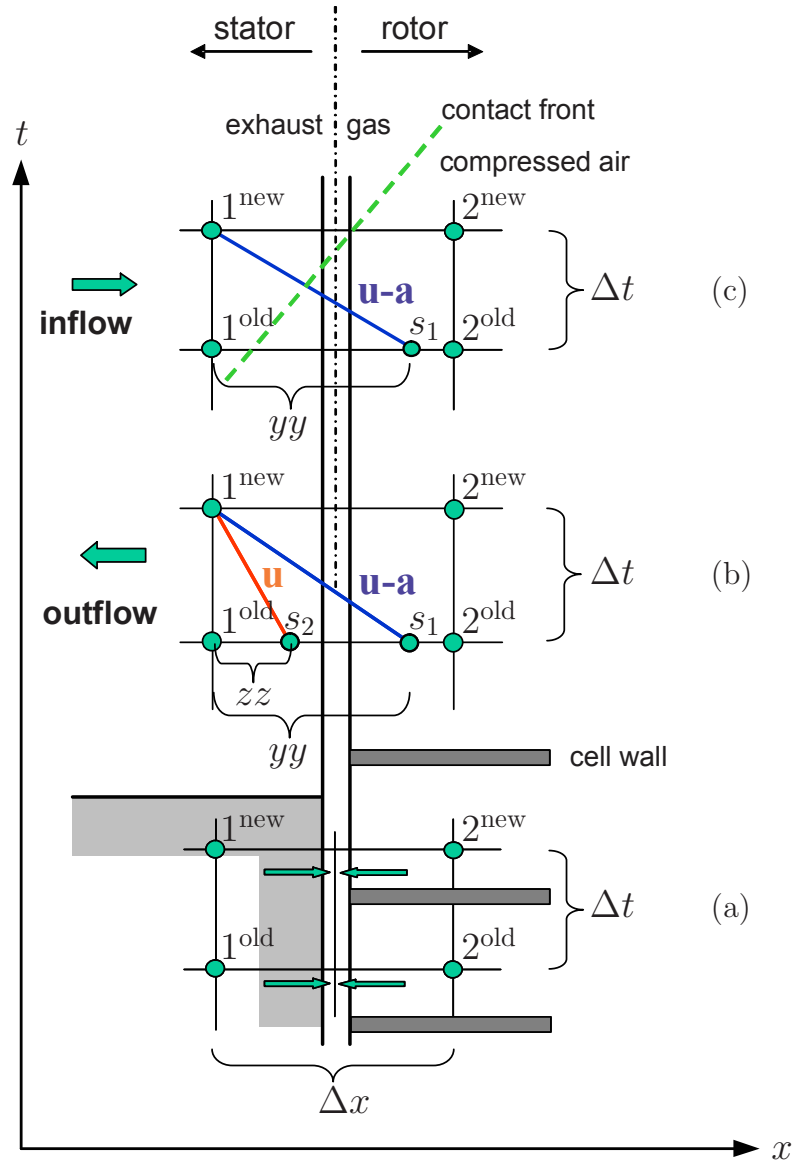


**Figure 3.3:** The three possible boundary conditions for the left side: (a) .. closed end, (b) .. outflow from the cell, (c) .. inflow to the cell

(b) The cell is open-ended to the channel such that **outflow** from the cell to the receiver prevails. The pressure  $p_1^{\text{new}}$  in the new boundary point is assumed to be equal to the receiver pressure  $p_{\text{rec}}$  unless outflow conditions have reached critical values. The speed of sound at the new point is equal to the speed of sound of the fluid at starting point 1

(s1) expanded isentropically from  $p_{s1}$  to  $p_1^{\text{new}}$ :

$$a_1^{\text{new}} = a_{s1} \left( \frac{p_1^{\text{new}}}{p_{s1}} \right)^{\frac{\kappa-1}{2\kappa}} \quad (3.24)$$

The speed of sound is the speed at which small disturbances propagate through a substance measured with respect to the movement of the substance (see also App. D). For a perfect gas, this is as follows:

$$a = \sqrt{\kappa \cdot R \cdot T} \quad (3.25)$$

The (generally) unsteady relation between point s1 at the old time level inside the cell wheel and the new boundary node (outside of the cell wheel) must fulfill the so-called *Compatibility Equation* (3.26) along the characteristic line (3.27), depicted as  $u - a$  in Fig. 3.3 (b):

$$(a_1^{\text{new}} - a_{s1}) = \frac{\kappa - 1}{2} (u_1^{\text{new}} - u_{s1}) \quad (3.26)$$

$$\frac{dx}{dt} = u - a \quad (3.27)$$

The solution of Eqs. (3.24)-(3.26) results in a linear equation for the outlet velocity. Additionally, the variable for the gas density at the outlet can be isolated using the isentropic relation along the path line (point s2  $\rightarrow$  point 1<sup>new</sup>), Equation (3.28).

$$\rho_1^{\text{new}} = \rho_{s2} \left( \frac{p_1^{\text{new}}}{p_{s2}} \right)^{\frac{1}{\kappa}} \quad (3.28)$$

(c) When the cell end is opened and **inflow** into the cell dominates, between the receiver and the inlet cross-section of the cell an isentropic quasi-steady state change is assumed to occur. This may be described by the *energy equation* in the form:

$$\frac{a_{\text{rec}}^2}{\kappa - 1} = \frac{(a_1^{\text{new}})^2}{\kappa - 1} + \frac{(u_1^{\text{new}})^2}{2} \quad (3.29)$$

In the beginning stage of exhaust gas expansion into the cell, a **discontinuity surface** (contact front) as depicted in Fig. 3.3 (c)

may exist between node 1 and node 2. Both sides of the discontinuity surface experience the same pressure and flow velocity, but generally different temperatures and densities. Due to the possibility of different entropy levels existing between incoming and pre-existing fluids in the cell, appropriate equations describing the entropy discontinuity have to be added here. On a constant pressure line, the entropy ratio over the discontinuity surface may be represented by the ratio of the speeds of sound. Introducing an arbitrarily set reference pressure  $p_{\text{ref}} = 1 \text{ bar}$ , the speeds of sound at  $p_{\text{ref}}$  on both sides of the discontinuity surface can be calculated as follows:

$$a_{\text{hot,ref}} = a_{\text{rec}} \left( \frac{p_{\text{ref}}}{p_{\text{rec}}} \right)^{\frac{\kappa-1}{2\kappa}}, \quad a_{\text{cold,ref}} = a_{s1} \left( \frac{p_{\text{ref}}}{p_{s1}} \right)^{\frac{\kappa-1}{2\kappa}} \quad (3.30)$$

where  $a_{\text{hot,ref}}$  is the speed of sound in the exhaust gas expanded isentropically from the receiver pressure, while  $a_{\text{cold,ref}}$  is the speed of sound in the compressed air expanded isentropically from  $p_{s1}$  to the reference pressure. Once the entropy ratio  $\Pi_S$  is known on the level of  $p_{\text{ref}}$ , the same ratio can be used on the pressure level  $p_1^{\text{new}}$  as depicted in Fig. 3.4.

$$\Pi_S := \frac{s_{\text{hot}}}{s_{\text{cold}}} = \frac{a_{\text{hot,ref}}}{a_{\text{cold,ref}}} \stackrel{!}{=} \frac{a_{\text{hot}}}{a_{\text{cold}}} = \frac{a_1^{\text{new}}}{a_{\text{cold}}} \quad (3.31)$$

The introduction of a reference pressure is necessary since the pressure  $p_1^{\text{new}}$  is not yet known as it was in the case (b). Furthermore,  $a_{\text{cold}}$  can be computed again using the compatibility equation along the characteristic line from point  $s1$  to the discontinuity:

$$(a_{\text{cold}} - a_{s1}) = \frac{\kappa - 1}{2} (u_1^{\text{new}} - u_{s1}) \quad (3.32)$$

Combining Eqs. (3.29)-(3.32) yields a quadratic equation in  $u_1^{\text{new}}$ . Using again the isentropic relations, the pressure  $p_1^{\text{new}}$  and the density  $\rho_1^{\text{new}}$  can then be calculated from the receiver state:

$$\frac{p_1^{\text{new}}}{p_{\text{rec}}} = \left( \frac{a_1^{\text{new}}}{a_{\text{rec}}} \right)^{\frac{2\kappa}{\kappa-1}}, \quad \frac{\rho_1^{\text{new}}}{\rho_{\text{rec}}} = \left( \frac{a_1^{\text{new}}}{a_{\text{rec}}} \right)^{\frac{2}{\kappa-1}} \quad (3.33)$$

A last consideration is necessary to find the starting points  $s1$  and  $s2$  of the characteristic line and the particle line which exactly

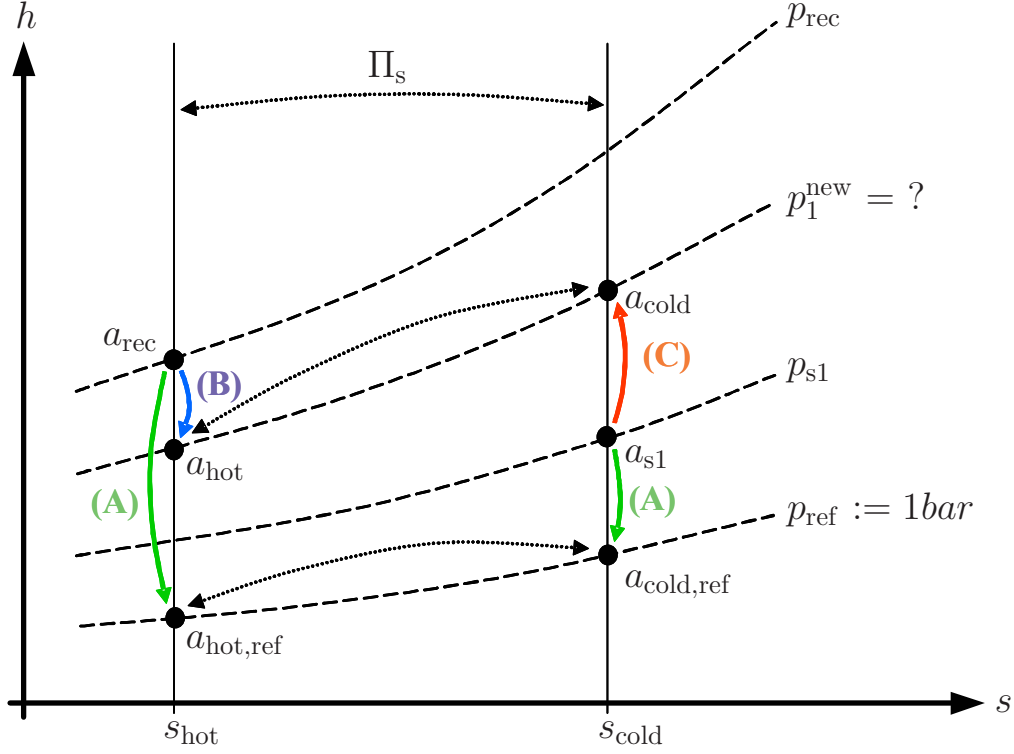


**Figure 3.4:** Enthalpy-entropy diagram for inflow conditions:  $s_{\text{hot}}$  is the entropy level of the inflowing gas whereas  $s_{\text{cold}}$  is the entropy level of the air inside the cell. (A) The isentropic equation (3.30) relates the speeds of sound at levels  $p_{\text{ref}}$  with  $p_{\text{rec}}$  and  $p_{s1}$ , respectively.

(B) The energy equation (3.29) links the speed of sound at level  $p_{\text{rec}}$  to the speed of sound at the unknown pressure level of the hot gas in the inlet cross section.

(C) The compatibility equation (3.32) connects the speeds of sound and the fluid velocities of both hot and cold gases along the characteristic line.

hits the boundary point  $1^{\text{new}}$  at the proper time. From the stability criterion,  $s1$  may be limited to the area located between the boundary node and nearest inner node. An adequate position may be found by interpolating the flow parameters between the two nodes on the actual time level:

$$u_{s1} = u_1^{\text{old}} + yy \cdot (u_2^{\text{old}} - u_1^{\text{old}}) \quad (3.34)$$

$$a_{s1} = a_1^{\text{old}} + yy \cdot (a_2^{\text{old}} - a_1^{\text{old}}) \quad (3.35)$$

Using these values, the condition for the characteristic line can be set up:

$$yy \cdot \Delta x = -(u_{s1} - a_{s1}) \Delta t \quad (3.36)$$

Starting from the point  $s1$  between node  $1^{\text{old}}$  and node  $2^{\text{old}}$ , the corresponding characteristic line will exactly hit the first node  $1^{\text{new}}$

of the new level. Similar conditions can be derived for  $zz$  to define the particle path starting from point  $s2$  and passing node  $1^{\text{new}}$ :

$$u_{s2} = u_1^{\text{old}} + zz \cdot (u_2^{\text{old}} - u_1^{\text{old}}) \quad (3.37)$$

$$zz \cdot \Delta x = -u_{s2} \Delta t \quad (3.38)$$

### 3.1.4 Pressure and Temperature Distributions

Using the boundary conditions as described in Section 3.1.3 and the solving procedure as presented in Section 3.1.2, the partial differential equation derived in Section 3.1.1 can be solved for the entire space-time plane. Since the charging process is a cyclic process, the states in the initial row ( $n = 1$ ) and in the final row need to have similar values. Therefore, the final values are used as initial inputs and the solving procedure is repeated several times.

Eventually, the states such as pressure, temperature, density, and fluid velocity can be presented graphically as they were in Fig. 3.5 for pressures. Moreover, the states in the boundary nodes can be used for calculating the channel and leakage mass flows. By integration of the fluid velocities, particles can be traced along a charging cycle. In Fig. 3.5, three more PWS-typical issues become visible.

- Shock waves are built up by superposition of pressure waves. Since the density of the fluid behind the pressure wave is slightly higher than that of the fluid in front, pressure waves that start later are faster and then reach the front of the initial wave. After a certain time (or length), the shock wave has reached its final stage. This is visible in the triangle of the first shock wave starting when Channel 3 opens.
- For well-tuned charging cycles, the reflected first shock wave exactly returns to the left end when Channel 3 closes. If the cell-wheel speed is too low, the wave arrives earlier and triggers an expansion wave that accelerates the fluid towards the left. Hence, a backflow into Channel 3 occurs.
- The pressure equalization among cells that pass the expansion pocket mentioned earlier increases the pressure level in the low-

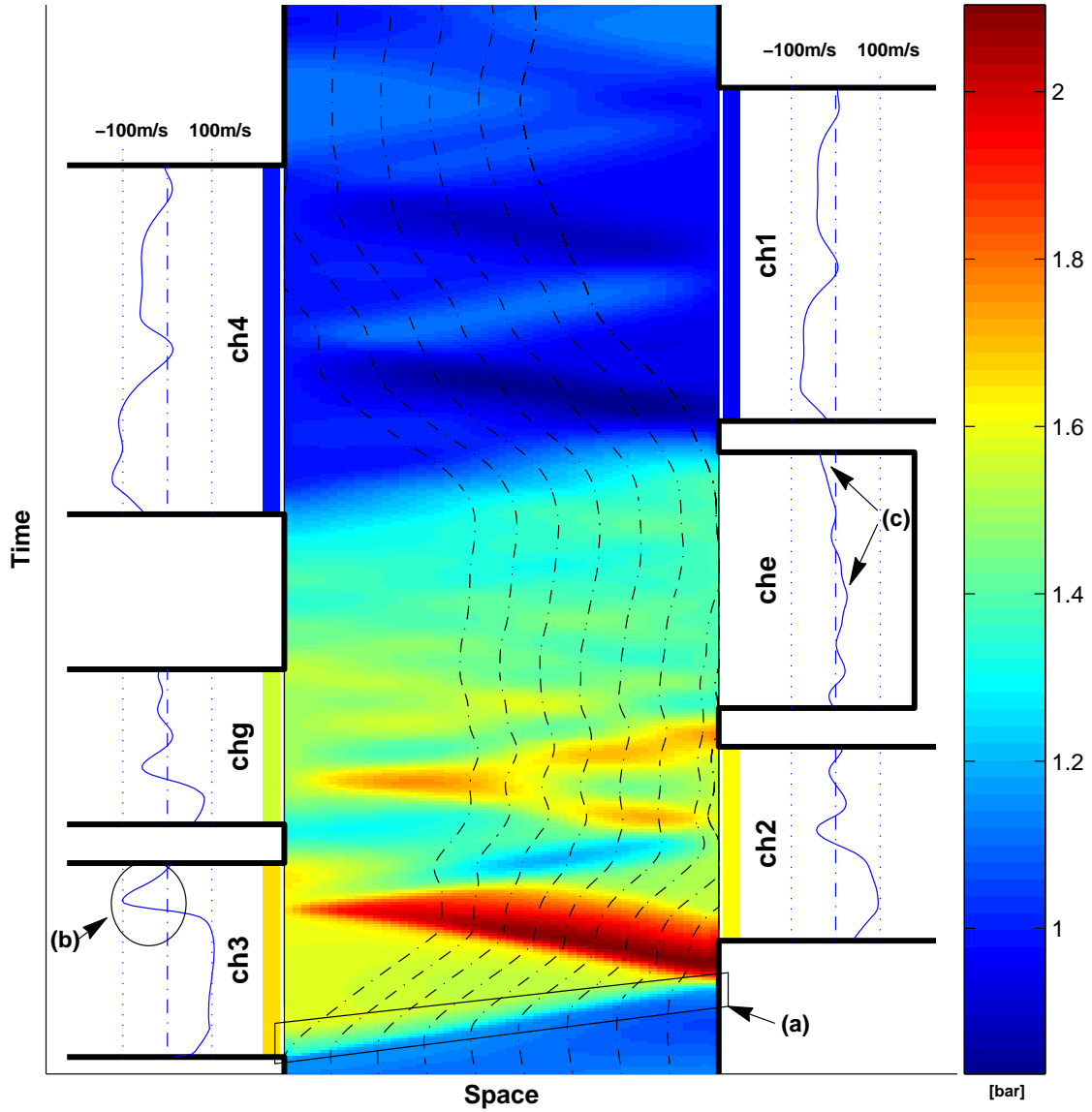


**Figure 3.5:** Pressure distribution over a cycle (pressure according to color bar), fluid velocities in the channels (blue solid curves at the boundaries), and particle paths (black dash-dotted lines). Shock-wave build-up (a), back-flows into channels (b), and equalization of pressure (c).

Note that for this figure, channel geometry and pressure and temperature boundary conditions are arbitrarily chosen, i.e. they do not coincide with values measured on the EA111/HX95 engine system.

pressure part and therefore improves the scavenging of the cells. This effect can be verified with the model.

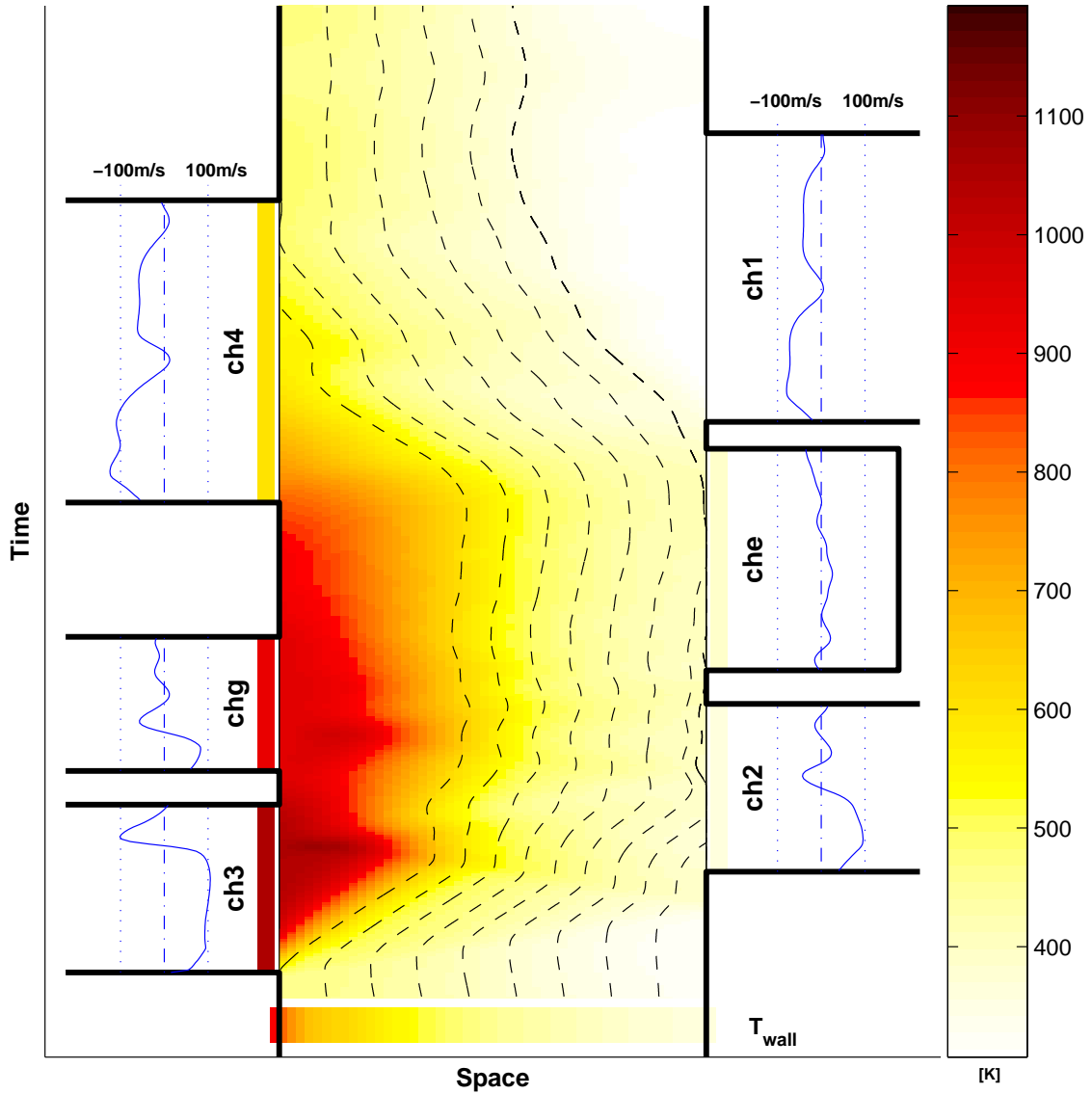


**Figure 3.6:** Temperature distribution over a cycle, similar to the pressure distribution above. The temperature of the entering hot exhaust gas drops immediately due to heat transfer into the cold fresh air and to the wall (cell wheel). The horizontal bar at the bottom illustrates the temperature profile in the cell wheel in the axial direction.

### 3.1.5 Sensitivity Analysis

Having such a sophisticated model at hand, it is interesting to investigate the influences of model parameters and model inputs. In addition, if the PWS model is used in a loop with an engine model, the input/output behavior is critically important for calculation and stability reasons. The *sensitivity* of a system in this context is defined

as representing a normalized gain from a certain system input  $u$  to an output  $y$ , referring to specified nominal values:

$$S(u, y) = \frac{\frac{y - y_{\text{nom}}}{y_{\text{nom}}}}{\frac{u - u_{\text{nom}}}{u_{\text{nom}}}} \quad (3.39)$$

Six typical operating points in the engine map were chosen to demonstrate the sensitivity. The measurements are taken at low (10 Nm) and at medium load ( $\approx 100$  Nm) at engine speeds of 1000, 2000, and 3000 rpm.

In Figure 3.7 the sensitivities of the mass flows of  $\pm 5\%$  versus the receiver pressures are plotted against the nominal mass flows. This means that for each operating point, the measured mass flow refers to  $y_{\text{nom}}$  and the measured pressure to  $u_{\text{nom}}$ . Increasing or reducing one specific pressure by  $+5\%$  or  $-5\%$  ( $\rightarrow u$ ), holding all the other inputs fixed, causes all mass flows to increase or decrease, too ( $\rightarrow y$ ). According to Eq. (3.39), the fraction of the relative differences then is the sensitivity.

The sensitivities are plotted over the nominal mass flows  $u_{\text{nom}}$ . Generally, higher sensitivities are to be expected for low mass flows. For part-load operating conditions of the engine (low mass flows), they can represent up to 40 or more. Considering the variation of the input  $u$  of  $-5\%$

$$\frac{u - u_{\text{nom}}}{u_{\text{nom}}} = -0.05 \quad (3.40)$$

a sensitivity of 40 means that the output  $y$  is equal to  $-y_{\text{nom}}$  i.e. that the mass flows in the opposite direction. From Eq. (3.39) thus follows:

$$\frac{y - y_{\text{nom}}}{y_{\text{nom}}} = 40 \cdot (-0.05) \quad (3.41)$$

hence

$$\frac{y}{y_{\text{nom}}} - 1 = -2 \quad (3.42)$$

and

$$y = -y_{\text{nom}} \quad (3.43)$$

In general, the low-pressure-part mass flows  $\dot{m}_{\text{ch1}}^*$  and  $\dot{m}_{\text{ch4}}^*$  are more sensitive to pressures than the high-pressure part mass flows  $\dot{m}_{\text{ch2}}^*$  and  $\dot{m}_{\text{ch3}}^*$ .



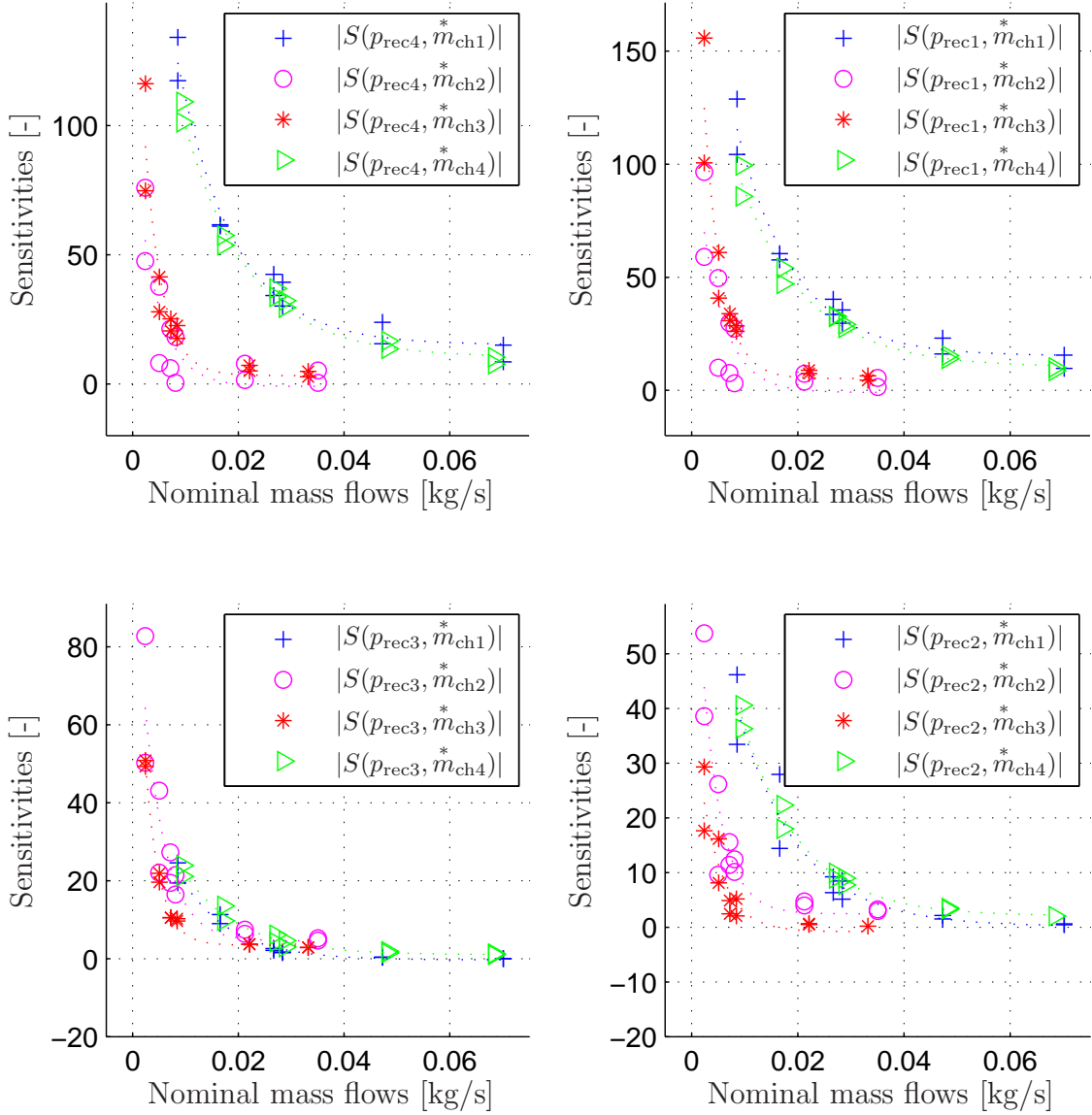


**Figure 3.7:** Sensitivities of mass flows versus pressures. Note: scaling varies

The temperatures  $T_{\text{rec3}}$  and  $T_{\text{rec1}}$  only show a relatively weak and rather constant influence on the mass flows (Fig. 3.8).

The variations of the friction parameter  $c_{\text{frict}}$  of  $\pm 5\%$  and the wall temperature  $T_{\text{wall}}$  are shown in Fig. 3.9. The parameter  $c_{\text{frict}}$  only weakly affects the mass flows. However, it is important to guess the wall temperature  $T_{\text{wall}}$  quite well, mainly for low mass flows since its influence is considerable.

Recapitulating, the mass flows as main outputs are extremely sensitive to pressure inputs and heat transfer effects. In contrast,

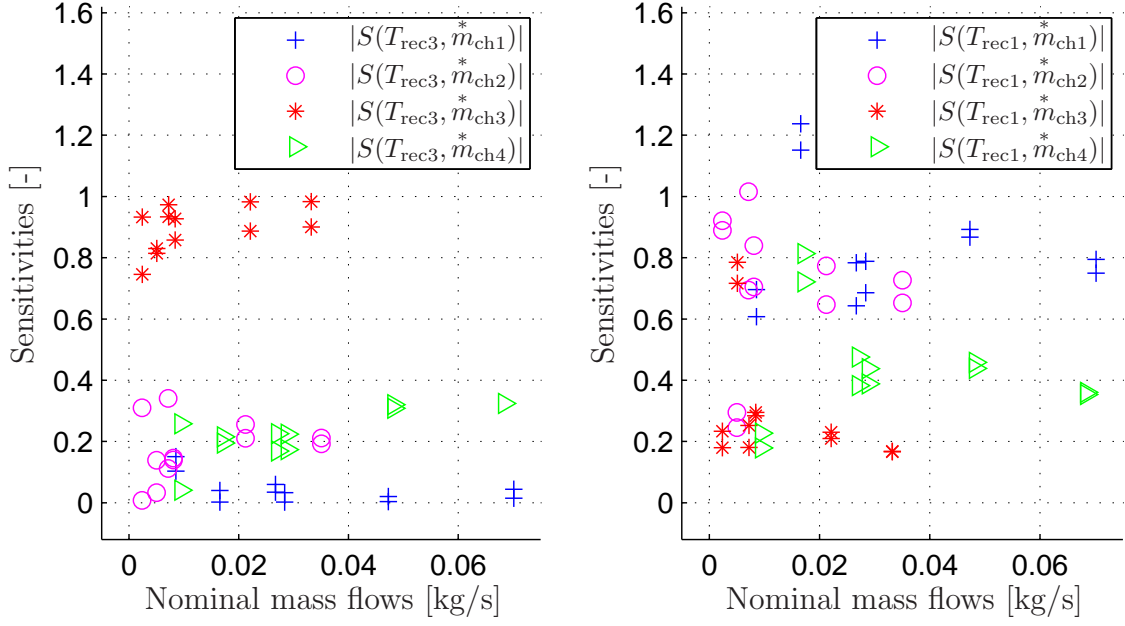


**Figure 3.8:** Sensitivities of mass flows versus temperatures

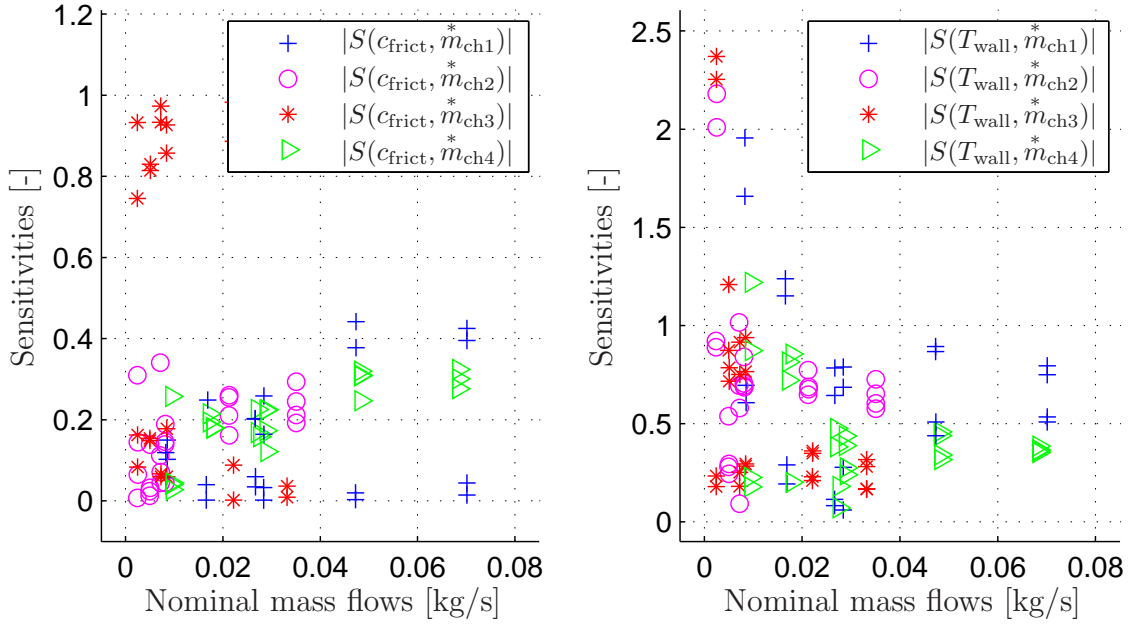


**Figure 3.9:** Sensitivities of mass flows versus friction coefficient, wall temperature, and heat transfer parameter

the temperature inputs and friction model parameters are of much smaller significance.

### 3.1.6 The Influence of Leakage

For the design and operation of PWSs an important question remaining open is the influence of leaking mass between the cell wheel and the casing. Assuming a high-load operating point ( $p_{\text{rec}2} = 2.1 \text{ bar}$ ,  $p_{\text{rec}3} = 2 \text{ bar}$ ), shown in Fig. 3.10, subplot (a), the left gap width  $d_{\text{gap,L}}$  (hot side) was varied in the range of 0 to 200  $\mu\text{m}$  holding the right gap  $d_{\text{gap,R}}$  (cold side) fixed at 0  $\mu\text{m}$  and 100  $\mu\text{m}$ , respectively. In the same way, the right gap width was varied for a fixed  $d_{\text{gap,L}}$  in subplot (b). As expected, the leakage mass flows on both sides increase with an increasing gap width. Taking the sum of both left and right leakage mass flows, for typical gap widths of 100  $\mu\text{m}$  on both sides, the model confirms estimations made by Hörler (1969), according to which the leakage mass flowing into the casing can add up to 10% of  $\dot{m}_{\text{ch}2}^*$ .

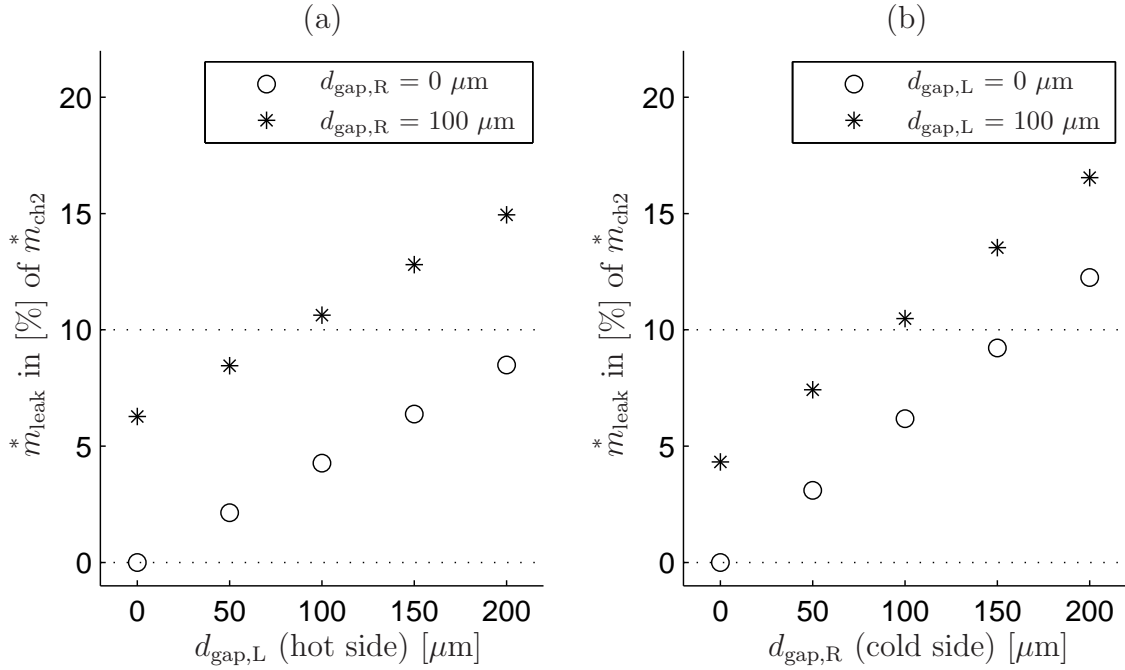


**Figure 3.10:** Leakage mass flows over gap widths (normalized with  $\dot{m}_{\text{ch}2}^*$ ): Subplot (a): left gap width  $d_{\text{gap,L}}$  is varied, right gap width  $d_{\text{gap,R}}$  is held fixed for 0  $\mu\text{m}$  and 100  $\mu\text{m}$ , respectively. Subplot (b): vice-versa ( $p_{\text{rec}2} = 2.1 \text{ bar}$ ,  $p_{\text{rec}3} = 2 \text{ bar}$ )

In Figure 3.11, the influence of leakage on channel mass flows is depicted in greater detail. Generally, leakage reduces all mass flows, except  $\dot{m}_{\text{ch}3}^*$ , where the mass flow increases very weakly, see subplot (c).

The lower pressure level caused by leakage negatively affects all mass flows. This “indirect” influence is more important than the lost mass itself. Moreover, all mass flows are more sensitive to the variation of  $d_{\text{gap,R}}$ , the right gap width on the “cold” side, since the pressure maximum is generally close to the edge when Channel 2 opens (see Fig. 3.5). However, a lower pressure level will not only result in a reduced charger efficiency, but it can also harm *scavenging conditions* and may therefore cause problems at lower operating points and during transient operation.

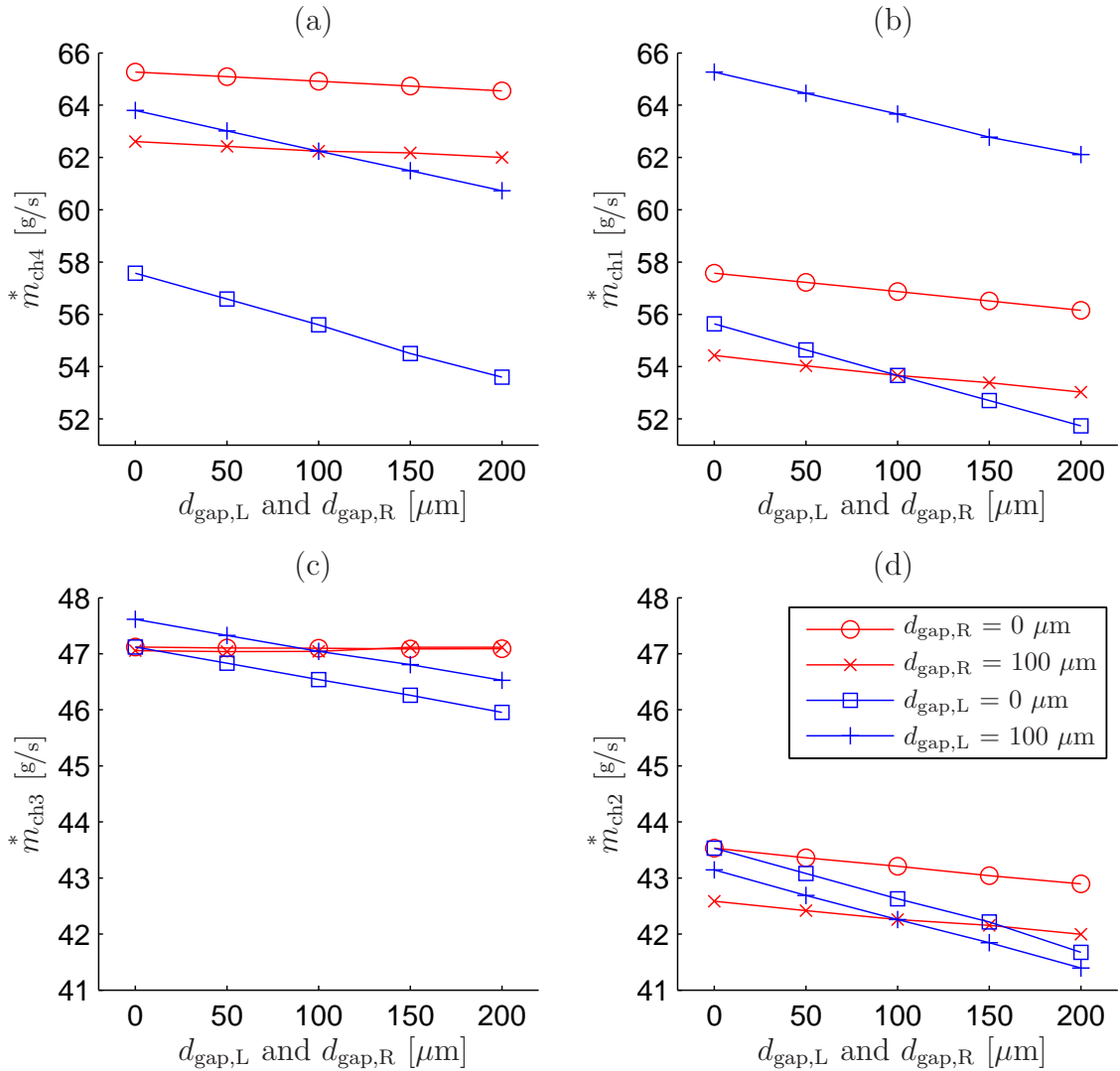


**Figure 3.11:** Influence of leakage on the four channel mass flows ( $\dot{m}_{\text{ch1}}$  to  $\dot{m}_{\text{ch4}}$ ): both left and right gap width are varied while the other gap is fixed at  $0 \mu\text{m}$  and  $100 \mu\text{m}$  ( $p_{\text{rec2}} = 2.1 \text{ bar}$ ,  $p_{\text{rec3}} = 2 \text{ bar}$ )

### 3.1.7 Validation of the Finite-Difference Model

In this section, results of the finite-difference model are compared to measurement data from two PWS engine systems.

On both systems, the lumped pressure in each receiver is captured by measuring the static pressure through an opening in the piping. In each air/gas inlet/outlet channel, pressure and temperature data are captured and averaged during 30 s to obtain the steady-state measurement results as presented in Figs. 3.14 and 3.15. However, these pressure data do not exactly match the boundary values used in the Lax-Wendroff scheme. This is due to the facts that, first, the pressure is measured a certain distance from the corresponding channel cross-section (Fig. 3.12) and, second, no information is available about the pressure distribution over the entire cross-section. Therefore, a slight difference between the measured lumped value and the uniformly distributed values that are used to form the boundary condition in the first column of nodes of the space/time grid has to be taken into account.

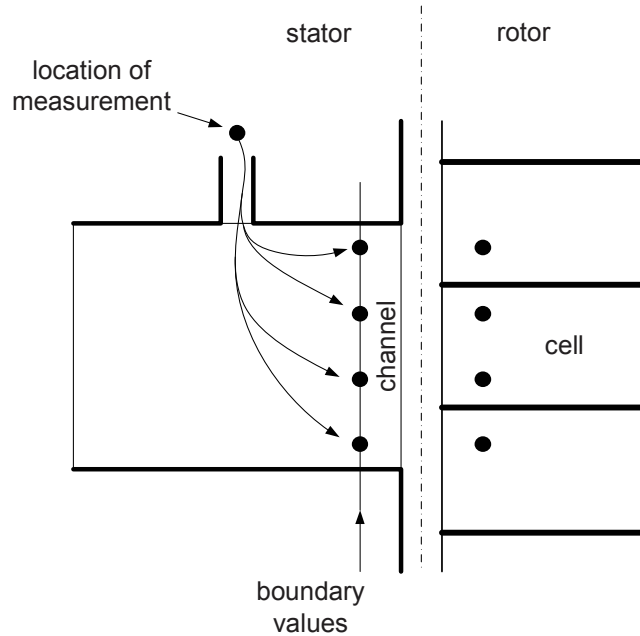


**Figure 3.12:** Assumptions for boundary values: the measured value may not directly be used as boundary condition for the Lax-Wendroff scheme due to the distance from recording point to channel end. Furthermore, there is no information about the pressure distribution in the channel. Constant pressure and temperature values are assumed over the entire channel cross-section.

As shown in Fig. 1.4, the PWS is generally modeled as a producer and a consumer of mass and energy, respectively, driven by pressure and temperature in the surrounding receivers. As shown in the block PWS in Fig. 3.13, receiver pressures and  $T_{\text{rec1}}$  and  $T_{\text{rec3}}$  thus are the driving signals, whereas the channel mass flows are the driven signals.

Considering the high sensitivity of the mass flows to pressure errors, as described in Sect. 3.1.5, the measured lumped pressures may not be used as inputs. Rather, as shown in the block PWS & Rec in Fig. 3.13 the core PWS model is extended by four receivers. The channel mass flows  $\dot{m}_{\text{ch1}}^*$ ,  $\dot{m}_{\text{ch2}}^*$ ,  $\dot{m}_{\text{ch3chg}}^*$ , and  $\dot{m}_{\text{ch4}}^*$ , together with the inflowing temperatures  $T_{\text{rec1}}$  and  $T_{\text{rec3}}$  and the actuator signals  $y_{\text{gpv}}$ ,  $n_{\text{pws}}$ , and  $\alpha_{\text{cas}}$  then appear as system inputs for the *PWS & Rec* system. The receiver pressures  $p_{\text{rec1}}$ ,  $p_{\text{rec2}}$ ,  $p_{\text{rec3}}$ , and  $p_{\text{rec4}}$  and the temperatures  $T_{\text{rec2}}$  and  $T_{\text{rec4}}$  are redefined as system outputs and may be compared to their corresponding measured, lumped values. Using this method the sensitivities of the results on measuring errors are significantly reduced.

The receiver pressures and temperatures, which serve as boundary conditions for the FDMdl, are calculated using the approaches described in Sect. 2.1. In Fig. 3.14, the comparison of mass flows, pressures, and temperatures at the boundaries of the system “PWS” is presented for six operating points. The measurements are taken from the 1 liter VW GOL test bench engine equipped with the HYPREX PWS at low (10 Nm) and at medium load ( $\approx 100$  Nm) at engine speeds of 1000, 2000, and 3000 rpm, all points being recorded with the gas pocket valve closed.

The receiver model adjusts the receiver and pocket pressures and temperatures in accordance with the mass and enthalpy flows that are given at the boundaries of system “PWS & Rec”. After three PWS cycles, the simulated pressure values correspond to the measurement results with an error of less than 6%, except for one point in the series of  $p_{\text{rec2}}$  which is diagnosed to be due to a sensor failure. Since pressure  $p_{\text{rec4}}$  in Receiver 4 and the temperatures  $T_{\text{rec2}}$  and  $T_{\text{rec4}}$  were held constant, these values match exactly. The values of  $T_{\text{rec3}}$  and  $T_{\text{gp}}$  are too low. Additional measurements showed that the temperature in Receiver 3 varies over 150 K, depending on how deep the sensor is inserted in the pipe.

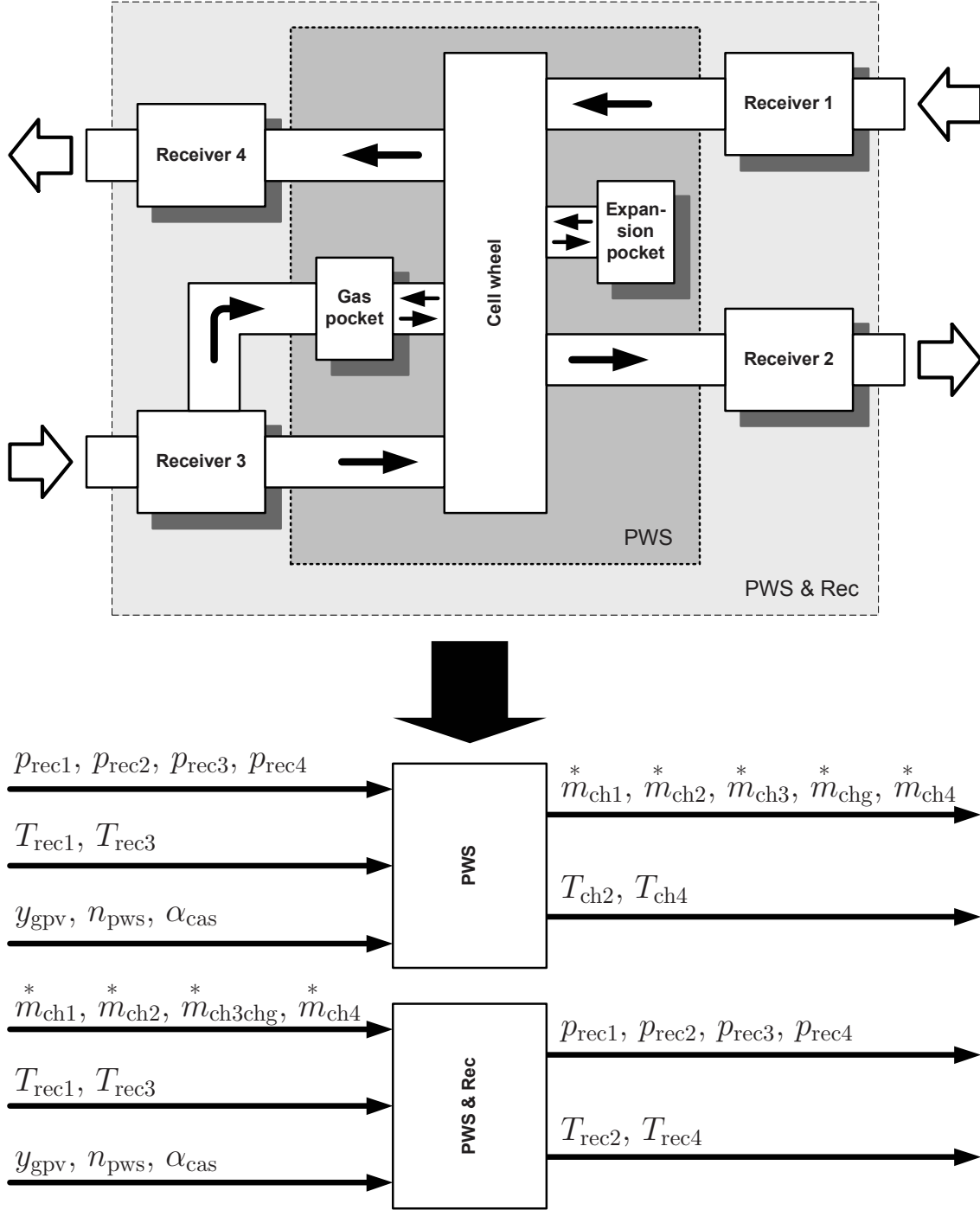


**Figure 3.13:** Definitions of inputs and outputs of the finite-difference model: Due to the high sensitivity of the mass flows versus pressure errors, the core **PWS** model is extended by four receivers ( $\rightarrow$  **PWS & Rec**). The channel mass flows, together with  $T_{rec1}$  and  $T_{rec3}$ , thus appear as inputs, whereas the receiver pressures and  $T_{rec2}$  and  $T_{rec4}$  are redefined as outputs.

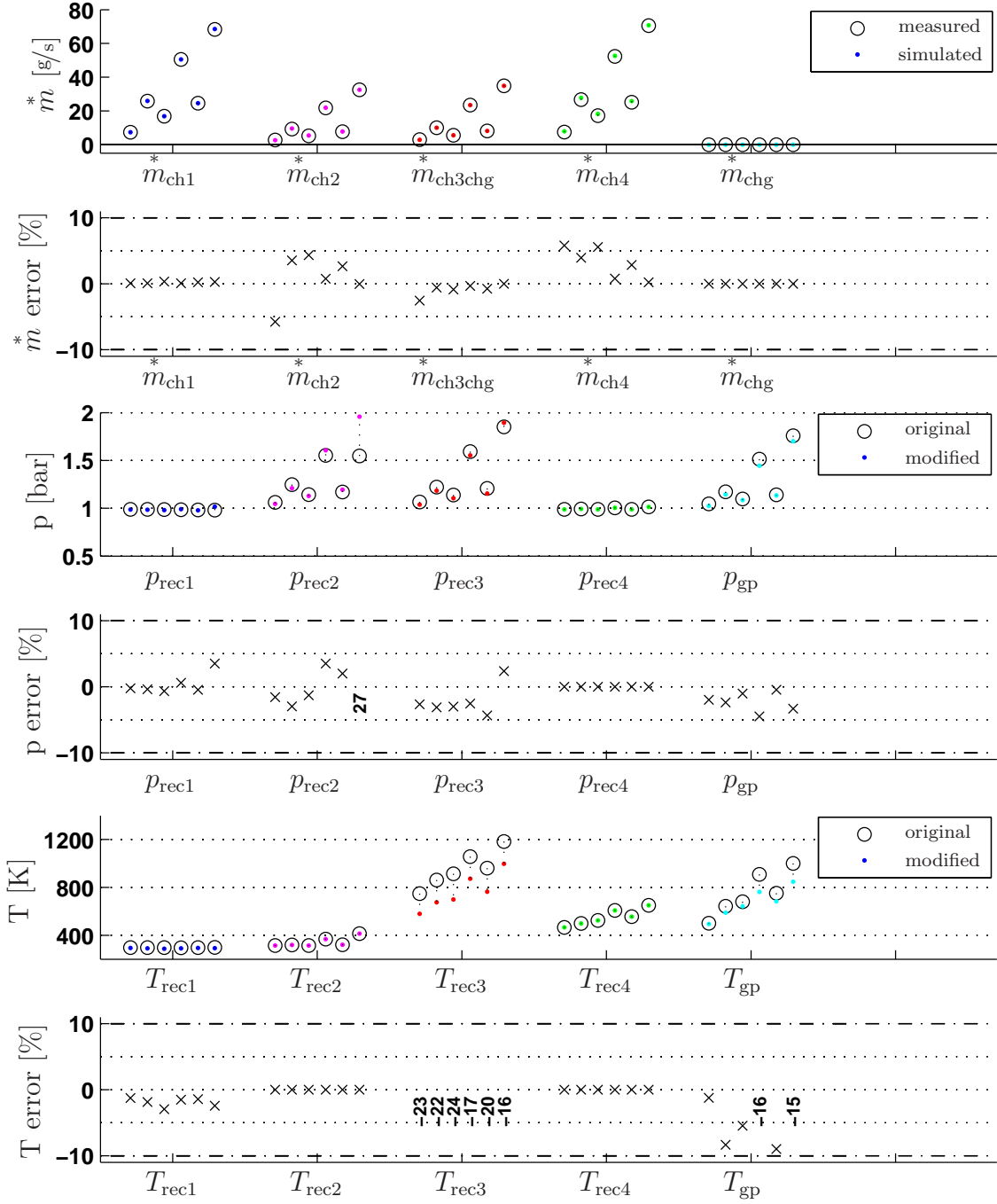


**Figure 3.14:** Model validation for the EA111/HX95 engine system with six independent steady-state operating points in the engine map. Mass flows are grouped by channel, whereas pressures and temperatures are grouped by receiver. For each group, the six points correspond to (1000 rpm/10 Nm), (1000 rpm/100 Nm), (2000 rpm/10 Nm), (2000 rpm/100 Nm), (3000 rpm/10 Nm), and (3000 rpm/100 Nm). Except for one point (attributed to sensor failure) in the series of  $p_{rec2}$  the model error amounts to less than 6%.



As another test, Figure 3.15 shows measurement and simulation results for four typical operating points in the engine map of the SAB360 engine with COMPRES<sup>®</sup>, a PWS of a different size and with a different channel geometry.

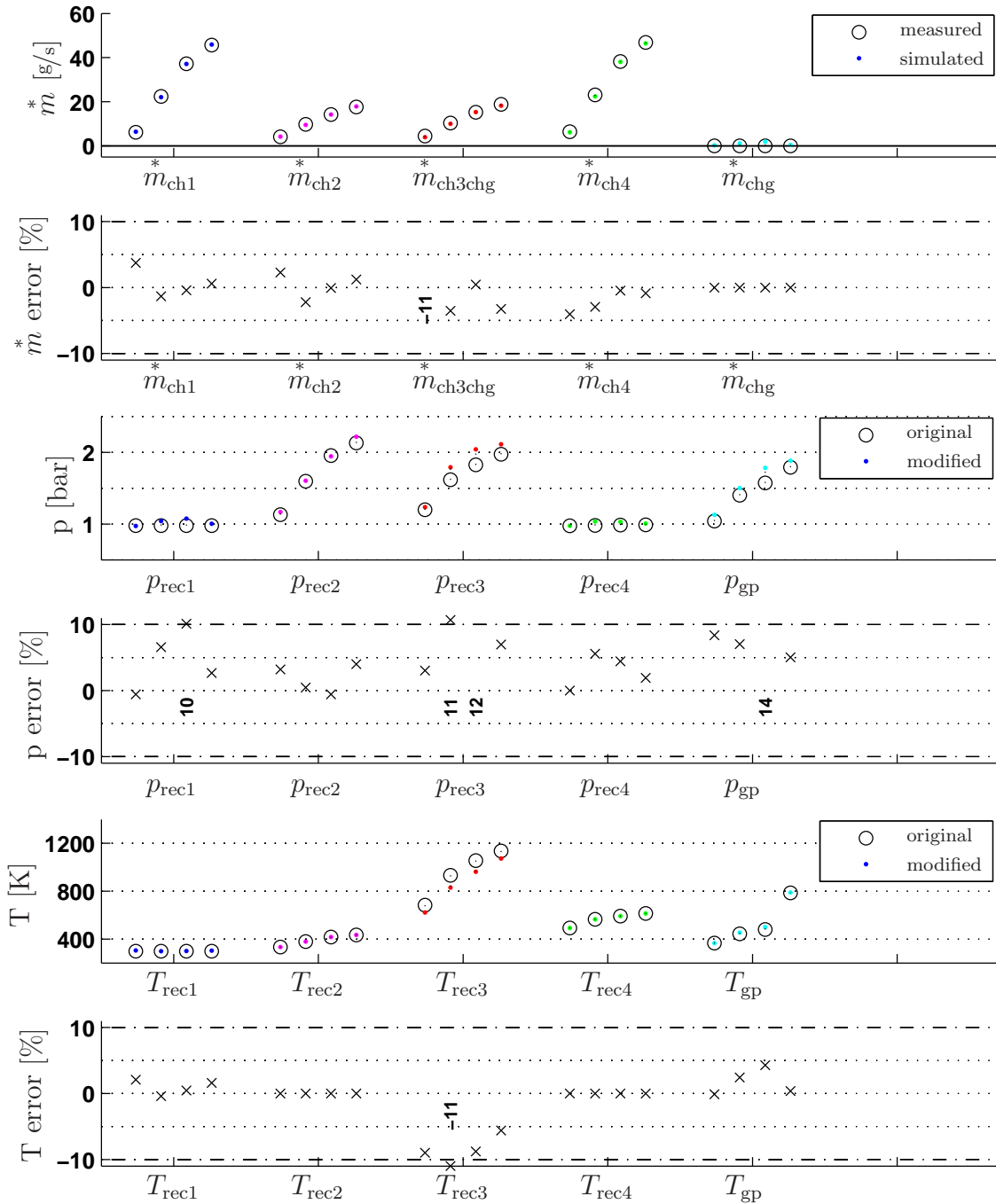


**Figure 3.15:** Model validation for SAB360/CX64 engine system. Four steady-state operating points in the engine map, grouped by channel and by receiver.

After the model parameters are adapted to the geometric data of the CX64, the model still reproduces the pressure and temperature measurements from mass flows very well and thus demonstrates its extrapolation capability.

## 3.2 Control-Oriented Mean-Value Model (MVMdl)

In the last section, a first-principle model was developed that is useful for interpolation and extrapolation from known, i.e. measured operating conditions. The computation time mainly depends on the resolution of the grid and on the number of PWS cycles that are repeated in order to avoid errors from initial conditions. For instance, the simulations presented in Fig. 3.14 were carried out by discretizing the rotor length into 25 pieces (and thus  $N_{\text{nodes}} = 26$ ). Repeating the simulation over ten cycles took 18 minutes on a personal computer <sup>2</sup>.

A PWS model that takes such long computation times in each intermediate step is not suitable to being used in a dynamical simulation in SIMULINK or to being transferred to a state-of-the-art electronic control unit (ECU) for automotive applications. Hence, the primary challenge is the separation of the most important patterns from the minor influences and the reduction of the complexity and thus the computational burden (Guzzella and Onder, 2004). A mean-value model is more suitable to deal with that challenge. Assuming that the charger is operated under efficiency-optimal conditions, in this section a simplified, control-oriented mean-value model is systematically developed, using the results of the finite-difference model.

While subsystems such as the engine, throttle bodies, intercooler, and three-way catalytic converter are quite well known, control-oriented models of PWSs are sparsely available in the literature. In particular, there are no PWS models that are simple enough to serve as a basis for real-time applications. The model presented in Weber (2001) can indeed predict the EGR rate, but it is not suitable to handle out-of-tune conditions as they occur for variable casing offsets and charger speeds. The model was intended to serve as a means to observe specific events on the SAB360/CX64 engine testbench.

For the control-oriented PWS model presented in Pfiffner et al. (1997), a limited PWS operation is assumed as well. Since its main focus is on mass flow control, the model does not include EGR effects.

The model presented in this section is similar to those described by Weber (2001) and Pfiffner et al. (1997) in that it is also based

---

<sup>2</sup>Pentium 4, 2.4 GHz Processor

on the one-dimensional linear wave theory. It additionally includes a method for identifying the unknown model parameters using the finite-difference model (FDMdl).

### 3.2.1 Summary of Linear Wave Theory

As demonstrated in Section 3.1, the main processes taking place in a PWS include the propagation of shock and expansion waves in presence of moving contact surfaces and losses such as friction, heat transfer, and leakage. A cell of the cell wheel may reasonably be simplified as a narrow, adiabatic pipe since the ratio of the cell length to its diameter is typically greater than ten. Moreover, the laws of conservation for mass, momentum, and energy are linearized, and both exhaust gas and fresh air are considered as perfect gases. Respecting these assumptions, the gas dynamics in a PWS may be described by means of the linear wave theory (Sauer, 1960). A detailed derivation of the basic relations may be found in Appendix C. The extensive set of equations that are necessary to model the wave process of a PWS (Weber, 2001) may be summarized by a modular set of functions. Note that

- all fluid and wave velocities are defined to be  $> 0$  in the positive x-direction, i.e. to the right (air) side,
- fluid and wave velocities are considered with relation to a fixed coordinate system and therefore depend on the velocity of the “carrier” fluid (indexed by 0),
- pressure ratios become  $> 1$  for “shock” waves and  $< 1$  for “expansion” waves, and
- for shock waves the polytropic exponent  $n = n(p_i, \kappa)$  is a function of the pressure ratio  $\pi$  and the ratio of specific heats  $\kappa$  and it includes losses such as friction, heat transfer, and leakage (see Fig. 3.16).

Although expansion waves are not as distinct as shock waves, they can similarly be represented by lines in the space-time plane. Similarly to those in Appendix C, a set of equations can be derived for expansion

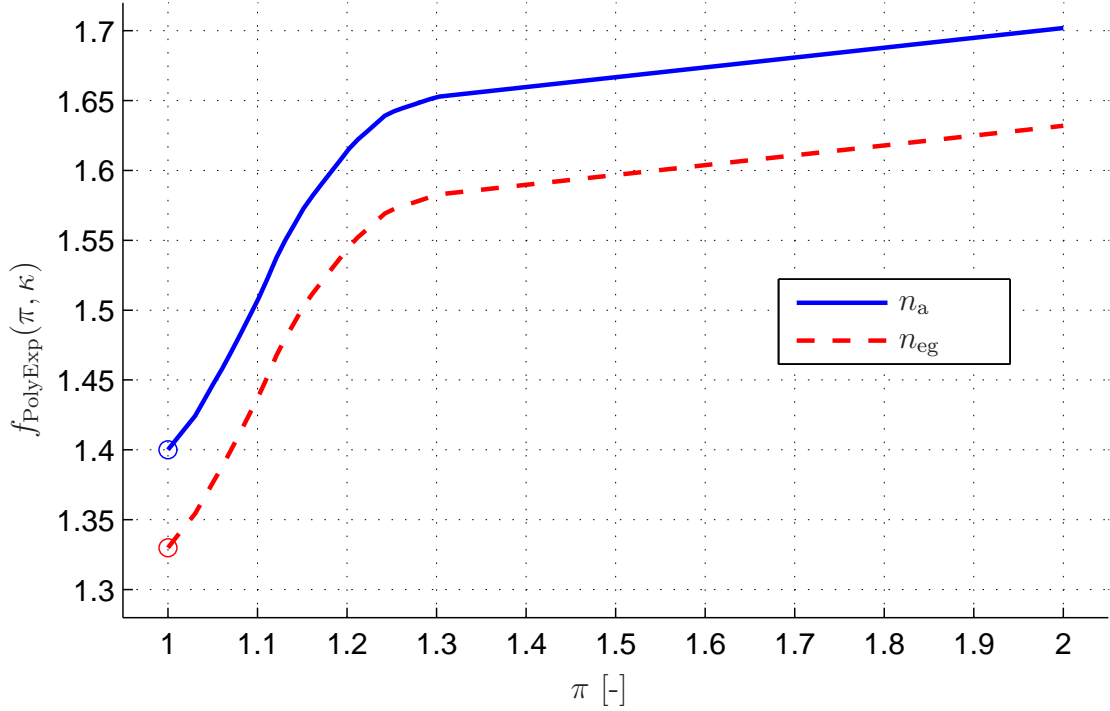


**Figure 3.16:** The function  $f_{\text{PolyExp}}(\pi, \kappa)$  defining polytropic exponents  $n$  for air and exhaust gas includes losses such as friction, heat transfer, and leakage. The curves were identified using the FDMdl.

waves although the pressure ratio then is lower than 1, the fluid is accelerated in the opposite direction, the temperature is decreased over the wave, and the polytropic coefficient  $n$  may be replaced by the ratio of specific heats  $\kappa$ .

The given quantities are the pressure  $p_{z0}$ , temperature  $T_{z0}$ , and fluid velocity  $u_{z0}$  of the carrier fluid (i.e. in the zone  $z_0$  in front of the wave  $w$ ), as well as the pressure  $p_{z1}$  of the fluid in the zone after the wave ( $z_1$ ). The pressure ratio  $\pi$ , wave velocity  $u_w$  and the states  $T_{z1}$  and  $u_{z1}$  of the fluid after the wave can then be calculated, allowing the distinction of the following four cases:

|   | Case                                    | Abbreviation |
|---|---|--------------|
| 1 | Shock wave moving towards the right     | SR           |
| 2 | Shock wave moving towards the left      | SL           |
| 3 | Expansion wave moving towards the right | ER           |
| 4 | Expansion wave moving towards the left  | EL           |

**Pressure ratios:**

$$\begin{aligned}
\pi_{\text{SR}} &= \frac{p_{z1}}{p_{z0}} > 1 \quad (\text{SR}) \\
\pi_{\text{SL}} &= \frac{p_{z1}}{p_{z0}} > 1 \quad (\text{SL}) \\
\pi_{\text{ER}} &= \frac{p_{z1}}{p_{z0}} < 1 \quad (\text{ER}) \\
\pi_{\text{EL}} &= \frac{p_{z1}}{p_{z0}} < 1 \quad (\text{EL})
\end{aligned} \tag{3.44}$$

**Polytropic exponents:**

$$\begin{aligned}
n_{\text{SR}} &= f_{\text{PolyExp}}(\pi_{\text{SR}}, \kappa_{\text{fluid}}) \quad (\text{SR}) \\
n_{\text{SL}} &= f_{\text{PolyExp}}(\pi_{\text{SL}}, \kappa_{\text{fluid}}) \quad (\text{SL}) \\
n_{\text{ER}} &= \kappa_{\text{fluid}} \quad (\text{ER}) \\
n_{\text{EL}} &= \kappa_{\text{fluid}} \quad (\text{EL})
\end{aligned} \tag{3.45}$$

**Wave velocities relative to fixed coordinates:**

$$\begin{aligned}
u_{\text{wSR}} &= u_{z0} + \sqrt{\frac{RT_{z0}}{2}} \sqrt{\pi_{\text{SR}} (n_{\text{SR}} + 1) + n_{\text{SR}} - 1} \quad (\text{SR}) \\
&=: f_{\text{WaveVel}}(u_{z0}, T_{z0}, p_{z0}, p_{z1}, \kappa, R, \rightarrow) \\
u_{\text{wSL}} &= u_{z0} - \sqrt{\frac{RT_{z0}}{2}} \sqrt{\pi_{\text{SL}} (n_{\text{SL}} + 1) + n_{\text{SL}} - 1} \quad (\text{SL}) \\
&=: f_{\text{WaveVel}}(u_{z0}, T_{z0}, p_{z0}, p_{z1}, \kappa, R, \leftarrow) \\
u_{\text{wER}} &= u_{z0} + \sqrt{\frac{RT_{z0}}{2}} \sqrt{(1/\pi_{\text{ER}}) (n_{\text{ER}} + 1) + n_{\text{ER}} - 1} \quad (\text{ER}) \\
&=: f_{\text{WaveVel}}(u_{z0}, T_{z0}, p_{z0}, p_{z1}, \kappa, R, \rightarrow) \\
u_{\text{wEL}} &= u_{z0} - \sqrt{\frac{RT_{z0}}{2}} \sqrt{(1/\pi_{\text{EL}}) (n_{\text{EL}} + 1) + n_{\text{EL}} - 1} \quad (\text{EL}) \\
&=: f_{\text{WaveVel}}(u_{z0}, T_{z0}, p_{z0}, p_{z1}, \kappa, R, \leftarrow)
\end{aligned} \tag{3.46}$$

**Fluid velocities relative to fixed coordinates:**

$$\begin{aligned}
u_{z1} &= u_{z0} + \sqrt{2 R T_{z0}} \frac{\pi_{\text{SR}} - 1}{\sqrt{\pi_{\text{SR}} (n_{\text{SR}} + 1) + n_{\text{SR}} - 1}} \quad (\text{SR}) \\
&=: f_{\text{FluidVel}}(u_{z0}, T_{z0}, p_{z0}, p_{z1}, \kappa, R, \rightarrow) \\
u_{z1} &= u_{z0} - \sqrt{2 R T_{z0}} \frac{\pi_{\text{SL}} - 1}{\sqrt{\pi_{\text{SL}} (n_{\text{SL}} + 1) + n_{\text{SL}} - 1}} \quad (\text{SL}) \\
&=: f_{\text{FluidVel}}(u_{z0}, T_{z0}, p_{z0}, p_{z1}, \kappa, R, \leftarrow) \\
u_{z1} &= u_{z0} - \sqrt{2 R T_{z0}} \frac{(1/\pi_{\text{ER}} - 1)}{\sqrt{(1/\pi_{\text{ER}}) (n_{\text{ER}} + 1) + n_{\text{ER}} - 1}} \quad (\text{ER}) \\
&=: f_{\text{FluidVel}}(u_{z0}, T_{z0}, p_{z0}, p_{z1}, \kappa, R, \rightarrow) \\
u_{z1} &= u_{z0} + \sqrt{2 R T_{z0}} \frac{(1/\pi_{\text{EL}} - 1)}{\sqrt{(1/\pi_{\text{EL}}) (n_{\text{EL}} + 1) + n_{\text{EL}} - 1}} \quad (\text{EL}) \\
&=: f_{\text{FluidVel}}(u_{z0}, T_{z0}, p_{z0}, p_{z1}, \kappa, R, \leftarrow)
\end{aligned} \tag{3.47}$$

**Temperature ratio over the shock front <sup>3</sup>:**

$$\begin{aligned}
T_{z1} &= T_{z0} \pi_{\text{SR}} \frac{\pi_{\text{SR}} (n_{\text{SR}} - 1) + n_{\text{SR}} + 1}{\pi_{\text{SR}} (n_{\text{SR}} + 1) + n_{\text{SR}} - 1} \quad (\text{SR}) \\
&=: f_{\text{Temp}}(T_{z0}, p_{z1}, p_{z1}, \kappa) \\
T_{z1} &= T_{z0} \pi_{\text{SL}} \frac{\pi_{\text{SL}} (n_{\text{SL}} - 1) + n_{\text{SL}} + 1}{\pi_{\text{SL}} (n_{\text{SL}} + 1) + n_{\text{SL}} - 1} \quad (\text{SL}) \\
&=: f_{\text{Temp}}(T_{z0}, p_{z1}, p_{z1}, \kappa) \\
T_{z1} &= T_{z0} \pi_{\text{ER}} \frac{\pi_{\text{ER}} (n_{\text{ER}} - 1) + n_{\text{ER}} + 1}{\pi_{\text{ER}} (n_{\text{ER}} + 1) + n_{\text{ER}} - 1} \quad (\text{ER}) \\
&=: f_{\text{Temp}}(T_{z0}, p_{z1}, p_{z1}, \kappa) \\
T_{z1} &= T_{z0} \pi_{\text{EL}} \frac{\pi_{\text{EL}} (n_{\text{EL}} - 1) + n_{\text{EL}} + 1}{\pi_{\text{EL}} (n_{\text{EL}} + 1) + n_{\text{EL}} - 1} \quad (\text{EL}) \\
&=: f_{\text{Temp}}(T_{z0}, p_{z1}, p_{z1}, \kappa)
\end{aligned} \tag{3.48}$$

Hence the four cases are condensed in the functions  $f_{\text{PolyExp}}$ ,  $f_{\text{WaveVel}}$ ,  $f_{\text{FluidVel}}$ , and  $f_{\text{Temp}}$ , specifying the states in zone  $z_0$ , the pressure in zone  $z_1$ , and the wave direction.

### 3.2.2 Modeling the High-Pressure Part

In contrast to the COMPREX<sup>®</sup> PWS that is described and modeled in Weber (2001), the HYPREX<sup>®</sup> PWS present the possibility to vary the casing offset within a certain range (see Fig. 1.2). Generally, varying cell-wheel speeds and casing offsets involve the necessity of a structural switching. For instance, the shock wave  $w_{3o1}$ , triggered by the pressure difference between Channel 3 and cell (see Fig. 3.17), is normally reflected as a second shock wave  $w_{3o2}$  on the air side. But if the casing offset is so low that the shock wave  $w_{3o1}$  runs into the open Channel 2, this builds a completely different base for the following waves. In fact,  $w_{3o2}$  then is formed as expansion wave for  $p_{rec3} > p_{rec2}$ . As demonstrated in Fig. 3.17 for the high-pressure part, the multitude of schematical wave diagrams may be reduced to six basic modes.

However, since the required MVMdl is not intended to work universally for all possible operating conditions, the modeling is restricted to *in-tuned conditions* in the “nominal” mode as shown in the wave diagram in Mode (a) of Fig. 3.17. In that case, shock wave  $w_{3o1}$  hits the air side shortly before Channel 2 opens, and the reflected shockwave  $w_{3o2}$  returns to the gas side soon after Channel 3 closes. In a way similar to that described in Weber (2001), for given pressure and temperature boundaries (i.e.  $p_{rec2}$ ,  $p_{rec3}$ ,  $p_{gp}$ ,  $T_{rec3}$ ), the wave diagram is built up step by step, i.e. zone by zone or wave by wave, for the high-pressure part. In contrast to Weber (2001), the fitting parameters are piecewise identified by comparing the lumped states of the mean-value model (MVMdl) with the pressure, temperature, and velocity distributions of the finite-difference model (FDMdl). Figure 3.18 presents both the FDMdl (underlayed) and the MVMdl results (overlayed) for a typical operating point. Figure 3.19 clearly shows the agreement between the models for the high-pressure mass flow outputs  $\dot{m}_{ch2}^*$ ,  $\dot{m}_{ch3}^*$ , and  $\dot{m}_{chg}^*$  over a wide range of operating points.

**Zone  $z_0$ :** The states  $p_0$ ,  $T_0$ , and  $u_0$  in the initial zone  $z_0$  are closely related to the states in Receiver 1.

$$\begin{aligned} p_{z0} &= p_{rec1} + \Delta p_{z0} \\ T_{z0} &= T_{rec1} + \Delta T_{z0} \\ u_{z0} &= 0 \end{aligned} \tag{3.49}$$



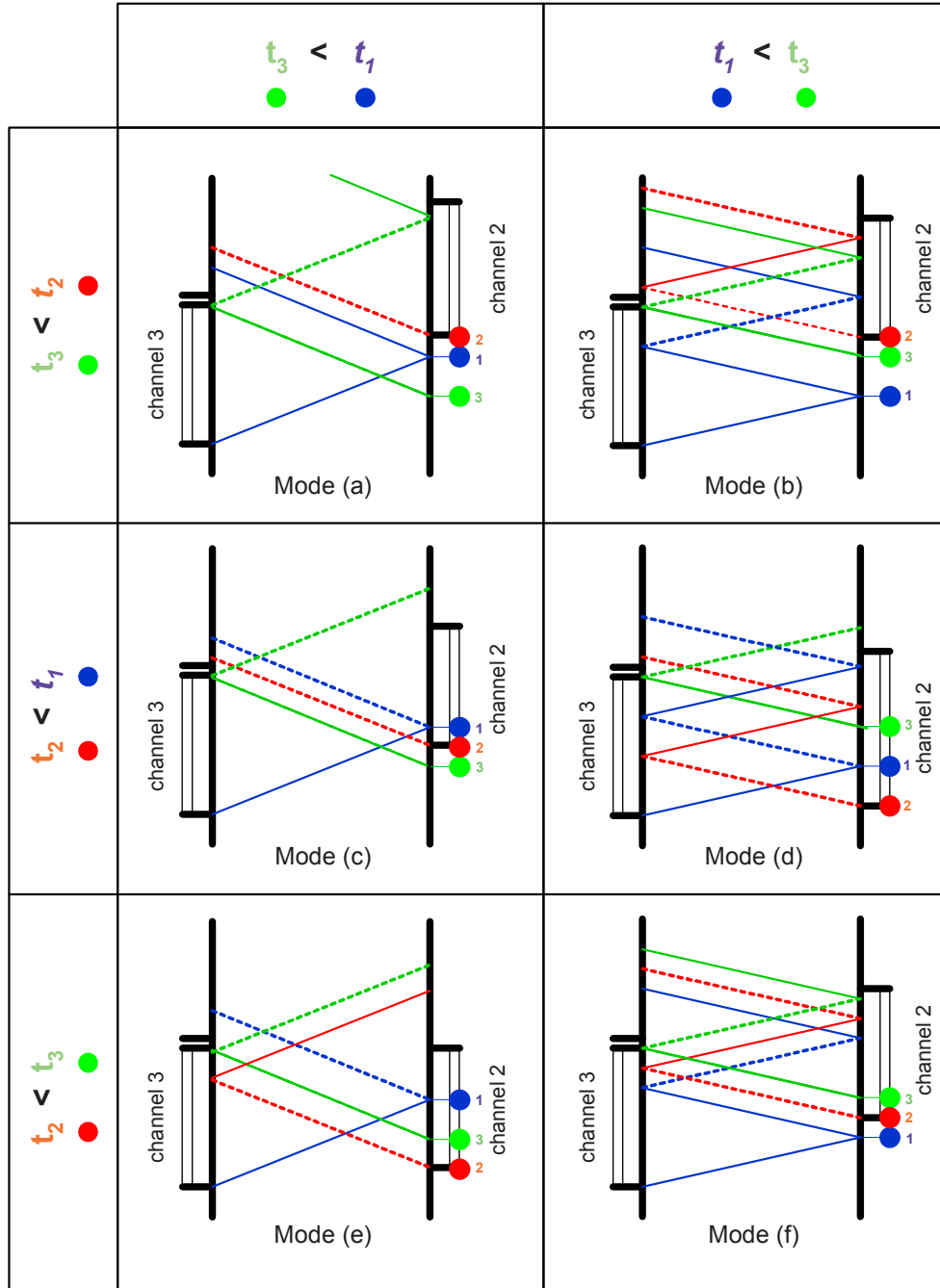


**Figure 3.17:** Six basic modes of wave diagrams caused by variations of cell-wheel speed  $n_{pws}$  and casing offset  $\alpha_{cas}$ . Defining  $t = 0$  at the edge when Channel 3 is opened,  $t_1$  is the time when the first wave (triggered by opening Channel 3) is reflected on the air side,  $t_2$  is the time when Channel 2 is opened, and  $t_3$  is the time at which a wave would have to start on the air side to exactly hit the point where Channel 3 is closed.

Modes a,c,e:  $n_{pws}$  too high ; Modes b,c,f:  $n_{pws}$  too low

Modes a,b: shock wave  $w_{3o1}$  is reflected as another shock wave

Modes c,d: shock wave  $w_{3o1}$  is running into the open Channel 2

Modes e,f: wave  $w_{3o2}$  is running into the open Channel 3

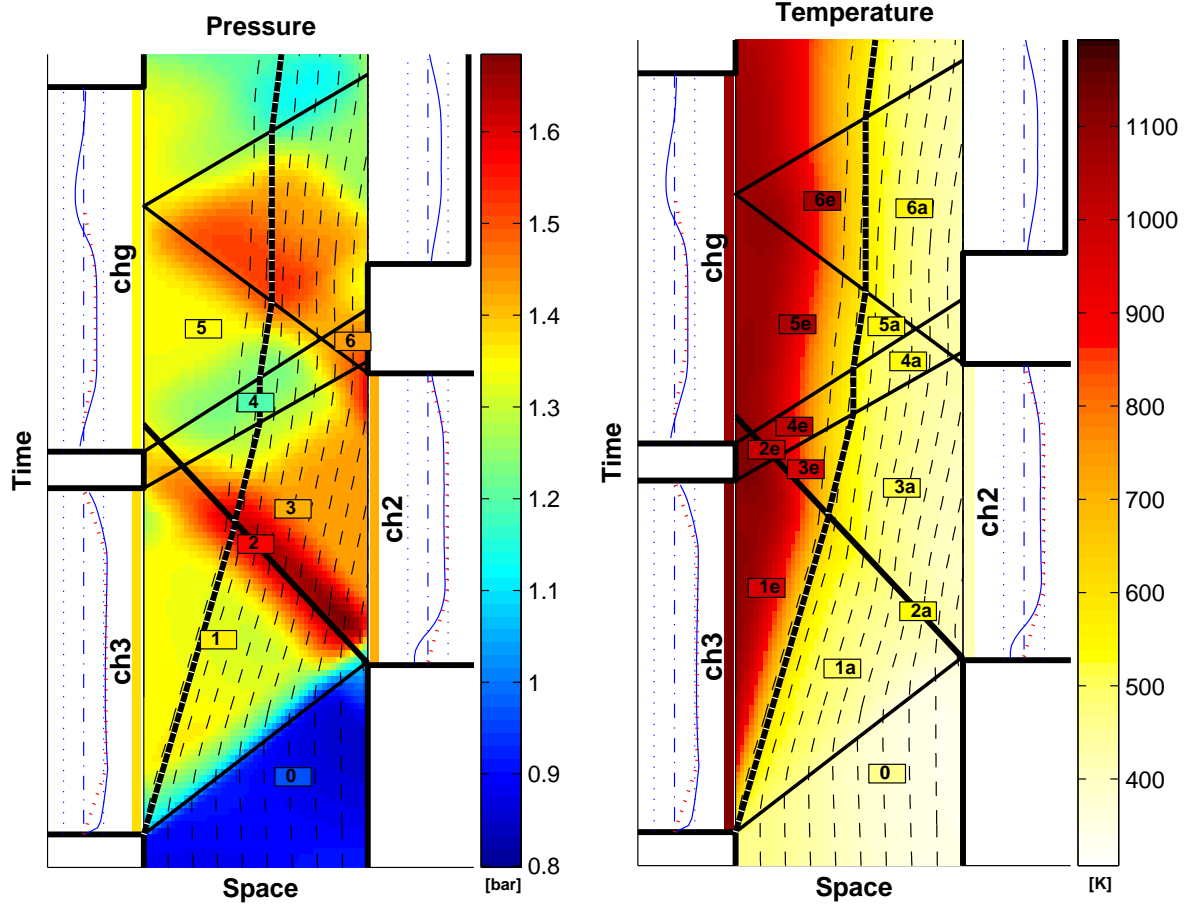


**Figure 3.18:** Mean-value-model parameter identification using the finite-difference model: Underlaid are the pressure and temperature distributions resulting from the finite-difference model (FDMdl). Overlaid in boxes are the results of the mean-value model (MVMdl). The solid lines refer to waves and the charger casing, the dashed line to the contact front. The zones are limited by waves and charger casing and, for temperatures, by the contact front. Using the same color map, the lumped values for pressure and temperature in each zone are displayed in the boxes. Pressures and temperatures are assumed to be constant within each zone.

**Wave  $w_{301}$ :** The pressure in zone  $z_1$  is equivalent to  $p_{\text{rec}3}$ . For the shock wave  $w_{301}$  (triggered by the pressure difference between Channel 3 and the cell and moving in the positive  $x$ -direction), pressure ratio  $\pi_{301}$  and shock velocity  $u_{w301}$  follow

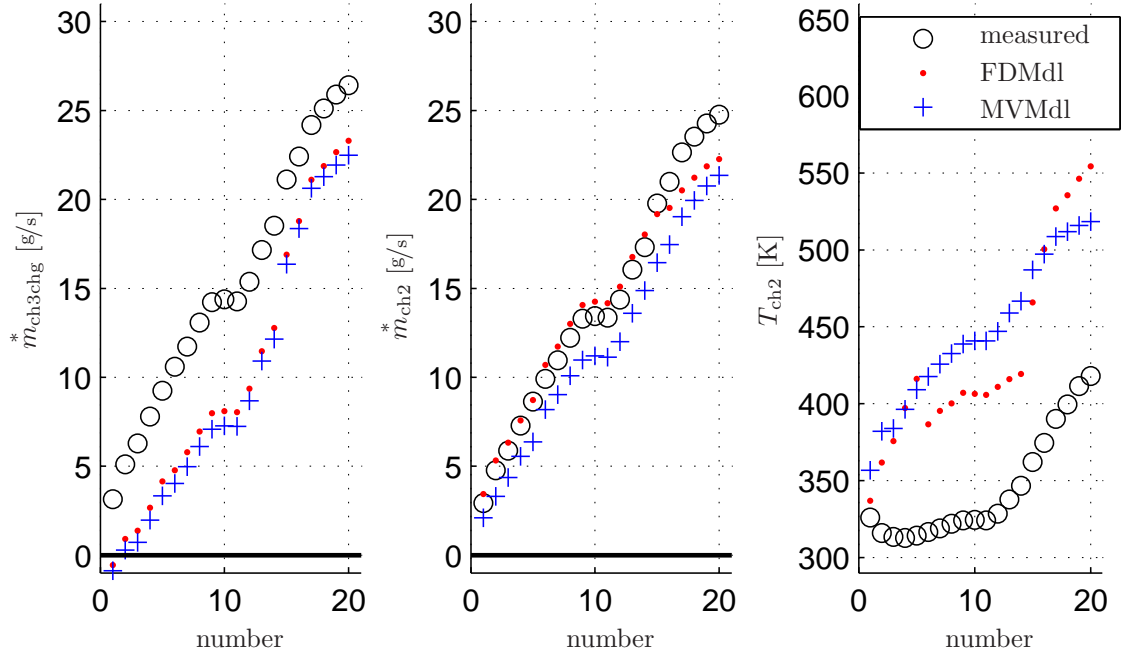


**Figure 3.19:** Validation of the MVMdl versus the FDMdl and measurement results: Comparison of the high-pressure mass flows  $\dot{m}_{\text{ch3chg}}^*$  and  $\dot{m}_{\text{ch2}}^*$  and the outflowing temperature  $T_{\text{ch2}}$  for 20 steady-state operating points along  $n_e = 1500 \text{ rpm}$ .

from Eq. (3.44-SR), Eq. (3.45-SR), and Eq. (3.46-SR).

$$\begin{aligned}
 p_{z1} &= p_{\text{rec3}} \\
 \pi_{3o1} &= \frac{p_{z1}}{p_{z0}} > 1 \\
 u_{w3o1} &= u_{z0} + \sqrt{\frac{RT_{z0}}{2}} \sqrt{\pi_{3o1} (n_{3o1} + 1) + n_{3o1} - 1}
 \end{aligned} \tag{3.50}$$

or, using the condensed notation:

$$u_{w3o1} = f_{\text{WaveVel}}(u_{z0}, T_{z0}, p_{z0}, p_{z1}, \kappa, R, \rightarrow)$$

**Zone  $z_1$ :** After Channel 3 opens, some exhaust gas enters the cell. Zone  $z_1$  then actually could be modeled as two zones (exhaust gas and air). However, due to the contact condition, one lumped parameter for pressure and velocity is sufficient. For the temperature, index  $a$  denotes air and  $e$  stands for exhaust gas. The mean value of both temperatures is the basis for the

calculation of the following wave and fluid velocities.

$$\begin{aligned}
 u_{z1} &= f_{\text{FluidVel}}(u_{z0}, T_{z0}, p_{z0}, p_{z1}, \kappa, R, \rightarrow) \\
 T_{z1a} &= f_{\text{Temp}}(T_{z0}, p_{z1}, p_{z1}, \kappa) \\
 T_{z1e} &= T_{\text{rec3}} \\
 T_{z1} &= \frac{T_{1a} + T_{1e}}{2}
 \end{aligned} \tag{3.51}$$

**Wave  $w_{3o2}$ :** The wall condition on the right-hand side theoretically stops the fluid. However, since the cell has a finite width and wave  $w_{3o1}$  is reflected close to the opening edge of Channel 2, the fluid is not stopped to zero but only decelerated to approximately half of its speed. This may be concluded from a visual comparison of the pressure and velocity distributions of the FDMdl with the results of the mean values of pressure and velocity of zone  $z_2$  of the mean-value model (Fig. 3.18). In the ideal case, the pressure  $p_{z2}$  in zone  $z_2$  after the reflection of shock wave  $w_{3o1}$  is equal to the total pressure in zone  $z_1$ . Due to leakage and heat transfer, this pressure is slightly lower. The pressure ratio  $\pi_{3o2}$  can be isolated from:

$$\begin{aligned}
 u_{z2} &\approx 0.5 u_{z1} \\
 u_{z2} &\stackrel{!}{=} u_{z1} + \sqrt{2 R T_{z1a}} \frac{\pi_{3o2} - 1}{\sqrt{\pi_{3o2} (n + 1) + n - 1}}
 \end{aligned} \tag{3.52}$$

Hence, a quadratic equation in  $\pi_{3o2}$  follows for the theoretical pressure ratio over wave  $w_{3o2}$ :

$$\begin{aligned}
 \pi_{3o2, \text{theo}} &= \frac{-b + \sqrt{b^2 - 4ac}}{2a} > 1 \\
 \text{with} \\
 a &= 2 R T_{z1a} \\
 b &= -4 R T_{z1a} - (u_{z1} - u_{z2})^2 (n + 1) \\
 c &= 2 R T_{z1a} - (u_{z1} - u_{z2})^2 (n - 1)
 \end{aligned} \tag{3.53}$$

Arranging a reflection efficiency (Weber, 2001) like

$$\eta_r = \frac{\pi_{3o2} - 1}{\pi_{3o2, \text{theo}} - 1} \approx 0.8 \tag{3.54}$$

includes losses like leakage and heat transfer. Pressure  $p_{z2}$  in zone  $z_2$  and shock velocity  $u_{w3o2}$  then follow as:

$$\begin{aligned} p_{z2} &= p_{z1} \pi_{3o2} \\ u_{w3o2} &= f_{\text{WaveVel}}(u_{z1}, T_{z1}, p_{z1}, p_{z2}, \kappa, R, \leftarrow) \end{aligned} \quad (3.55)$$

**Zone  $z_2$ :** Velocity and temperature again follow from pressure ratio over wave  $w_{3o2}$ .

$$\begin{aligned} u_{w3o2} &= f_{\text{WaveVel}}(u_{z1}, T_{z1}, p_{z1}, p_{z2}, \kappa, R, \leftarrow) \\ T_{z2a} &= f_{\text{Temp}}(T_{z1a}, p_{z1}, p_{z2}, \kappa) \\ T_{z2e} &= f_{\text{Temp}}(T_{z1e}, p_{z1}, p_{z2}, \kappa) \\ T_{z2} &= \frac{T_{z2a} + T_{z2e}}{2} \end{aligned} \quad (3.56)$$

**Wave  $w_{2o1}$ , zone  $z_3$ :** Another wave  $w_{2o1}$  (expansion wave) is triggered (to the left) when the cell passes the opening edge of Channel 2. Since  $p_{z3} < p_{z2}$ , the fluid is accelerated towards the right (positive  $x$ -direction) and the temperatures are lowered over the wave.

$$\begin{aligned} p_{z3} &= p_{\text{rec2}} \\ u_{w2o1} &= f_{\text{WaveVel}}(u_{z2}, T_{z2}, p_{z2}, p_{z3}, \kappa, R, \leftarrow) \\ u_{z3} &= f_{\text{FluidVel}}(u_{z2}, T_{z2}, p_{z2}, p_{z3}, \kappa, R, \leftarrow) \\ T_{z3a} &= f_{\text{Temp}}(T_{z2a}, p_{z2}, p_{z3}, \kappa) \\ T_{z3e} &= f_{\text{Temp}}(T_{z2e}, p_{z2}, p_{z3}, \kappa) \\ T_{z3} &= \frac{T_{z3a} + T_{z3e}}{2} \end{aligned} \quad (3.57)$$

**Wave  $w_{3c1}$ , zone  $z_4$ :** Based on the fact that  $u_{z4} \approx 0.25 u_{z3}$  (again, concluded by comparing the FDMdl results with the MVMdl results as depicted in Fig. 3.18), the pressure ratio  $\pi_{3c1}$  can be calculated by repeating the sequence of Eq. (3.53). Pressure  $p_{z4}$  then follows from  $p_{z4} = p_{z3} \pi_{3c1}$ , and wave velocity, fluid velocity

and temperatures follow from:

$$\begin{aligned}
u_{w3c1} &= f_{\text{WaveVel}}(u_{z3}, T_{z3}, p_{z3}, p_{z4}, \kappa, R, \rightarrow) \\
u_{z4} &= f_{\text{FluidVel}}(u_{z3}, T_{z3}, p_{z3}, p_{z4}, \kappa, R, \rightarrow) \\
T_{z4a} &= f_{\text{Temp}}(T_{z3a}, p_{z3}, p_{z4}, \kappa) \\
T_{z4e} &= f_{\text{Temp}}(T_{z3e}, p_{z3}, p_{z4}, \kappa) \\
T_{z4} &= \frac{T_{z4a} + T_{z4e}}{2}
\end{aligned} \tag{3.58}$$

**Wave  $w_{go1}$ , zone  $z_5$ :** When the cell passes the opening edge of the gas pocket channel, a process similar to that described for Channel 3 is triggered.

$$\begin{aligned}
u_{wgo1} &= f_{\text{WaveVel}}(u_{z4}, T_{z4}, p_{z4}, p_{z5}, \kappa, R, \rightarrow) \\
u_{z5} &= f_{\text{FluidVel}}(u_{z4}, T_{z4}, p_{z4}, p_{z5}, \kappa, R, \rightarrow) \\
T_{z5a} &= f_{\text{Temp}}(T_{z4a}, p_{z4}, p_{z5}, \kappa) \\
T_{z5e} &= T_{gp} \\
T_{z5} &= \frac{T_{z5a} + T_{z5e}}{2}
\end{aligned} \tag{3.59}$$

**Wave  $w_{2c1}$ , zone  $z_6$ :** The last essential wave to compute the high pressure mass flows consists of  $w_{2c1}$ , i.e. the wave that is formed due to the deceleration of the outflowing fluid when Channel 2 closes. The procedure of  $w_{3c1}$  is repeated.

$$\begin{aligned}
u_{z6} &\approx 0.2 u_{z5} \\
u_{w2c1} &= f_{\text{WaveVel}}(u_{z6}, T_{z6}, p_{z6}, p_{z4}, \kappa, R, \leftarrow) \\
T_{z6a} &= f_{\text{Temp}}(T_{z5a}, p_{z5}, p_{z4}, \kappa) \\
T_{z6e} &= f_{\text{Temp}}(T_{z5e}, p_{z5}, p_{z4}, \kappa)
\end{aligned} \tag{3.60}$$

As depicted in Fig. 3.18, all essential wave and zone states may be plotted into the x-t plane. The casing geometry, i.e. the times when channels open or close, may also be added respecting both cell-wheel speed  $n_{pws}$  and casing offset  $\alpha_{cas}$ . The fluid velocity profiles in the channel cross-sections are subject to casing geometry, wave timing, and cell width. The gradual opening of the cell also causes a gradual fluid acceleration. This effect is modeled by setting up a trapezoidal

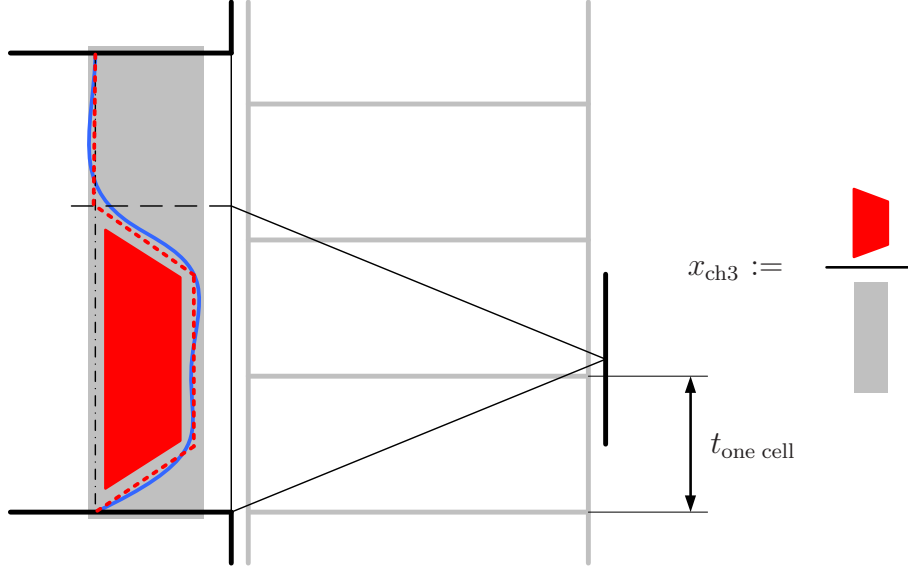


**Figure 3.20:** Gradual fluid acceleration due to gradual opening of the cell when passing Channel 3. The blue, solid line refers to the velocity in Channel 3, obtained with the FDMdl. The red dashed line represents the channel velocity for the mean-value model (MVMdl).

The fraction  $x_{\text{ch3}}$  indicates the “active” channel cross-section.

function for the fluid profile (Fig. 3.20). The ramp time is set to half of the time shift for one cell ( $t_{\text{one cell}}$ ).

The mass flow through Channel 3 can be calculated from density, velocity, full channel cross-section, and the parameter  $x_{\text{ch3}}$ , describing the ratio between active and full channel cross-section (see Fig. 3.20):

$$\begin{aligned} \dot{m}_{\text{ch3}}^* &= \frac{p_{\text{rec3}}}{R T_{\text{rec3}}} u_{z1} A_{\text{ch3}} x_{\text{ch3}} \\ \text{where} \\ x_{\text{ch3}} &= f(\text{casing geometry, wave timing}) \end{aligned} \tag{3.61}$$

Similarly,  $\dot{m}_{\text{ch2}}^*$  and  $\dot{m}_{\text{chg}}^*$  can be calculated.

$$\begin{aligned} \dot{m}_{\text{ch2}}^* &= \frac{p_{z3}}{R T_{z3}} u_{z3} A_{\text{ch2}} x_{\text{ch2}} \\ \dot{m}_{\text{chg}}^* &= \frac{p_{\text{gp}}}{R T_{\text{gp}}} u_{z5} A_{\text{chg}} x_{\text{chg}} \end{aligned} \tag{3.62}$$

### 3.2.3 Modeling EGR Effects

Recirculated exhaust gas through Channel 2 is closely connected to the scavenging process in the low-pressure part (Amstutz, 1991). Generally, the discontinuity surface between the hot exhaust gases and the cold fresh air within a cell is neither distinct nor well defined. Due to the finite cell width, the inflow process at the cell-port connection is gradual and the contact surface can be of a very complicated three-dimensional shape (Piechna and Lisewski, 1998). In the contact area there exists a mixture of exhaust gases and air. The distribution of the exhaust gases smoothly changes from 0 to 100%. Under normal operating conditions, the scavenging process is effective enough to not only remove exhaust gases from the cell, but also to lead a certain amount of compressed **fresh air** from the cell wheel through Channel 4. Under certain circumstances, the scavenging process is not fully efficient, such that a portion of the exhaust gases is not removed from the cell. That portion may then “wind up” and spread out in the direction of Channel 2. This wind-up process of the remaining gases only takes a few rotations of the cell wheel and causes exhaust gases to arrive at Channel 2 after a very short time (on the order of 10 to 15 rotations or 50 ms). Figure 3.21 exemplifies such a wind-up process. During each cycle, even under EGR conditions, some fresh air enters the cell during the passing of Channel 1, causing the dispersing exhaust gases to be suppressed towards the left (gas side). During this time, a natural “cleaning” process occurs. But in the end, a certain portion of the diluted exhaust gas may be delivered to Channel 2, together with the compressed air.

The analysis of steady-state measurement data leads to the useful relation between scavenging rate and EGR rate (Amstutz, 1991). The EGR rate  $x_{\text{egr}}$  is defined as the mass-specific EGR flow related to the engine air mass flow as follows:

$$x_{\text{egr}} := \frac{m_{\text{egr}}^*}{m_{\text{ch2}}^*} \quad (3.63)$$

The scavenging rate  $x_{\text{sc}}$  is an indicator for the amount of compressed fresh air that did not leave the cell wheel through Channel 2, but left



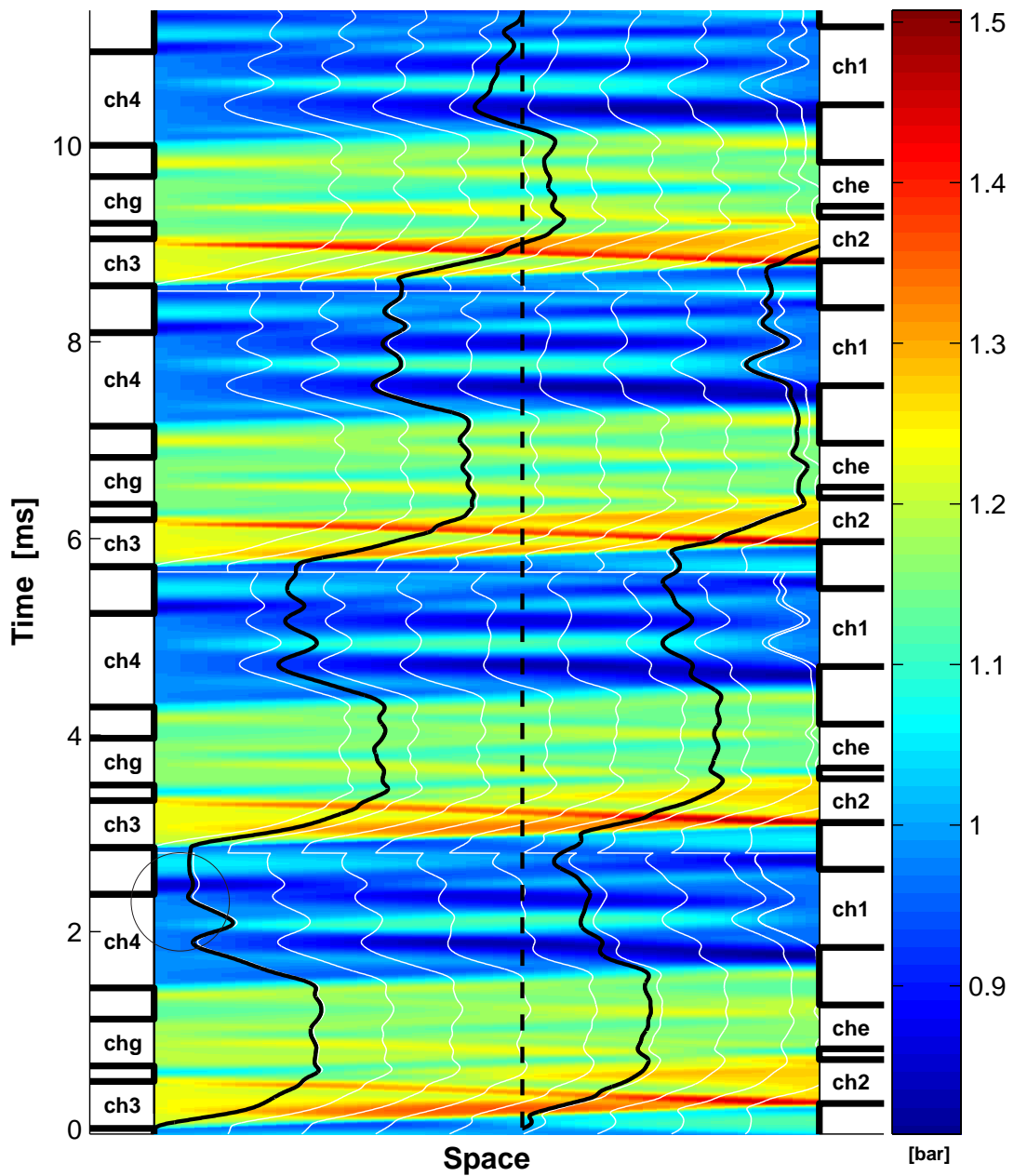


**Figure 3.21:** Graphical presentation of the formation of EGR, tracing an exhaust gas particle entering when Channel 3 opens. The particle does not leave through Channel 4 (indicated by the circle) and thus reappears in the next cycle. Assuming that the boundary pressures and temperatures remain constant over 2-4 cycles ( $\approx 20$  ms), in this simulation the particle steadily travels to the right-hand side until it finally leaves through Channel 2.

This winding-up process is responsible for even small exhaust gas fractions being transported fast towards Channel 2 (Amstutz, 1991).

through Channel 4 instead. It is defined as follows:

$$x_{sc} := \frac{\dot{m}_{14}^*}{\dot{m}_{ch2}^*} \quad (3.64)$$

Figure 3.22 demonstrates the relation between scavenging rate and EGR rate for multiple steady-state experiments on the EA111/HX95 engine system.

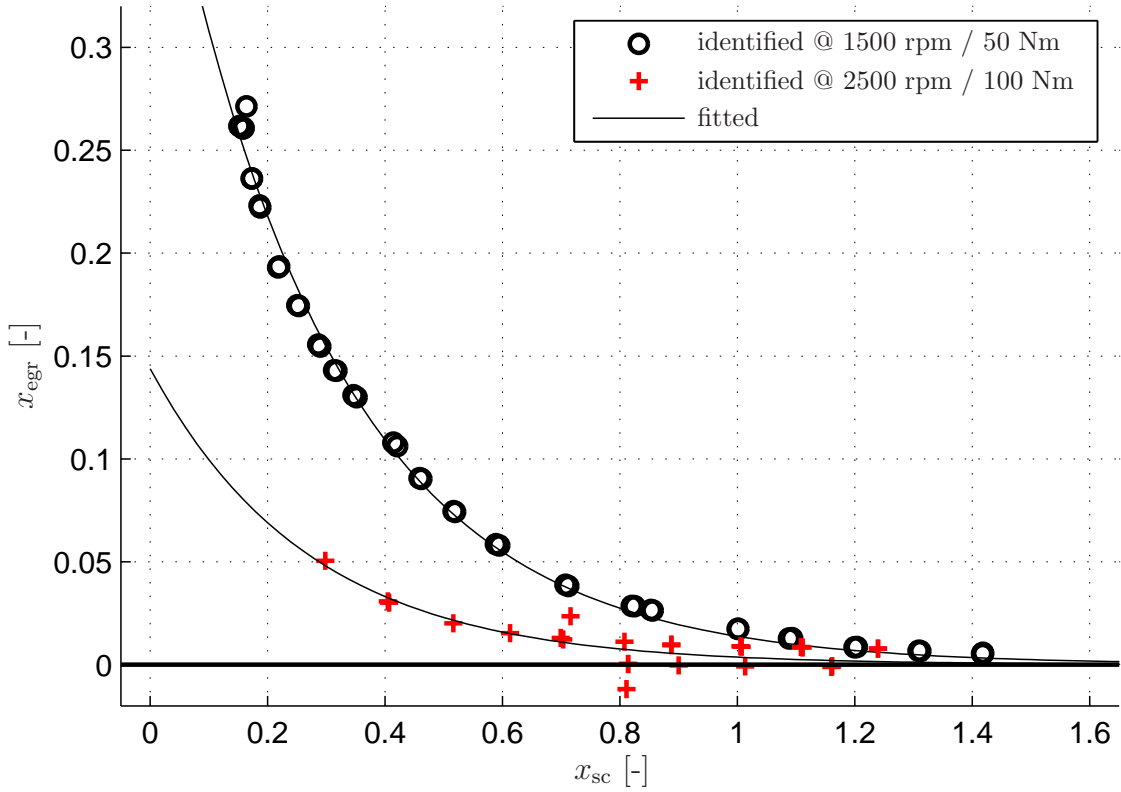


**Figure 3.22:** Identified relation between EGR rate and scavenging rate ( $x_{sc}$ ): At low scavenging rates, the sensitivity of the EGR rate increases rapidly.

The model described in this section is intended to serve as a basis for the control strategy that is going to be developed in Chapter 5, where  $x_{egr}$  will be substituted by  $x_{sc}$  as the control variable. Therefore, modeling is focused on the scavenging rate only. As Eq. (3.64) shows,  $x_{sc}$  may be derived from the mass flows through Channels 1 and 2. Hence, a precise and simple model for calculating  $\dot{m}_{ch1}^*$  would be quite useful. Mass flow  $\dot{m}_{ch1}^*$  is not only a function of the low-pressure intake density, i.e. of the states  $p_{rec1}$  and  $T_{rec1}$ , but it also depends on

the velocity of the inflowing mass through Channel 1  $u_{ch1}$ . The fluid in the cell is initially accelerated due to the expansion wave  $w_{4o1}$  (see Fig. 3.23) caused by the pressure ratio  $p_{sc}/p_4$ . The so-called *scavenging pressure*  $p_{sc}$  designates the pressure level of the fluid in the cell shortly before Channel 4 opens (Weber, 2001).

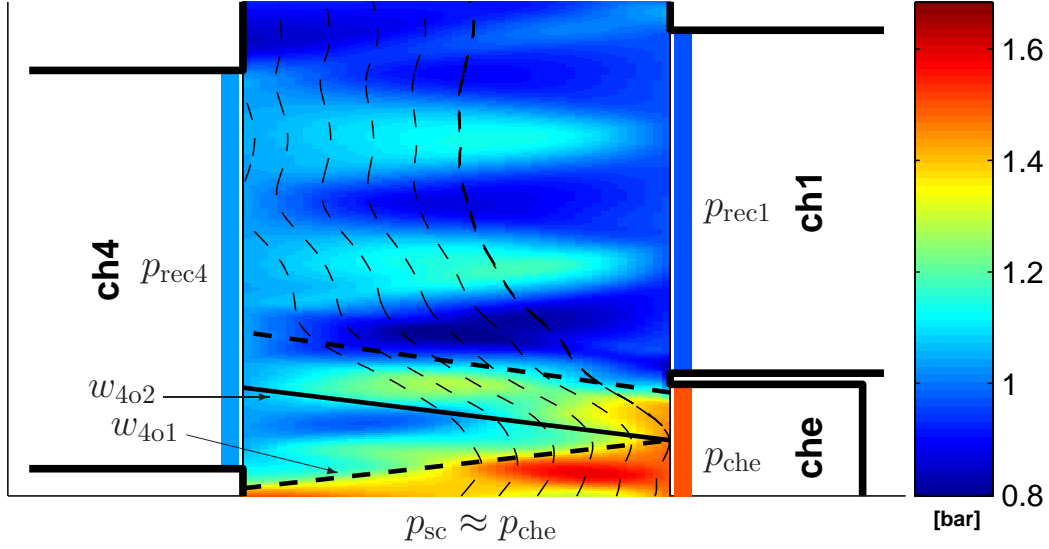


**Figure 3.23:** Scavenging process in the low-pressure part: Fluid acceleration mainly is due to  $p_{sc}$  (i.e. the pressure before the scavenging process starts) and pressure  $p_{che}$  in the expansion pocket. The two pressure ratios  $p_{sc}/p_{rec4}$  and  $p_{che}/p_{rec4}$  cause the waves  $w_{4o1}$  and  $w_{4o2}$ , respectively.

As soon as the wave  $w_{4o1}$  has reached the right (air) side, the reflected wave  $w_{4o2}$  generates an additional acceleration towards the left (gas side) since the pressure in the expansion pocket  $p_{che} \approx p_{sc}$  is higher than  $p_{rec4}$ . This initial speed is vital for the entire scavenging process. Once the cell reaches Channel 1, the positive low-pressure difference  $\Delta p_{14} := p_4 - p_1 \geq 0$  (Croes, 1979; Mayer et al., 1990) decelerates the fluid such that the particle path lines become curved as shown in Fig. 3.23. The prediction of  $\dot{m}_{ch1}^*$  therefore generally is a function of the low-pressure states  $p_{rec1}$ ,  $p_{rec4}$ , and  $T_{rec1}$ , but it is sensitive to  $p_{sc} \approx p_{che}$  and depends on the actuator signals  $n_{pws}$  and  $y_{gpv}$ .

- An increased low-pressure difference  $\Delta p_{14}$  reduces  $\dot{m}_{ch1}^*$  due to the more curved shape of the particle path. Backflow into the cell is possible.

- A very low cell-wheel speed  $n_{\text{pws}}$  may result in a backflow towards the right when exhaust gas is flowing back into the cell.
- The gas pocket valve, regarded as a by-pass valve, can lead more or less mass towards either the charging or the scavenging process. In return, feeding the charging process with all the energy available from Receiver 3 in the case of a fully closed gas pocket valve may lower the cell's capability for thorough scavenging.
- Moreover, leakage effects such as heat transfer and mass leakage through the gaps between rotor and casing and may further lower  $p_{\text{sc}}$  and worsen the scavenging process.

For dynamical simulations,  $\dot{m}_{\text{ch1}}^*$  may be calculated in a post-processing procedure using the more precise FDMdl. Later, in the control strategy described in Chapter 5,  $\dot{m}_{\text{ch1}}^*$  will be defined as a (measured) input signal, using just an air mass flow meter.

## Chapter 4

# Closed-Loop Simulation and Validation

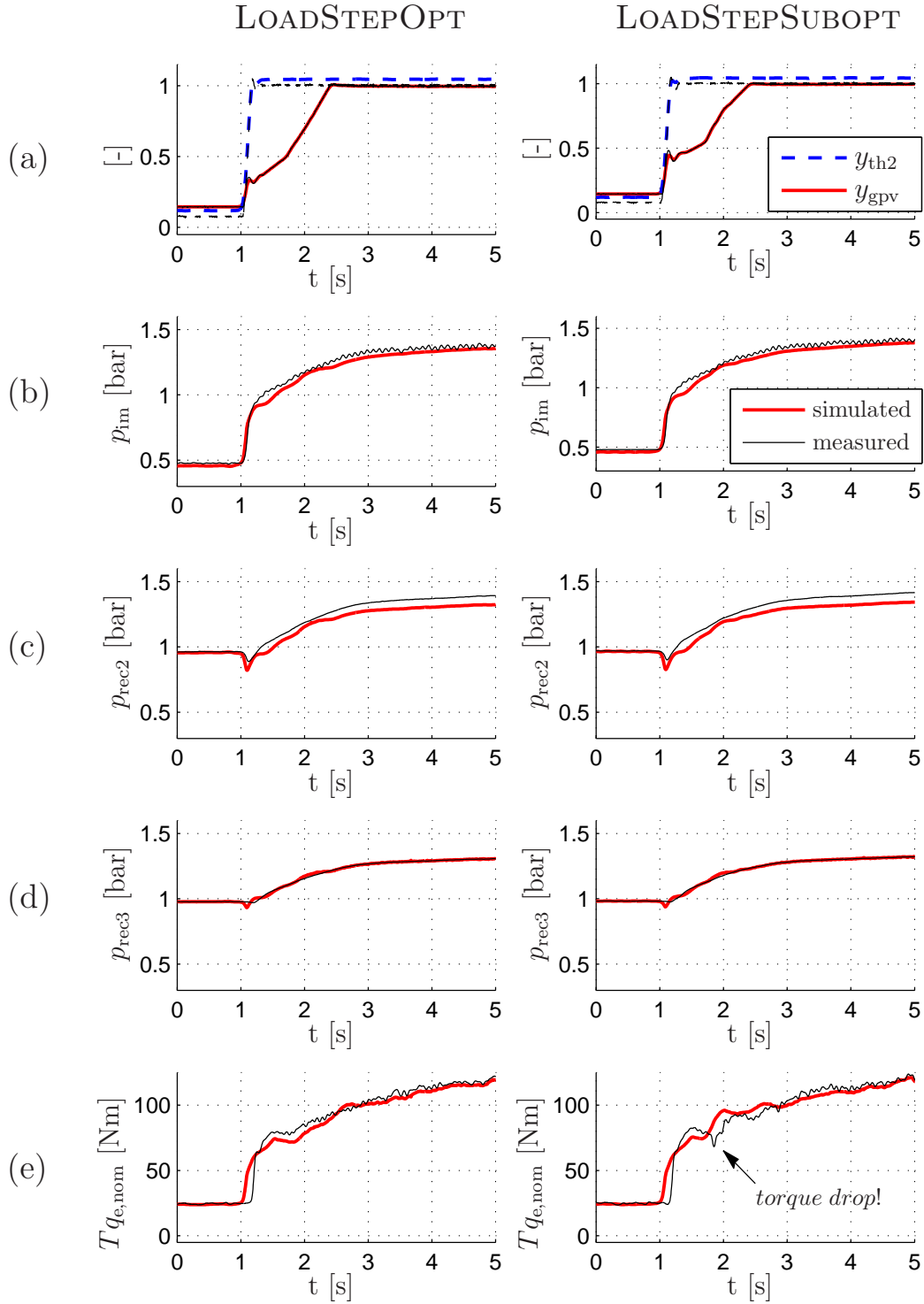
In order to simulate the high-pressure loop (HPL), that is the loop following the blocks PWS  $\rightarrow$  Receiver 2  $\rightarrow$  intercooler/Throttle 2  $\rightarrow$  intake manifold  $\rightarrow$  engine  $\rightarrow$  exhaust manifold  $\rightarrow$  TWC  $\rightarrow$  Receiver 3  $\rightarrow$  PWS, all models of the subsystems are implemented in MATLAB/SIMULINK<sup>1</sup> as proposed in Fig. 2.1.

Figure 4.1 contrasts measurement and simulation results for the load steps introduced in Fig. 1.8. Since the EGR model is not yet implemented, the engine torque is calculated with the assumption that no exhaust gas recirculation occurs.

Regarding EGR and scavenging rate, it is now possible to analyze the estimated mass flow rates. In Fig. 4.2, the measured mass flow rate  $\dot{m}_{ch1}^*$  is set in contrast with  $\dot{m}_{ch2}^*$ . In the case where EGR occurs, the difference  $\Delta \dot{m}_{14}^* = \dot{m}_{ch1}^* - \dot{m}_{ch2}^*$  and hence the scavenging rate  $x_{sc} = \dot{m}_{14}^* / \dot{m}_{ch2}^*$  temporarily becomes very small. This confirms the observation that low scavenging rates cause EGR, as illustrated in Fig. 3.22. An analysis of the estimated mass flow rates shows the various dynamics of the developing mass flows  $\dot{m}_{ch1}^*$  and  $\dot{m}_{ch2}^*$  (Fig. 4.2). Whereas  $\dot{m}_{ch2}^*$  is closely related to  $p_{im}$  and therefore immediately reacts to changes in the position of Throttle 2,  $\dot{m}_{ch1}^*$  is related to the pressure in Receiver 3 and to the gas pocket valve. Due to the pressure equalization occurring between Receiver 2 and the intake manifold, opening Throttle 2 immediately causes a high mass flow in the high-pressure loop and a high penetration ratio  $x_{pen}$  in the cell wheel. The

---

<sup>1</sup><http://www.mathworks.com/>



**Figure 4.1:** Validation of the PWS engine model for optimal and suboptimal load steps on the EA111/HX95 (see also Fig. 1.8). (a) Actuator input signals  $y_{th2}$  and  $y_{gpv}$ , (b,c,d) Pressure traces in the high-pressure loop, and (e) Engine torque build-up, assuming  $x_{egr} = 0$  for simulation.

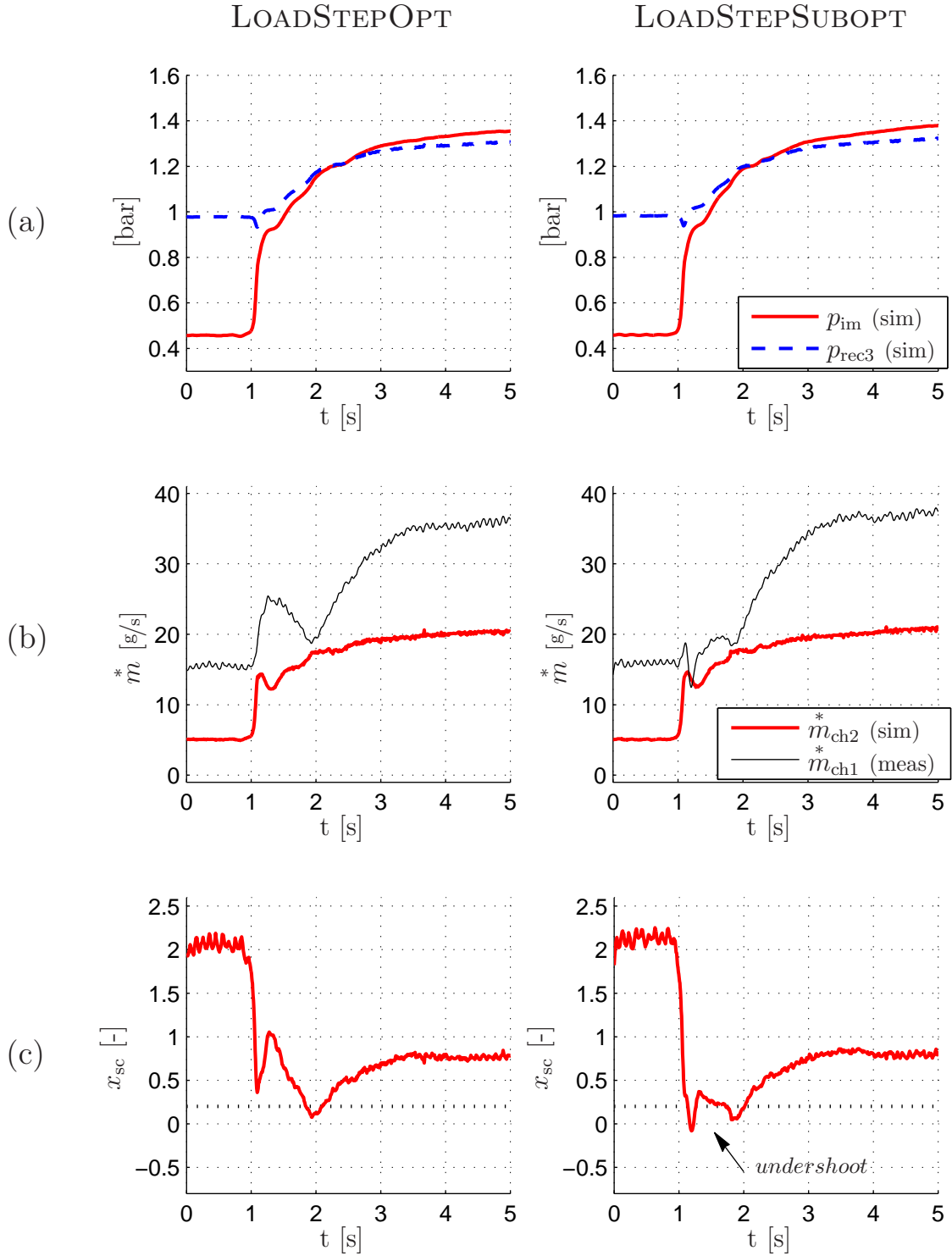


**Figure 4.2:** Traces of pressures, mass flows, and scavenging rates for two typical load steps on the EA111/HX95 (see also Fig. 1.8 and Fig. 4.1).

- (a) Pressure traces  $p_{im}$  and  $p_{rec3}$ , (b) Mass flows  $\dot{m}_{ch1}$  and  $\dot{m}_{ch2}$ , and  
(c) Scavenging rates

value

$$x_{\text{pen}} = \frac{L_{\text{pen}}}{L_{\text{rot}}} \quad (4.1)$$

indicates the maximum value of the penetration length  $L_{\text{pen}}$ , i.e., the distance by which the air is displaced in the cell compared to the rotor length  $L_{\text{rot}}$ . Assuming that the contact front between exhaust gas and air is well defined, a simple mass balance (Weber, 2001) leads to the function for  $L_{\text{pen}}$  (see also Fig. 4.3).

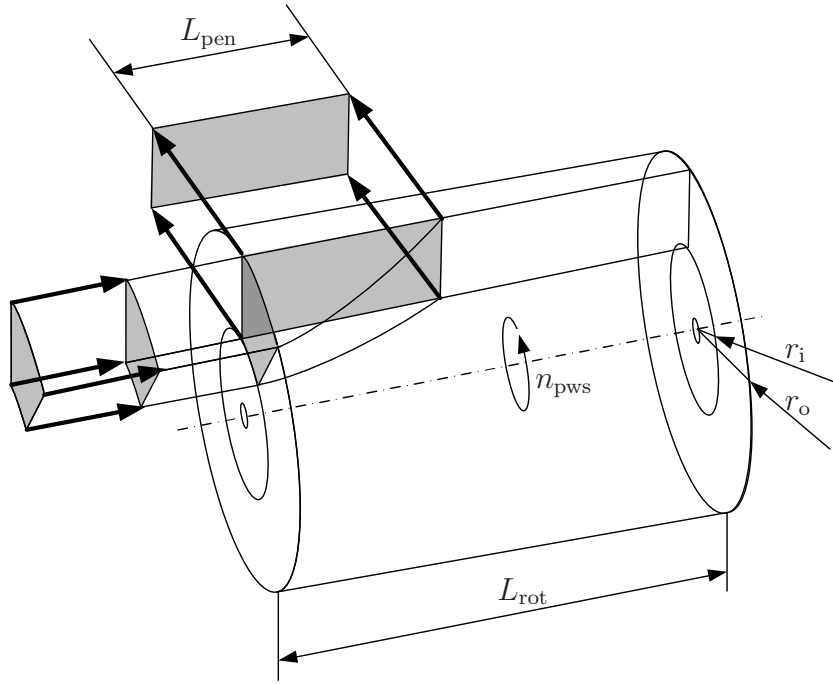


**Figure 4.3:** Exhaust gas penetration length in the rotor: a function of mass flow, density, cell-wheel speed, and channel geometry

$$m_{\text{ch3chg}}^* = L_{\text{pen}} \rho_{\text{sc}} \frac{n_{\text{pws}}}{60} \pi (r_o^2 - r_i^2) \quad (4.2)$$

The density may be roughly approximated by

$$\rho_{\text{sc}} = \frac{p_{\text{sc}}}{R T_{\text{sc}}} \approx \frac{p_{\text{gp}}}{R \frac{T_{\text{gp}} + T_{\text{rec2}}}{2}}$$

Once  $p_{\text{im}}$  has reached the ambient pressure level, all pressures in the high-pressure loop (HPL) increase more slowly. The pressure build-ups are dominated by the increasing engine outlet temperature. Due to



heat transfer, the energy increase of the fluids in the high-pressure loop in general and of the gas in Receiver 3 in particular is slow ( $\tau \approx 1$  s) compared to the initial jump of  $p_{\text{im}}$  ( $\tau \approx 0.1$  s).

High penetration ratios  $x_{\text{pen}}$  are not problematic with regard to EGR as long as there is sufficient scavenging energy available. As long as the initial acceleration of the fluid in the low-pressure part (caused by  $p_{\text{sc}}$  and  $p_{\text{che}}$ ) is high enough, the exhaust gases will be fully removed from the cell. But since the dynamics of  $\dot{m}_{\text{ch3chg}}^*$  (affecting  $x_{\text{pen}}$ ) and  $\dot{m}_{\text{ch1}}^*$  (as an indicator for the scavenging energy or  $p_{\text{sc}}$ ) are different, scavenging temporarily may become critical. Figure 4.4 displays the four phases occurring at the PWS outlet (Channel 4) during a load step.

**Part-load phase:** Although the pressure ratio  $p_{\text{sc}}/p_{\text{rec4}}$  is close to one and therefore the initial acceleration is low, complete scavenging and hence a high scavenging rate  $x_{\text{sc}}$  may still be expected.

**Critical phase:** The sudden increase of  $\dot{m}_{\text{ch3chg}}^*$  (due to  $p_{\text{im}}$ ) and therefore of  $L_{\text{pen}}$  and  $x_{\text{pen}}$  are not in proportion to the low initial acceleration due to being  $p_{\text{sc}}$  being low. It is possible that not all the exhaust gases leave through Channel 4 and that, therefore, some exhaust gases reappear in the next cycle. Exhaust gas windup (Fig. 3.21) and finally EGR may be caused. The scavenging rate reaches its minimum. This effect gets even worse if the gas pocket valve is closed.

**Recovery phase:** The pressure levels  $p_{\text{rec3}}$  and  $p_{\text{sc}}$  start to increase since the mass and energy losses (heat transfer) become small relative to the mass and the energy flows, respectively. Although  $\dot{m}_{\text{ch3chg}}^*$  and  $x_{\text{pen}}$  are further increasing, the initial acceleration is sufficient for complete scavenging. The scavenging rate  $x_{\text{sc}}$  is recovering from its minimum.

**Full-load phase:** The high pressure ratio  $p_{\text{sc}}/p_{\text{rec4}}$  is sufficient to completely remove the exhaust gases from the cell. However, the scavenging rate  $x_{\text{sc}}$  does not reach its part-load value again.

The typical shape of  $x_{\text{sc}}$  during the load step – an initial break-in followed by a retarded reversion – may be well described by the step

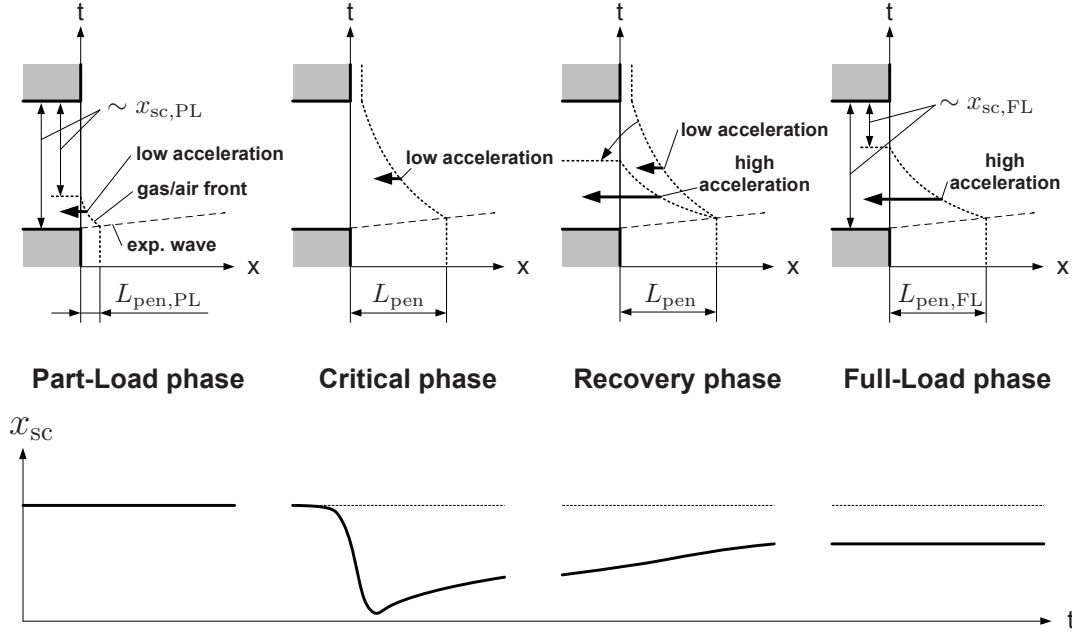


**Figure 4.4:** Four phases of scavenging during load step (schematical representation): The scavenging rate  $x_{sc}$  is related to the air/gas fraction leaving through Channel 4. The scavenging rate reaches its lowest value soon after the load-step command, since mass flow  $\dot{m}_{ch3chg}^*$  (and hence  $L_{pen}$ ) rises faster than  $p_{sc}$  (and thus the fluid acceleration).

response of a *first-order derivative lag element*, also known as a  $DT_1$  element. This new discovery will be useful in the control strategy described below.

## Chapter 5

# Control System Design and Verification

As mentioned in the introduction in Chapter 1, the main advantages of pressure-wave supercharged engines include the promising driveability, boost capacity at low engine speeds, and part load efficiency. Next to global constraints such as emission standards and noise reduction, the major controller requirements are therefore guided by efficiency and driveability.

- I. **Efficiency** in this context indicates the engine's thermal efficiency and thus the fuel consumption. Due to a bad supercharger efficiency, the pressure after the compressing process  $p_{\text{rec}2}$  is usually lower than the pressure before the expansion process  $p_{\text{rec}3}$  and the intake manifold pressure  $p_{\text{im}}$  is lower than the exhaust manifold pressure  $p_{\text{em}}$ , which causes pumping losses. The PWS's major advantage is its ability to keep the pressure  $p_{\text{rec}2} \approx p_{\text{rec}3}$  or even higher. The controller strategy thus should not deteriorate this advantage.
- II. **Driveability** designates a fast and precise system response to driver requests, mainly at low engine speeds, i.e. at low engine mass flows. In particular, the driver expects a fast, smooth, and steady engine torque rising after the accelerator is "tipped in".
- III. **Emission** standards have become very strict. The concept of exhaust gas aftertreatment presented in this text consists of two steps. While the three-way catalytic converter (TWC) between engine and supercharger reduces the nitrogen oxides

( $NO_x$ ) appearing, the second catalytic converter after Receiver 4 (OxCat) then oxidizes the remaining hydrocarbons (HC) and carbon oxides (CO) since there always occur lean conditions due to the scavenging air mass flow. However, the latter needs to be minimized since it considerably reduces the temperature  $T_{rec4}$  which may deteriorate the conversion rate in the (oxidation) catalytic converter (OxCat).

The engineer's "control authority" includes the five system actuators Throttle 1, Throttle 2, gas pocket valve, cell-wheel speed, and casing offset. However, the five-dimensional vector space that is spanned by these five control variables may reasonably be constrained by the following assumptions:

- I. Apart from a carefully designed, engine-matched charger layout, a PWS's best *efficiency* is reached for a well-tuned operation, i.e. under the conditions that were assumed while designing the casing geometry for a nominal operating point (Fig. 1.9). **Charger speed**  $n_{pws}$  and **casing offset**  $\alpha_{cas}$  therefore need to be set properly during the entire operation.
- II. The main torque actuators are **Throttle 2** (Th2) and the **gas pocket valve** (GPV). First considerations immediately lead to the proposal to open Throttle 2 and close the gas pocket valve as fast as possible to obtain maximum *driveability*. And in order to generate minimum pumping losses, i.e. minimum pressure differences  $p_{em}-p_{im}$ , Throttle 2 should be fully opened before the gas pocket valve is closed. However, the good  $p_{im}$  pressure build-up that the PWS concept is able to achieve, even for low engine mass flows, is useless in terms of driveability if exhaust gas is displacing oxygen in the combustion chamber and therefore lowers the engine torque. For PWS engines, driveability thus is intimately connected with **EGR control**, i.e. the avoidance of EGR.
- III. Best *emission* values and thus highest conversion rates are achieved for maximum  $T_{rec4}$  and therefore minimum scavenging mass flow. Throttling mass flow through Channel 1 by closing **Throttle 1** (Th1) is an effective method to lower the scavenging

mass flow (Pauli and Amstutz, 1989; Amstutz, 1991). However, a minimum scavenging rate  $x_{sc}$  is necessary to fulfill the driveability requirement. The trade-off problem is solved by closing Throttle 1 as much as possible in the normal case, while opening the throttle completely during fast acceleration maneuvers.

Each aspect of that split-up control concept will be handled separately in the following sections.

## 5.1 Controller I – Efficiency

As mentioned above, the Controller I is designed to ensure that the PWS generates the highest possible pressures in Receiver 2 ( $p_{rec2}$ ) with the lowest possible pressures in Receiver 3 ( $p_{rec3}$ ) during all operating conditions, using cell-wheel speed and casing offset as control inputs. In Fig. 3.5 the FDMdl simulates an operating point with too low a cell-wheel speed. The ideal case occurs, i.e. backflow from the cell into Channel 3 and from Channel 2 into the cell is precluded, when the first shock wave is reflected close to the edge of opening Channel 2 and when the returning shock wave  $w_{3o3}$  exactly hits the closing edge of Channel 3. These facts are not surprising since the casing geometry is designed with those occurrences in mind. The model here thus reflects the running times of the two first essential shock-waves, i.e.  $w_{3o1}$  and  $w_{3o2}$  (see Fig. 3.17). The controller is derived by inverting that model.

### 5.1.1 Realization

The basics for the calculation of the running times of the waves were elaborated in Sect. 3.2. In this section the model is slightly modified in that the deflection of the returning wave  $w_{3o2}$  at the contact front is also taken into account. The transmitted wave  $w_{3o2}$  travels slightly faster in the hot medium (exhaust gas). The calculation of the initial zone  $z_0$ , the first wave  $w_{3o1}$ , the first zone  $z_1$ , and of the reflected returning wave  $w_{3o2}$  has already been derived in Eqs.(3.49) to (3.55) in Sect. 3.2.2. The shock wave  $w_{3o3}$  thus underlies the same pressure

ratio as  $w_{3o2}$  and its velocity follows as:

$$\begin{aligned}\pi_{3o3} &= \pi_{3o2} \\ u_{w3o3} &= f_{\text{WaveVel}}(u_{z1e}, T_{z1e}, p_{z1e}, p_{z1}, \kappa, R, \leftarrow) \\ &= u_{z1} - \sqrt{\frac{RT_{z1e}}{2}} \sqrt{\pi_{3o2} (n_{3o2} + 1) + n_{3o2} - 1}\end{aligned}\quad (5.1)$$

The running times of the waves at the reflection point  $t_{3o1}$ , intersection point  $t_{3o2}$ , and returning point  $t_{3o3}$  then are calculated from the rotor length  $L_{\text{rot}}$  and fluid and wave speeds.

$$\begin{aligned}t_{3o1} &= \frac{L_{\text{rot}}}{u_{w3o1}} \\ t_{3o2} &= \frac{t_{3o1} u_{w3o2} + L_{\text{rot}}}{u_{w3o2} + u_{z1}} \\ t_{3o3} &= t_{3o2} + \frac{L_x}{u_{w3o3}} \quad \text{with} \quad L_x = \frac{t_{3o1} u_{w3o2} + L_{\text{rot}}}{u_{z1} (u_{w3o2} + u_{z2})}\end{aligned}\quad (5.2)$$

The nominal cell-wheel speed  $n_{\text{pws,nom}}$  follows from a comparison of the wave running time  $t_{3o3}$  with the time that is required to turn the cell wheel over the opening angle of Channel 3,  $\alpha_{\text{ch3}}$ .

$$\underbrace{\frac{60}{n_{\text{pws,nom}}}}_{\text{time for 1 rotation [s]}} \cdot \underbrace{\frac{\alpha_{\text{ch3}}}{360^\circ}}_{\text{rotational fraction}} \stackrel{!}{=} t_{3o3} \quad (5.3)$$

$$n_{\text{pws,nom}} = \frac{\alpha_{\text{ch3}}}{360^\circ} \frac{60}{t_{3o3}} \quad [\text{rpm}] \quad (5.4)$$

Similarly, the *theoretical* casing offset angle  $\alpha_{\text{cas,theo}}$  is the result of the comparison of the wave running time  $t_{3o1}$  with the time  $t_{\text{ch2o}}$  until Channel 2 opens.

$$\frac{60}{n_{\text{pws,nom}}} \cdot \frac{\alpha_{\text{cas,theo}}}{360^\circ} \stackrel{!}{=} t_{3o1} \quad (5.5)$$

$$\alpha_{\text{cas,theo}} = \frac{t_{3o1}}{t_{3o3}} \alpha_{\text{ch3}} \quad [^\circ] \quad (5.6)$$

Operating the PWS with  $\alpha_{\text{cas,theo}}$  and  $n_{\text{pws,nom}}$ , the first wave theoretically would be reflected exactly when Channel 2 opens. However,

experiments have shown that better efficiencies result for higher loads if the casing offset  $\alpha_{\text{cas}}$  is corrected by  $\Delta\alpha_{\text{cas}}$  (Fig. 5.2). The angular difference  $\Delta\alpha_{\text{cas}}$  is approximately half of the angle obtained when the cell wheel is rotated by one cell width.

$$\Delta\alpha_{\text{cas}} \simeq 0.5 \alpha_{\text{cell}} = \frac{360^\circ}{N_{\text{cells}}} \quad (5.7)$$

The angular difference  $\Delta\alpha_{\text{cas}}$  causes the fluid in the cell to be decelerated by the right boundary condition “wall”. The result is a higher pressure after the reflected wave and thus a higher mass flow  $\dot{m}_{\text{ch2}}^*$ . Hence, the *nominal* casing offset angle  $\alpha_{\text{cas,nom}}$  is:

$$\alpha_{\text{cas,nom}} = \alpha_{\text{cas,theo}} + \Delta\alpha_{\text{cas}} \quad (5.8)$$

In Fig. 5.1, the concept of controller I is displayed in condensed form.

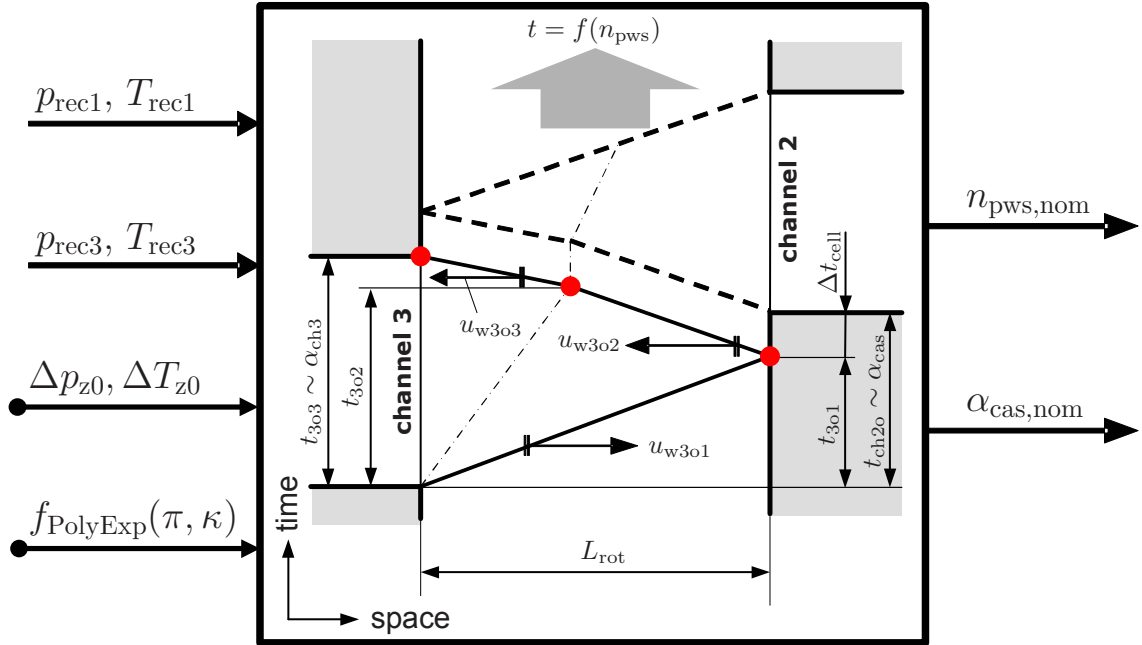


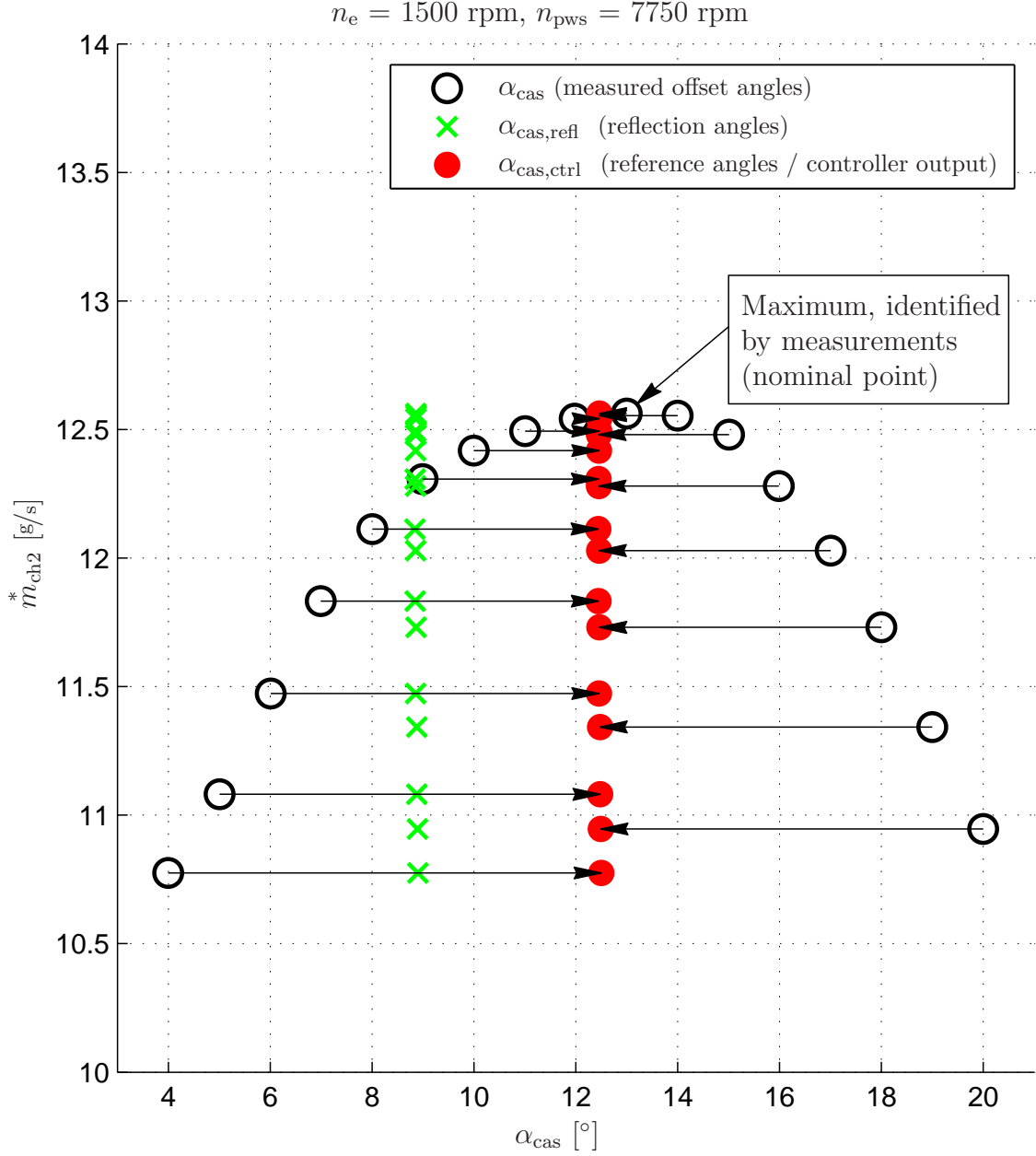
**Figure 5.1:** Scheme of Controller I: Using the states in Receiver 1 and Receiver 3 and estimating compression and reflection efficiencies, the wave running times are calculated.

### 5.1.2 Verification

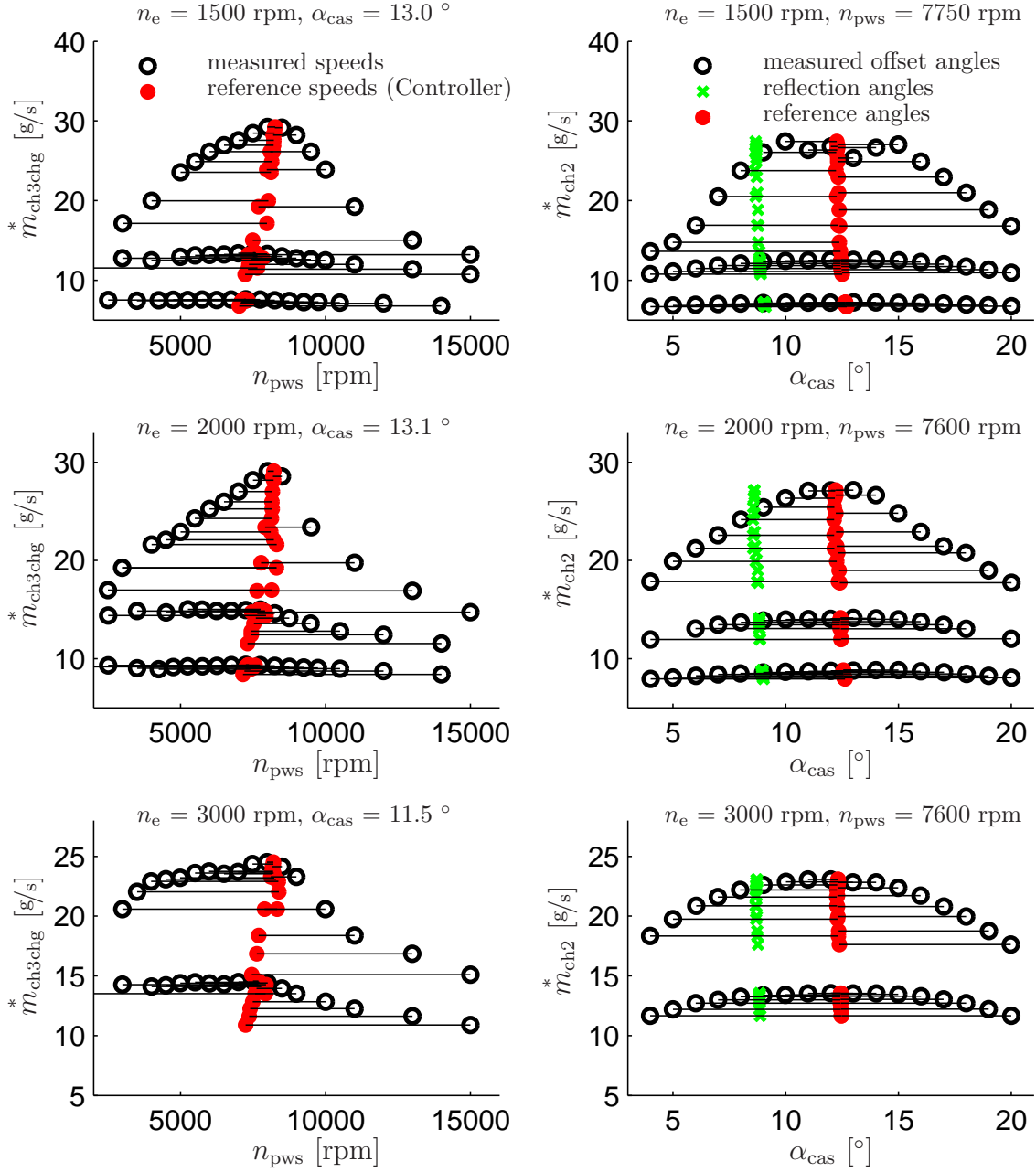
Controller I was implemented and verified on the EA111/HX95 engine test rig (see App. A). In Fig. 5.2, for one operating point in the engine map (2000 rpm, 70 Nm), the casing offset was varied over a wide range. The measured values  $\dot{m}_{\text{ch2}}^*$  are plotted over the variations of  $\alpha_{\text{cas}}$ . As Fig. 5.2 clearly shows, even for operating conditions far beyond the optimum, i.e. the maximum possible mass flow  $\dot{m}_{\text{ch2}}^*$ , the current values of  $p_{\text{rec1}}$ ,  $T_{\text{rec1}}$ ,  $p_{\text{rec3}}$ , and  $T_{\text{rec3}}$  direct the controller to point towards the maximum. For operation conditions close to the optimum, i.e., where no backflow into Channel 2 is expected, the proposed value for  $\alpha_{\text{cas}}$  does not differ much from the optimal values identified by measurements.

Figure 5.3 shows that for very different engine operating conditions the reference values from Controller I remain close to the optimum values.





**Figure 5.2:** Casing offset variation at 1500 rpm, medium load (Nominal point: 70 Nm, 8.8 bar BMEP). For each measured steady-state variation point (black circles), signals such as  $n_{pws}$ ,  $\alpha_{cas}$ ,  $p_{rec1}$ ,  $p_{rec3}$ ,  $T_{rec1}$ , are  $T_{rec3}$  are captured. Pressures and temperatures are the inputs for Controller I. The Controller output (red dots) is always close to the value where maximum mass flow  $\dot{m}_{ch2}^*$  is achieved. Corresponding measured  $\alpha_{cas}$  and controller outputs  $\alpha_{cas,ctrl}$  are connected by an arrow. The green x indicate  $\alpha_{cas,refl}$ , i.e. the angle where the wave  $w_{3o1}$  is reflected. Even for operating conditions far beyond the optimum, i.e. maximum mass flows, the controller values always point close to the optimum.



**Figure 5.3:** Verification of Controller I for eight operating points (low, medium, and high load at 1500, 2000, and 3000 rpm). Left columns:  $n_{pws}$  is varied over a wide area. For each steady-state measurement (black circles), the controller output angle  $\alpha_{cas,ctrl}$  (red dots) is close to the speed where maximum mass flows  $\dot{m}_{ch3chg}$  are achieved. Corresponding measured  $n_{pws}$  and controller output  $n_{pws,ctrl}$  are connected with black lines. Right columns: Similarly, variations in  $\alpha_{cas}$  are compared to their controller output values  $\alpha_{cas,ctrl}$ . The green x indicate  $\alpha_{cas,refl}$ , i.e. the angle where the wave  $w_{3o1}$  is reflected. Clearly the reference values from Controller I remain close to the optimum values.

## 5.2 Controller II – Driveability

A driver-requested fast, smooth, and steady engine torque response in a pressure-wave supercharged engine is not simply achievable by a fast opening of Throttle 2 and a simultaneous closing of the gas pocket valve. Although the intake manifold pressure  $p_{im}$  is built up quickly, some temporarily recirculated exhaust gas is to be expected in Channel 2 causing the engine torque to drop sharply.

The problematic nature of controlling EGR is that the start of an EGR event during a load step cannot be detected fast enough. Any interventions must be predisposed in order to keep **any** exhaust gases from entering Channel 2. Therefore, a control variable has to be found that allows to reliably predict a beginning EGR event. As proposed in Amstutz (1991) and proven earlier in this text, the scavenging rate as an indicator for the amount of fresh air leaving through Channel 4 is the favored variable to be controlled. This control concept is based on the fact that the EGR rate  $x_{egr} = \dot{m}_{egr}^*/\dot{m}_{ch2}^*$  is linked to the scavenging rate  $x_{sc} = \dot{m}_{14}^*/\dot{m}_{ch2}^*$  and that it is thus possible to substitute the scavenging rate  $x_{sc}$  for the EGR rate  $x_{egr}$  as the control variable.

A fast, steady and smooth torque formation, achieved by avoiding EGR therefore can be guaranteed by keeping the scavenging rate  $x_{sc}$  above a certain level  $x_{sc,min}$ . This rate is estimated using  $y_{th2}$  and  $y_{gpv}$  as main inputs. During fast acceleration maneuvers a precise prediction of  $x_{sc}$  is necessary since the feedback signals for estimating  $x_{sc}$  (i.e.  $\dot{m}_{ch1}^*$  and  $\dot{m}_{ch2}^*$ , or  $\lambda_{em}$  and  $\lambda_{rec4}$ ) are subject to time delays. The required predictor is realized using a linear first-order derivative lag element ( $DT_1$ ) in combination with a non-linear static function.

The top graphs in Fig. 5.4 show the input/output behavior of a  $DT_1$  element for a step input. The required output signal, i.e. the demand to keep  $x_{sc}$  above the level  $x_{sc,min}$  is achieved when the step input is replaced by a step-ramp signal (Fig. 5.4, bottom row). As soon as  $x_{sc}$  reaches its lower boundary value, the input needs to be closed more slowly with respect to the time constant of the lag element.

A nonlinear function describes the static relation between the actuator input signals (Th2, GPV) and the scavenging rate  $x_{sc}$ . Investigations demonstrate that a fast opening of Throttle 2 is not critical in terms of EGR, except for very low engine temperatures, i.e. during cold start. Hence, the step-ramp behavior may be

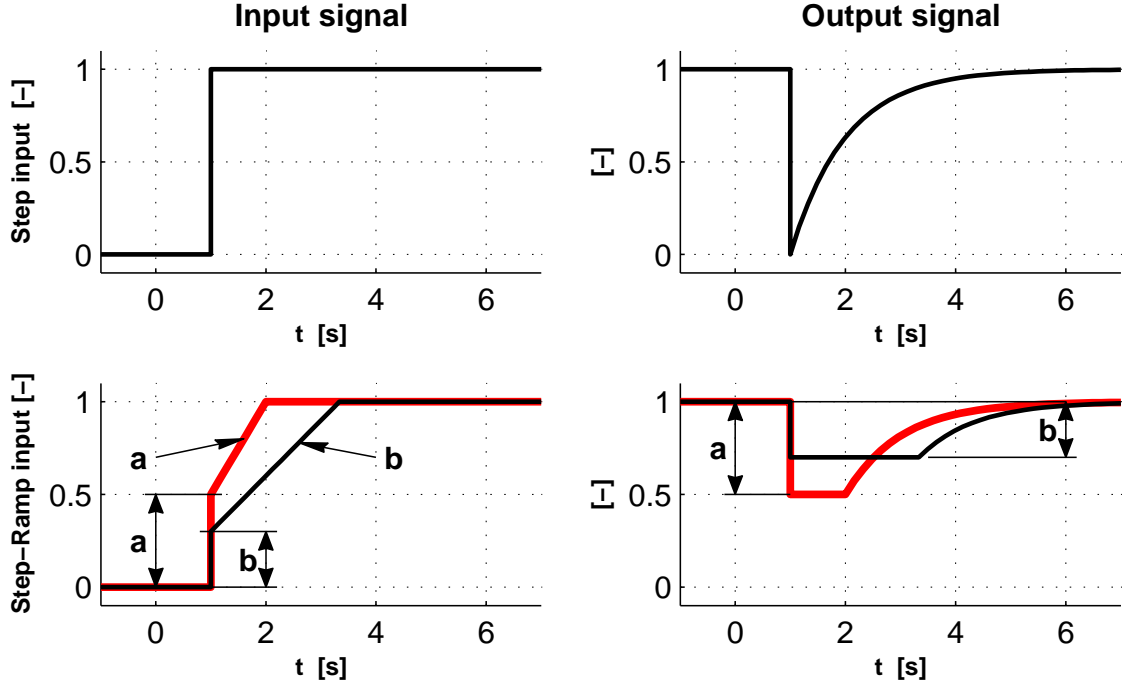


**Figure 5.4:** Three examples of the input/output behavior of a  $DT_1$  element (first-order derivative lag element). Left column: input signals, right: output signals. Top row: step input, bottom: step-ramp input. A step-ramp input results in the required (lower limited) output signal.

assumed to be close to the optimal trajectory of the gas pocket valve. This is a verification of the solution presented in Spring et al. (2003). There, the optimal feed-forward trajectories for the throttle 2 and the gas pocket valve are found by applying a shooting method on the model presented in Weber (2001), i.e. on a model of the SAB 360ccm COMPREX<sup>®</sup>(SAB360/CX64) engine system as presented in Appendix A.

### 5.2.1 Realization

Figure 5.5 shows the proposed control concept in a schematic overview. The implementation on the testbench engine system is carried out in the following three steps (see also Figs. 5.6-5.8):

1. Respecting the specified lower boundary  $x_{sc,min}$  the maximum acceptable engine mass flow  $\dot{m}_{im,max}^* \approx \dot{m}_{ch2,max}^*$  is calculated

from the minimum expectable, measured, or estimated  $\dot{m}_{\text{ch1}}^*$ :

$$\dot{m}_{\text{ch2,max}}^* = \frac{\dot{m}_{\text{ch1,min}}^*}{x_{\text{sc,min}} + 1} \quad (5.9)$$

2. The mass flow  $\dot{m}_{\text{im,WOT}}^*$  designates the mass flow through Channel 2 and engine for a wide open Throttle 2 (WOT). The calculation is performed using the engine mass flow model presented in Sect. 2.4.

$$\dot{m}_{\text{im,WOT}}^* = f(p_{\text{im,WOT}}, T_{\text{im}}, p_{\text{em}}, n_{\text{e}}, V_{\text{d}}) \quad (5.10)$$

For steady-state conditions, the intake manifold pressure for a wide open Throttle 2 ( $p_{\text{im,WOT}}$ ) is a function of the engine speed and of the temperature of the exhaust gas before it enters the charger.

$$p_{\text{im,WOT}} = f(n_{\text{e}}, T_{\text{rec3}}) \quad (5.11)$$

The mass flow margin

$$\Delta \dot{m}_{\text{im,gpv}}^* = \dot{m}_{\text{ch2,max}}^* - \dot{m}_{\text{im,WOT}}^* \quad (5.12)$$

is an indicator of how much the gas pocket valve may be closed.

3. Estimating the influence of the degree the gas pocket valve is closed  $y_{\text{gpv}}$  on  $p_{\text{im}}$  and on  $\dot{m}_{\text{im}}^*$ , the maximum closing degree  $y_{\text{gpv,max}}$  can be calculated from  $\Delta \dot{m}_{\text{im,gpv}}^*$ :

$$y_{\text{gpv,max}} = f(\Delta \dot{m}_{\text{im,gpv}}^*) \quad (5.13)$$

Reference values for Throttle 2 and the gas pocket valve can be calculated from the torque desired by the driver. While the position of Throttle 2 is controlled according to its reference value  $y_{\text{th2,ref}}$ , the reference position for the gas pocket valve is limited to  $y_{\text{gpv,max}}$ . This guarantees a minimum scavenging rate.

For the purpose of cost reduction, the air mass flow meter in Channel 1 may be omitted if the mass flow through Channel 1 is estimated reliably. A “conservative” estimation for  $\dot{m}_{\text{ch1}}^*$  is realized by isolating

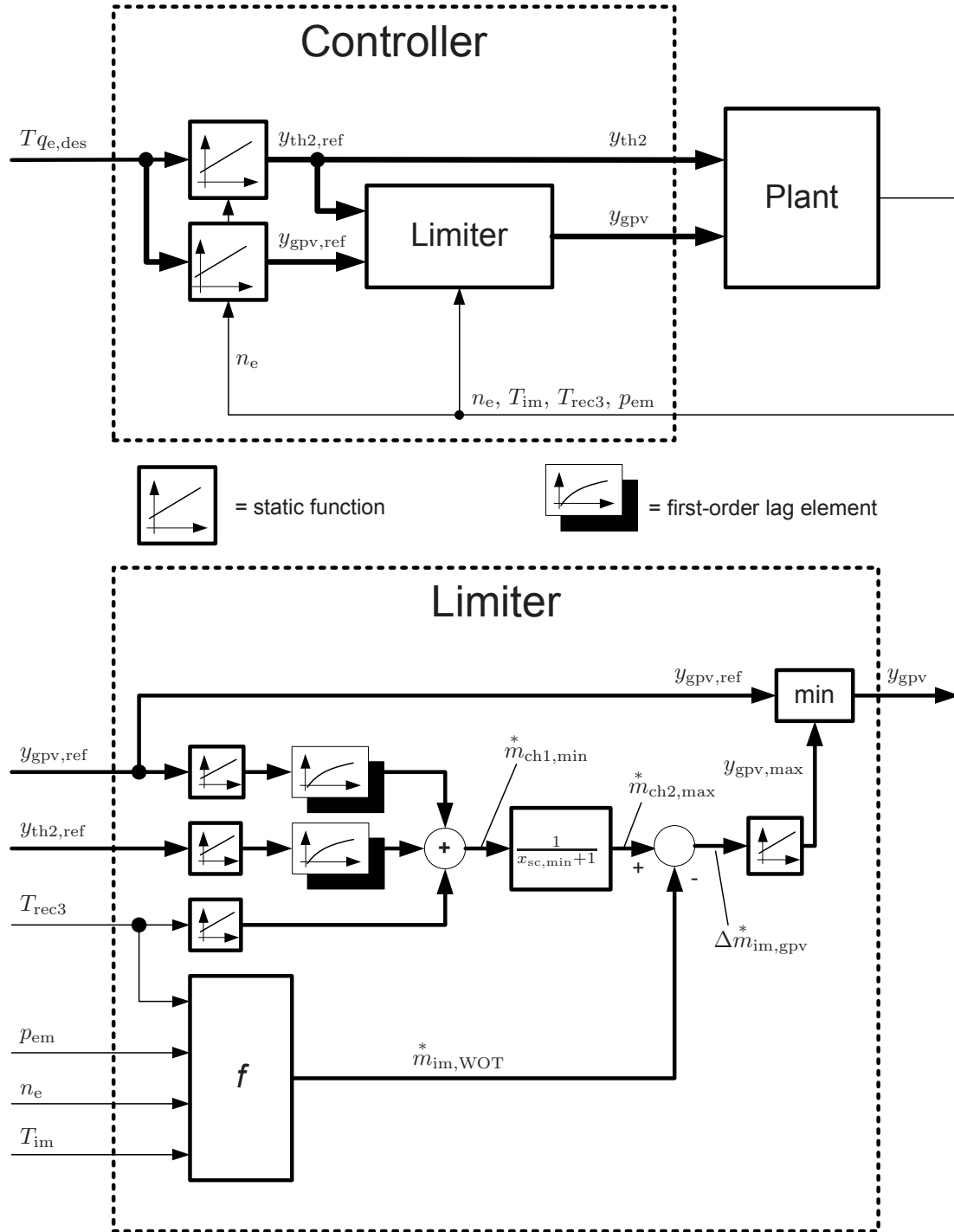


**Figure 5.5:** Scheme of Controller II: The gas pocket valve ( $y_{gpv}$ ) is restricted with respect to a minimum scavenging rate  $x_{sc,min}$ .

the static influences caused by Throttle 2, gas pocket valve, engine speed, and operating temperature, and by modeling the dynamic characteristics using two first-order lag ( $PT_1$ ) elements ( $\tau_{th2}$ ,  $\tau_{gpv}$ ),

$$\dot{m}_{ch1,est}^* = \dot{m}_{ch1,th2}^* + \dot{m}_{ch1,gpv}^* + \dot{m}_{ch1,T3}^* \quad (5.14)$$

where

$$\begin{aligned} \dot{m}_{ch1,T3}^* &= f(T_{rec3}) \\ \frac{d}{dt} \dot{m}_{ch1,th2}^* &= \frac{1}{\tau_{th2}} \left( f(y_{th2}) - \dot{m}_{ch1,th2}^* \right) \\ \frac{d}{dt} \dot{m}_{ch1,gpv}^* &= \frac{1}{\tau_{gpv}} \left( f(y_{gpv}) - \dot{m}_{ch1,gpv}^* \right) \end{aligned} \quad (5.15)$$

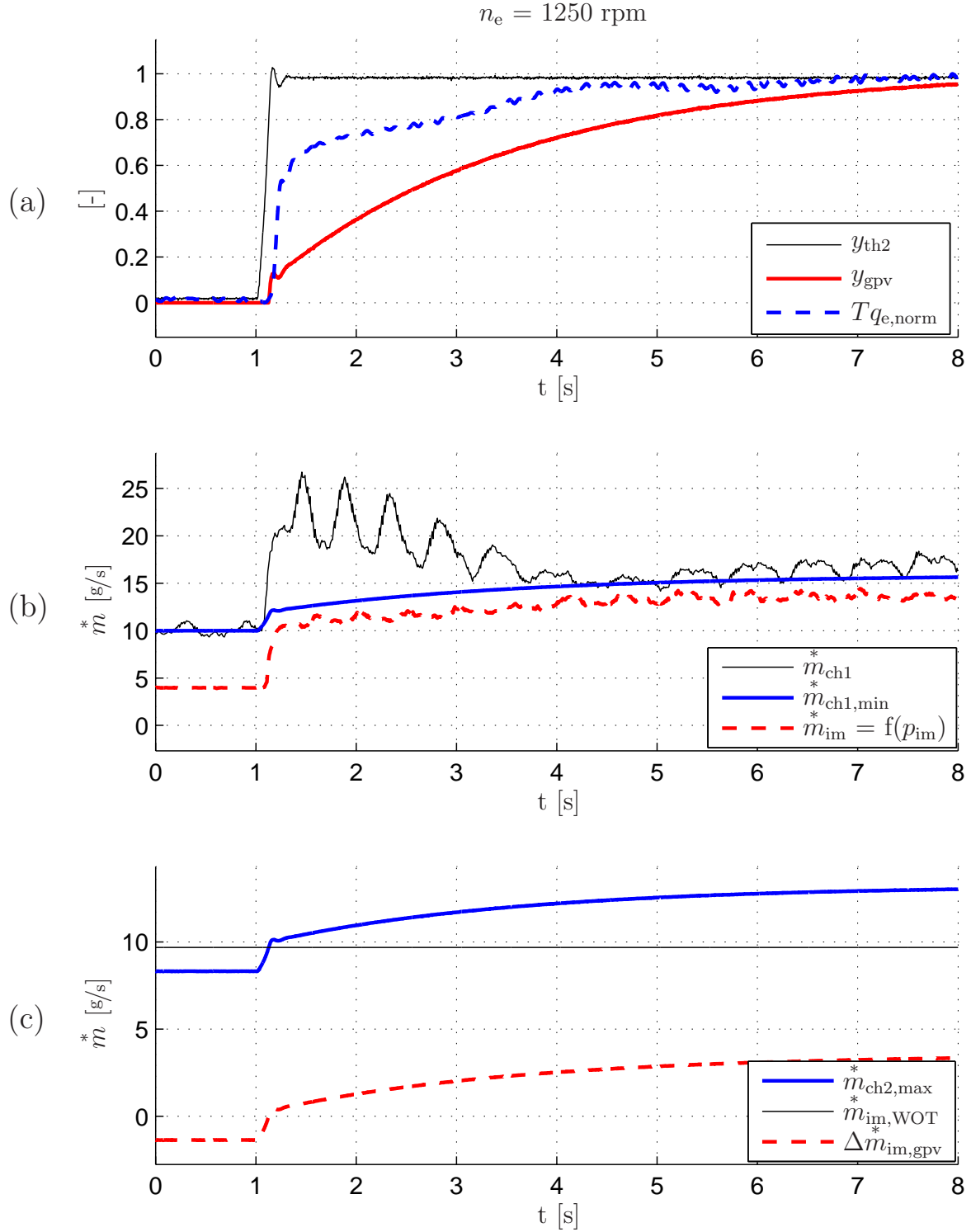
The structure of equations (5.14) and (5.15) is illustrated in Fig. 5.5. The time lags  $\tau_{th2}$  and  $\tau_{gpv}$  represent the two delays caused by changes in the positions of Throttle 2 and of the gas pocket valve, respectively. On the one hand, opening Throttle 2 causes a fast pressure equalization between Receiver 2 and the intake manifold and thus a higher mass flow through Channel 2. The increasing mass flow  $\dot{m}_{ch2}^*$  partially raises the mass flow through Channel 1  $\dot{m}_{ch1}^*$ . On the other hand, closing the gas pocket valve has a relatively slow effect on the scavenging process due to heat transfer in the engine exhaust manifold.

### 5.2.2 Verification

The control concept illustrated in Fig. 5.5 is implemented and experimentally verified at three engine speeds. For 1250, 1500, and 2000 rpm, well-controlled load steps from very low load to full load are depicted in Fig. 5.6, Fig. 5.7, and Fig. 5.8. The top subplots (a) show the measured actuator signals  $y_{th2}$  and  $y_{gpv}$  as well as the resulting measured engine torque over time. Note that the engine torque is normalized with its maximum (final) value. Due to higher accessibility requirements, the intake receivers are much larger on the test bench compared to a car engine. Therefore the torque build-up is relatively slow. The center subplots (b) display both measurement results and conservative estimations of the mass flows through Channel 1. The

term “conservative” in this context means that the estimated mass flow  $\dot{m}_{\text{ch1,min}}^*$  is always lower than the real value  $\dot{m}_{\text{ch1}}^*$  measured with the air mass flow meter. The mass flow  $\dot{m}_{\text{im}}^*$  is calculated using the measured  $p_{\text{im}}$ ,  $p_{\text{em}}$  and  $T_{\text{im}}$  signals as inputs for the engine model described in Sect. 2.4. The bottom subplots (c) show how  $\Delta\dot{m}_{\text{im,gpv}}^*$  follows from the difference  $\dot{m}_{\text{ch2,max}}^* - \dot{m}_{\text{im,WOT}}^*$ . The engine mass flow  $\dot{m}_{\text{ch2,max}}^*$  is derived from  $\dot{m}_{\text{ch1,min}}^*$  using Eq. (5.9) with the assumption of a minimum scavenging rate  $x_{\text{sc,min}}$ . The mass flow  $\dot{m}_{\text{im,WOT}}^*$  designates the engine mass flow for a wide open Throttle 2 for a certain engine speed. The maximum gas pocket valve signal  $y_{\text{gpv,max}}$  is then derived from the mass flow difference  $\Delta\dot{m}_{\text{im,gpv}}^*$  using a linear function. Clearly, the engine torque is now rising steadily and smoothly.



Figure 5.6: Verification of Controller II for  $n_e = 1250 \text{ rpm}$

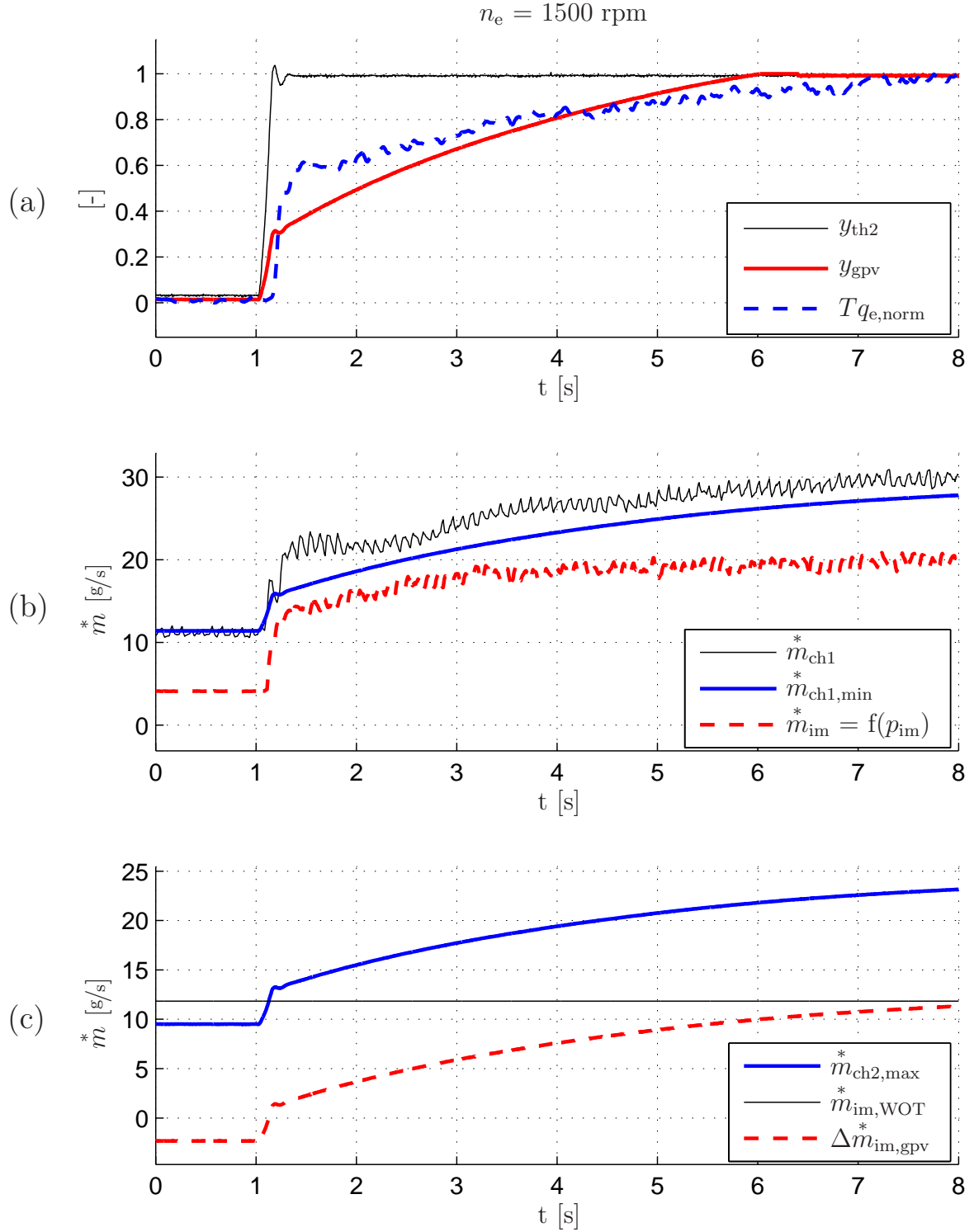
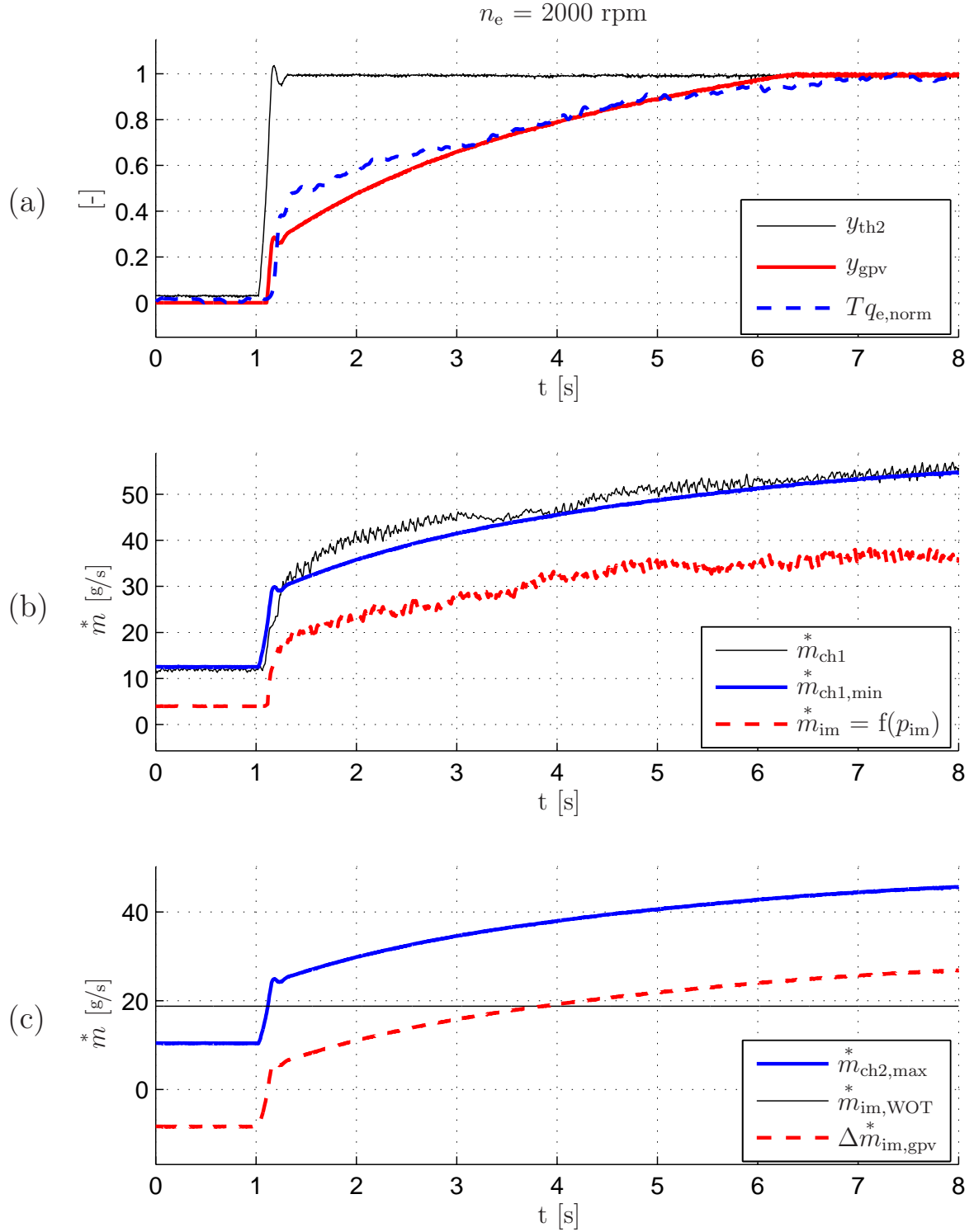
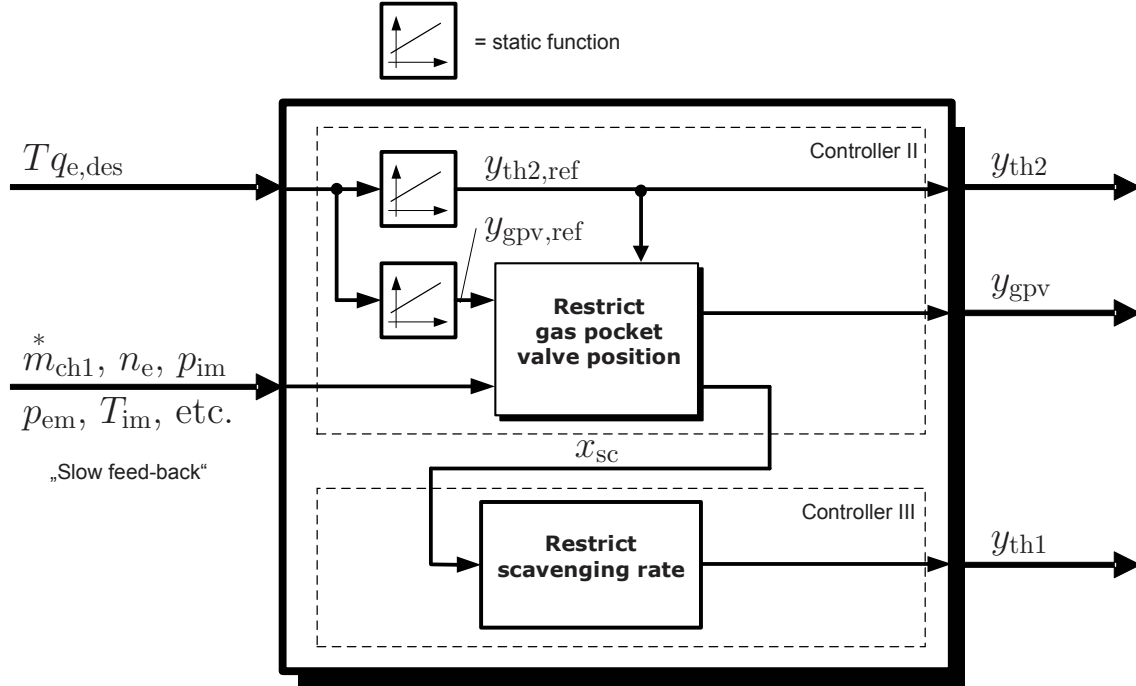


Figure 5.7: Verification of Controller II for  $n_e = 1500 \text{ rpm}$

Figure 5.8: Verification of Controller II for  $n_e = 2000 \text{ rpm}$

### 5.3 Controller III – Maximum $T_{\text{rec}4}$

Better emission values and higher conversion rates are achieved for higher  $T_{\text{rec}4}$  and minimum scavenging mass flows. Throttling the mass flow through Channel 1 by partially closing Throttle 1 is the only effective method to lower the scavenging mass flow, which is a goal contrary to the driveability postulation. The trade-off problem is to be solved by maintaining  $x_{\text{sc}}$  below a certain limit  $x_{\text{sc,max}}$  in the normal case, while opening the throttle completely during fast acceleration maneuvers. Based on the scavenging rate  $x_{\text{sc}}$  the controller closes Throttle 1 at  $x_{\text{sc}} \approx x_{\text{sc,max}}$ . But as soon as  $x_{\text{sc}}$  falls below  $x_{\text{sc,crit}}$ , the scavenging process is no longer affected negatively, and Throttle 1 is fully opened (see Fig. 5.9).



**Figure 5.9:** Scheme of Controllers II and III: whereas Controller II must guarantee  $x_{\text{sc}}$  to remain above the minimum  $x_{\text{sc,min}}$  to maintain driveability, Controller III keeps  $x_{\text{sc}}$  below the upper level  $x_{\text{sc,max}}$  by partially closing Throttle 1. The scavenging rate  $x_{\text{sc}}$  is therefore adopted from Controller II.

## Chapter 6

# Conclusions and Outlook

This thesis analyzes the application of so-called pressure-wave superchargers (PWS) with spark-ignition (SI) engines. It presents an alternative way to control the load of an SI engine with reduced throttling. By reducing the engine displacement and compensating the smaller engine size by supercharging using a PWS, a fast engine torque response and a high boost pressure over the entire engine speed range are achieved.

Current pressure-wave supercharging devices present the option of arbitrarily setting the gas pocket valve position, the cell-wheel speed, and the angle offset between air and gas casing. From a control-oriented point of view these actuators are considered as inputs of the PWS system which cause a multitude of cross couplings towards the PWS system outputs, such as the mass flows. Particularly the mass flow through Channel 2, where the compressed air leaves the PWS to the engine, is important since it directly affects the engine torque. Therefore, it is important to understand the main effects and phenomena that take place in a PWS.

Section 3.1 describes a universally valid PWS model in which a set of Euler-type partial differential equations is numerically solved using a finite-difference method. One-dimensional, unsteady gas dynamics in the cell wheel are simulated, taking into account such phenomena as leakage, heat transfer, friction, and varying actuator inputs. The validation with measurement data from a PWS-boosted engine shows an error of less than 6% in a large operating range.

The finite-difference model shows the influences of model inputs such as pressures and model parameters on the model outputs. Initial experiments proved that even a small change in the value of a pressure

input immediately affects *all* the outputs. The sensitivity of the mass flows to pressure and temperature proves to be a very important issue. For instance, if the PWS model is used in a loop with an engine model, the input/output behavior of the PWS model is critically important for a stable simulation. Due to the high sensitivities of the model, small errors in the pressure signals are strongly amplified and may cause the calculation to fail. The sensitivity analysis thus proves that the lumped pressures, measured at the test bench engine, may not be used as inputs for the PWS model. Therefore, the core PWS model is extended by four receivers, enabling the channel mass flows to act as system inputs. With this method, the sensitivities of the results to measuring errors are significantly reduced. The finite-difference model is a versatile tool for visualizing and investigating the pressure-wave processes for very different operating points.

The control-oriented mean-value model described in Sect. 3.2 is then derived on the basis of the finite-difference model. As it is restricted to the simulation of the essential physical effects, it saves considerable computational time. This static PWS model is thus implemented in a dynamic model in order to simulate the transient behavior of the entire engine system. Ordinary differential equations describe the relevant dynamics of the lumped pressures and temperatures in the manifolds of the engine system.

The dynamic model proved to be useful to understand the mechanisms of transient exhaust gas recirculation (EGR), a phenomenon which was observed during experiments on the test bench. During tip-in maneuvers, critical situations arise when large amounts of exhaust gas are recirculated over the PWS from the exhaust to the intake manifolds. This causes the engine torque to drop sharply. In order to prevent such situations, the actuators such as throttles, valves, etc., have to be controlled in a coordinated way.

All the previously introduced tools and investigations such as FDMdl, MVMdl, engine system model and closed-loop simulation are used to design off-line a new system consisting of three controllers. Open-loop Controller I causes the PWS to operate at optimal efficiency. Cell-wheel speed and casing offset are defined using a model for the running times of the first two essential shock waves. Feed-forward Controller II maintains good driveability by limiting the EGR effects that cause torque drops. The control concept is based

on the fact that the EGR rate is linked to the scavenging rate, an indicator for the amount of fresh air leaving through Channel 4 of the PWS. The scavenging rate  $x_{sc}$  is thus substituted for the EGR rate  $x_{egr}$  as a control variable. A fast, steady, and smooth torque formation, achieved by avoiding EGR, therefore is guaranteed by maintaining the scavenging rate  $x_{sc}$  above a certain level  $x_{sc,min}$ . Step functions of the desired engine torque  $Tq_{e,des}$  caused by a driver's tip-in command are filtered with respect to the predicted scavenging rate. This prediction is based on the engine speed, the intake and exhaust manifold pressures, and the temperature of the exhaust gas entering the PWS. While Throttle 1 is completely opened during fast acceleration maneuvers, Controller III closes Throttle 1 if the predicted scavenging rate  $x_{sc}$  has reached its upper limit  $x_{sc,max}$ . This way the temperature in the outlet is kept as high as possible, which keeps the exhaust gas aftertreatment process working properly. Experimental verifications on the engine test bench for the two Controllers I and II are presented for various operating conditions.

Pressure-wave supercharged SI engines are not yet considered to be suitable for everyday use. Their full-load compatibility has not yet been demonstrated, and more investigations have to be conducted on the subjects of cold-start and back-pressure sensitivity.

For the latter, a first-principle model is necessary to physically derive the relation between scavenging rate and EGR rate, i.e. the mixing phenomena of exhaust gas and fresh air. While phenomenological approaches have been tested, the model does not satisfactorily represent the reality over a wide operating range as yet.

For cold-start investigations, the model presented needs to be extended to analyze the sensitive influence of the casing temperature on the mass flows  $\dot{m}_{ch1}^*$  and  $\dot{m}_{ch4}^*$  in the low-pressure part.

However, PWS SI engines show great promise for efficiency and dynamics. Without any loss of generality, the models and concepts presented may be transferred to diesel and HCCI engine applications. Materials research, design, and modern control hardware can guarantee a robust system operation. The processes may be controlled in real-time using model-based algorithms. Although the underlying processes are complex, the system behavior is predictable.

The future implementation of the control systems presented in this

work will increase the acceptance of the fuel-efficient pressure-wave supercharged engines and thus help to reduce fuel consumption of passenger cars.



## Appendix A

# Experiments

The engine system under consideration, called *EA111/HX95* and also known as *SAVE* engine, consists of a modern HYPREX PWS (HX95), mounted onto a production type VW GOL 1-liter 4-cylinder 16-valve engine (EA111) (see Figure A.1). The GOL engine is originally equipped with a turbocharger as described in Frei (2004). A new feature presented by the HYPREX PWS is the possibility to set an arbitrary angle between air and gas casings.

For the validation of the FDMdl, additional measurement data were used from a small SWISSAUTO 360 *ccm* spark-ignition 2-cylinder flat-twin engine (SAB360) supercharged with a COMPRES<sup>®</sup>(CX64) with a gas pocket valve. This engine was part of the SMILE project, described in the publications of Guzzella and Martin (1998), Cortona (2000), Soltic (2000), Pfiffner (2001), and Weber (2001).

The technical data of both systems are summarized in Table A.1.

### A.1 Engine Test Rig

Apart from the validation of the FDMdl presented in Fig. 3.15, all measurements and investigations took place on the EA111/HX95 engine (Fig. A.1). The engine is equipped with a number of pressure, temperature, mass flow, speed, and lambda sensors, a sample of which is depicted in Figure 1.3. The static receiver pressures were measured in the ambient ( $p_{\text{amb}}$ ), around the PWS ( $p_{\text{rec1}}$ ,  $p_{\text{rec2}}$ ,  $p_{\text{rec3}}$ ,  $p_{\text{rec4}}$ ), and in the intake manifold ( $p_{\text{im}}$ ). Temperatures were captured in the ambient ( $T_{\text{amb}}$ ), around the PWS ( $T_{\text{rec1}}$ ,  $T_{\text{rec2}}$ ,  $T_{\text{rec3}}$ ,  $T_{\text{rec4}}$ ), behind the intercooler ( $T_{\text{ic}}$ ), and in the intake and the exhaust manifolds ( $T_{\text{im}}$ ,  $T_{\text{em}}$ ). Moreover, engine output torque  $Tq_e$ , engine speed  $n_e$ , air-

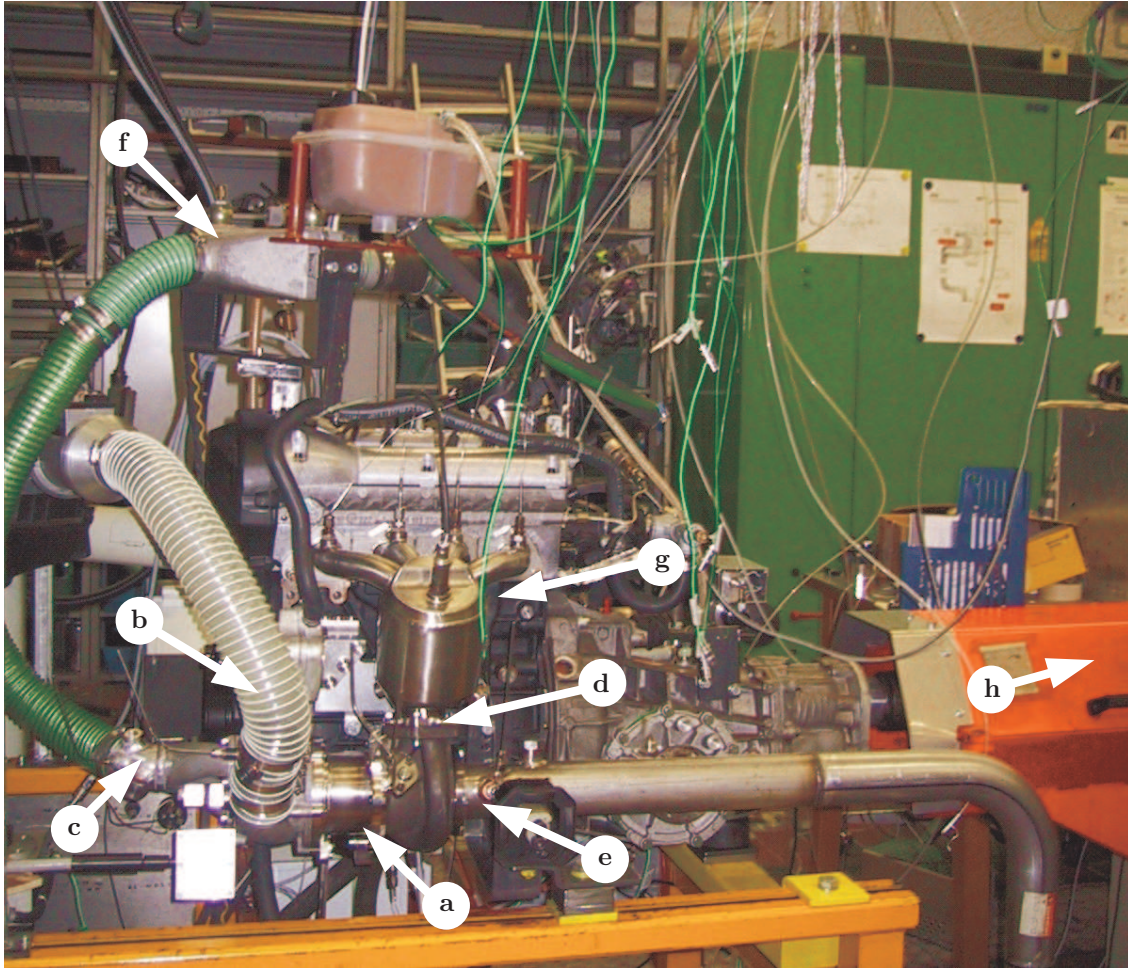


**Figure A.1:** The EA111/HX95 engine test rig: The engine is coupled with an asynchronous motor which works as a dynamic brake. It is controlled such that a desired load torque profile is imposed on the crank shaft. Details:

- |                                  |                   |                |
|----------------------------------|-------------------|----------------|
| a) pressure-wave supercharger    | b) Channel 1      | c) Channel 2   |
| d) Channel 3                     | e) Channel 4      | f) intercooler |
| g) three-way catalytic converter | h) electric motor |                |

to-fuel-ratio in the exhaust manifold ( $\lambda_{em}$ ) and in the outlet ( $\lambda_{rec4}$ ), fuel mass flow ( $\dot{m}_f^*$ ), and the air mass flow through Channel 1 ( $\dot{m}_{ch1}^*$ ) were measured. For specific EGR measurements, samples are captured in Receiver 2 ( $c_{rec2}$ ), Receiver 3 ( $c_{rec3}$ ), and Receiver 4 ( $c_{rec4}$ ) and conducted to the gas spectrum analyzer.

**Table A.1:** Technical specifications of the VW GOL 1.0 16V (EA111/HX95) and the SAB 360 ccm (SAB360/CX64) engine systems

|                              | EA111/HX95<br>("SAVE")        | SAB360/CX64<br>("SmILE")     |
|------------------------------|-------------------------------|------------------------------|
| peak power                   | 100 kW @5000 rpm <sup>1</sup> | 40 kW @5500 rpm <sup>2</sup> |
| rated torque                 | 200 Nm @1400 rpm <sup>1</sup> | 57 Nm @3000 rpm <sup>2</sup> |
| displaced volume             | 999 ccm                       | 358 ccm                      |
| stroke                       | 67.1 mm                       | 54 mm                        |
| bore                         | 70.6 mm                       | 65 mm                        |
| compression ratio            | 10.5 : 1                      | 9 : 1                        |
| number of cylinders          | 4 (in-line)                   | 2 (flat-twin)                |
| number of valves             | 16                            | 4                            |
| cell-wheel length & diameter | 95 mm                         | 64 mm                        |

<sup>1</sup> source: SWISSAUTO WENKO

<sup>2</sup> source: Soltic (2000)

## A.2 Reference Data

Based on the raw measurements as described in Section A.1, more reference data may be calculated.

**Engine mass flows** ( $\dot{m}_{\text{air}}^*$ ,  $\dot{m}_{\text{eg}}^*$ ): Neglecting fast wall-wetting dynamics and transport phenomena, considerations of stoichiometry immediately lead to the air and exhaust mass flows:

$$\dot{m}_{\text{air}}^* = \dot{m}_{\text{fl}}^* \lambda_{\text{em}} (A/F)_{\text{s}} \quad (\text{A.1})$$

$$\dot{m}_{\text{eg}}^* = \dot{m}_{\text{fl}}^* (1 + (A/F)_{\text{s}} \lambda_{\text{em}}) \quad (\text{A.2})$$

**Mass flow through Channel 4** ( $\dot{m}_{\text{ch4}}^*$ ): As presented in the Sankey diagram in Figure 1.5, the mass flow  $\dot{m}_{\text{ch4}}^*$  can be understood as the sum of scavenging mass flow  $\dot{m}_{14}^*$ , engine air mass flow  $\dot{m}_{\text{air}}^*$ , and fuel mass flow  $\dot{m}_{\text{fl}}^*$ .

$$\dot{m}_{\text{ch4}}^* = \dot{m}_{14}^* + \dot{m}_{\text{air}}^* + \dot{m}_{\text{fl}}^* \quad (\text{A.3})$$

For steady-state operating conditions, the mass flow  $\dot{m}_{\text{ch4}}^*$  reads as follows:

$$\dot{m}_{\text{ch4}}^* = \dot{m}_{\text{ch1}}^* + \dot{m}_{\text{fl}}^* \quad (\text{A.4})$$

The  $\lambda$  signal in Receiver 4 indicates the amount of excess air in Receiver 4:

$$\lambda_{\text{rec4}} = \frac{\dot{m}_{14}^* + \dot{m}_{\text{air}}^*}{\dot{m}_{\text{fl}}^* (A/F)_s} \quad (\text{A.5})$$

Similarly to Eq. (A.2), Eqs. (A.3) and (A.5) lead to:

$$\dot{m}_{\text{ch4}}^* = \dot{m}_{\text{fl}}^* (1 + (A/F)_s \lambda_{\text{rec4}}) \quad (\text{A.6})$$

**Scavenging mass flow ( $\dot{m}_{14}^*$ ):** The air entering the charger through Channel 1 which is not leaving through Channel 2, but through Channel 4, can also be considered as the difference of  $\dot{m}_{\text{ch4}}^*$  and  $\dot{m}_{\text{eg}}^*$ . Based on the assumptions that

- mass flows are quasi steady-state,
- EGR rates are small,  $x_{\text{egr}} \ll 1$

the scavenging mass flow then may be calculated using the  $\lambda$  signals  $\lambda_{\text{em}}$  and  $\lambda_{\text{rec4}}$  and the fuel mass flow:

$$\begin{aligned} \dot{m}_{14}^* &= \dot{m}_{\text{ch1}}^* - \dot{m}_{12}^* \\ &= \dot{m}_{\text{ch4}}^* - \dot{m}_{\text{eg}}^* \\ &= \dot{m}_{\text{fl}}^* (1 + (A/F)_s \lambda_{\text{rec4}}) - \dot{m}_{\text{fl}}^* (1 + (A/F)_s \lambda_{\text{em}}) \\ &= \dot{m}_{\text{fl}}^* (A/F)_s (\lambda_{\text{rec4}} - \lambda_{\text{em}}) \end{aligned} \quad (\text{A.7})$$

**Scavenging rate ( $x_{\text{sc}}$ ):** For steady-state conditions and for small EGR rates the mass flow  $\dot{m}_{12}^*$  may be approximated by  $\dot{m}_{\text{ch2}}^*$  (see Fig. 1.5). The scavenging rate  $x_{\text{sc}}$  then may be calculated from just

these two air-to-fuel ratios:

$$\begin{aligned}
 x_{\text{sc}} &:= \frac{\dot{m}_{14}^*}{\dot{m}_{\text{ch}2}^*} \approx \frac{\dot{m}_{14}^*}{\dot{m}_{12}^*} \\
 &= \frac{\dot{m}_{\text{fl}}^* (A/F)_s (\lambda_{\text{rec}4} - \lambda_{\text{em}})}{\dot{m}_{\text{fl}}^* (A/F)_s \lambda_{\text{em}}} \\
 &= \frac{\lambda_{\text{rec}4} - \lambda_{\text{em}}}{\lambda_{\text{em}}}
 \end{aligned} \tag{A.8}$$

With respect to the time delay of the measurement signal of  $\lambda_{\text{rec}4}$ , a better estimation of the scavenging rate  $x_{\text{sc}}$  may be obtained using an air mass flow meter to measure  $\dot{m}_{\text{ch}1}^*$  and to approximate  $\dot{m}_{\text{ch}2}^*$  by the mass flow  $\dot{m}_{\text{im}}^*$  that is aspirated by the engine. The scavenging rate then is calculated using the following relation:

$$\begin{aligned}
 x_{\text{sc}} &:= \frac{\dot{m}_{14}^*}{\dot{m}_{\text{ch}2}^*} = \frac{\dot{m}_{\text{ch}1}^* - \dot{m}_{12}^*}{\dot{m}_{\text{ch}2}^*} \\
 &\approx \frac{\dot{m}_{\text{ch}1}^* - \dot{m}_{\text{ch}2}^*}{\dot{m}_{\text{ch}2}^*} \\
 &\approx \frac{\dot{m}_{\text{ch}1}^* - \dot{m}_{\text{im}}^*}{\dot{m}_{\text{im}}^*}
 \end{aligned} \tag{A.9}$$

**Compressed air mass flow ( $\dot{m}_{12}^*$ ):** For steady-state operating conditions,  $\dot{m}_{12}^*$  is equivalent to  $\dot{m}_{\text{air}}^*$ .

$$\dot{m}_{12}^* \equiv \dot{m}_{\text{air}}^* \tag{A.10}$$

**Exhaust gas recirculation rate ( $x_{\text{egr}}$ ):** The EGR rate  $x_{\text{egr}}$  is defined as the mass fraction of recirculated exhaust gas mass flow ( $\dot{m}_{32}^*$ ) to the total mass flow through Channel 2 ( $\dot{m}_{\text{ch}2}^*$ ). In other words, the EGR rate designates the exhaust gas *mass* fraction in Channel 2. Carbon dioxide  $\text{CO}_2$ , carbon monoxide  $\text{CO}$ , and hydrocarbons  $\text{HC}$  are used as tracer species to measure the exhaust gas mass flow from Channel 3 to Channel 2. The fraction  $x_{\text{C}}$  is defined as the sum of all fractions of

carbon species.

$$x_C := \frac{n_{\text{CO}_2} + n_{\text{CO}} + n_{\text{HC}}}{n_{\text{tot}}} = x_{\text{CO}_2} + x_{\text{CO}} + x_{\text{HC}} \quad (\text{A.11})$$

The molar fractions  $x_{\text{C,rec2}}$  and  $x_{\text{C,rec3}}$  set the number of carbon particles ( $n_C$ ) in relation to the total number of particles in the probes of Receiver 2 and Receiver 3.

$$\begin{aligned} x_{\text{C,rec2}} &= \frac{n_{\text{CO}_2,\text{rec2}}}{n_{\text{tot,rec2}}} \\ x_{\text{C,rec3}} &= \frac{n_{\text{CO}_2,\text{rec3}}}{n_{\text{tot,rec3}}} \end{aligned} \quad (\text{A.12})$$

Since the probes are dehumidified before they are inserted into the analyzer, the measured concentration  $c_C$  is the number of particles divided by the total number of particles, except water.

$$\begin{aligned} c_{\text{C,rec2}} &= \frac{n_{\text{C,rec2}}}{n_{\text{tot,rec2}} - n_{\text{H}_2\text{O,rec2}}} = \frac{x_{\text{C,rec2}}}{1 - x_{\text{H}_2\text{O,rec2}}} \\ c_{\text{C,rec3}} &= \frac{n_{\text{C,rec3}}}{n_{\text{tot,rec3}} - n_{\text{H}_2\text{O,rec3}}} = \frac{x_{\text{C,rec3}}}{1 - x_{\text{H}_2\text{O,rec3}}} \end{aligned} \quad (\text{A.13})$$

It is assumed that the molar fractions in the exhaust gas remain constant as they pass the charger from Receiver 3 to Receiver 2. The molar fractions for carbons and water in Receiver 2 and Receiver 3 thus are related as follows:

$$x_{\text{H}_2\text{O,rec3}} = \frac{x_{\text{H}_2\text{O,rec2}}}{1 - x_{\text{air,rec2}}} \quad (\text{A.14})$$

and

$$x_{\text{C,rec3}} = \frac{x_{\text{C,rec2}}}{1 - x_{\text{air,rec2}}} \quad (\text{A.15})$$

where  $x_{\text{air,rec2}}$  is the molar fraction of the (dry) air in Receiver 2. Inserting Eqs. (A.14) and (A.15) into Eqs. (A.13) and defining the *molar* EGR rate  $x_{\text{egr,mol}}$  as follows:

$$x_{\text{egr,mol}} := 1 - x_{\text{air,rec2}} \quad (\text{A.16})$$

The molar EGR rate results as follows:

$$x_{\text{egr,mol}} = \frac{c_{\text{Crec2}}/c_{\text{Crec3}}}{1 - x_{\text{H}_2\text{O,rec3}} (1 - c_{\text{Crec2}}/c_{\text{Crec3}})} \quad (\text{A.17})$$



The exhaust gas mass fraction  $x_{\text{egr}}$  follows from the molar fraction  $x_{\text{egr,mol}}$ , taking into account the molar masses of exhaust gas ( $M_{\text{eg}}$ ) and of the exhaust gas/air mixture in Receiver 2 ( $M_{\text{rec2}}$ ).

$$x_{\text{egr}} = \frac{m_{\text{eg,rec2}}^*}{m_{\text{tot,rec2}}^*} = \frac{n_{\text{eg}} M_{\text{eg}}}{n_{\text{tot,rec2}} M_{\text{rec2}}} = x_{\text{egr,mol}} \frac{M_{\text{eg}}}{M_{\text{rec2}}} \quad (\text{A.18})$$

The molar mass of the fluid in Receiver 2 is again a function of the molar EGR rate:

$$\begin{aligned} M_{\text{rec2}} &= \frac{n_{\text{eg}} M_{\text{eg}} + n_{\text{air}} M_{\text{air}}}{n_{\text{tot,rec2}}} = \\ &= \frac{n_{\text{eg}}}{n_{\text{tot,rec2}}} M_{\text{eg}} + \frac{n_{\text{tot,rec2}} - n_{\text{eg}}}{n_{\text{tot,rec2}}} M_{\text{air}} = \\ &= x_{\text{egr,mol}} M_{\text{eg}} + (1 - x_{\text{egr,mol}}) M_{\text{air}} \end{aligned} \quad (\text{A.19})$$

Hence, the EGR rate is:

$$x_{\text{egr}} = \frac{x_{\text{egr,mol}} M_{\text{eg}}}{x_{\text{egr,mol}} M_{\text{eg}} + (1 - x_{\text{egr,mol}}) M_{\text{air}}} \quad (\text{A.20})$$

The molar mass for exhaust gas ( $M_{\text{eg}}$ ) and the molar fraction for water in the exhaust gas ( $x_{\text{H}_2\text{O}}$ ) are subject to the pressure  $p_{\text{rec3}}$ , the temperature  $T_{\text{rec3}}$ , and the air-to-fuel ratio  $\lambda_{\text{em}}$ . They were calculated using the *CHEMICAL EQUILIBRIUM PROGRAMMING PACKAGE (CHEPP)* presented in (Eriksson, 2004):

$$[M_{\text{eg}}, x_{\text{H}_2\text{O}}] = f(p_{\text{rec3}}, T_{\text{rec3}}, \lambda_{\text{em}}) \quad (\text{A.21})$$

**Recirculated exhaust gas mass flow:** With the EGR rate  $x_{\text{egr}}$ , the recirculated mass flow  $m_{32}^*$  can be calculated using the definition of the EGR rate

$$x_{\text{egr}} := \frac{m_{32}^*}{m_{\text{ch2}}^*} \quad (\text{A.22})$$

Since the mass flow in Channel 2 is

$$m_{\text{ch2}}^* = m_{12}^* + m_{32}^* \quad (\text{A.23})$$

the EGR mass flow may be written as

$$m_{32}^* = \frac{x_{\text{egr}}}{1 - x_{\text{egr}}} m_{12}^* \quad (\text{A.24})$$

or, for steady-state operating conditions:

$$m_{\text{egr}}^* \equiv m_{32}^* = \frac{x_{\text{egr}}}{1 - x_{\text{egr}}} m_{\text{air}}^* = \frac{x_{\text{egr}}}{1 - x_{\text{egr}}} m_{\text{fl}}^* \lambda_{\text{em}}(A/F)_s \quad (\text{A.25})$$

**Mass flows through Channel 3 and gas pocket ( $m_{\text{ch3}}^*$ ,  $m_{\text{chg}}^*$ ,  $m_{\text{ch3chg}}^*$ ):** The mass flow  $m_{\text{ch3}}^*$  is distinct for a closed gas pocket valve.

$$y_{\text{gpv}} = 1 \quad \Rightarrow \quad \begin{cases} m_{\text{chg}}^* = 1 \\ m_{\text{ch3}}^* = m_{\text{ch3chg}}^* = m_{\text{eg}}^* \end{cases} \quad (\text{A.26})$$

For partially opened gas pocket valve positions, some part of  $m_{\text{ch3chg}}^*$  is flowing through the gas pocket valve (GPV). The GPV mass flow  $m_{\text{gpv}}^*$  generally is a function of up- and downstream pressure, valve position, geometry, and secondary effects. The GPV may be modeled as flow restriction for compressible fluid (Sect. 2.2).

$$y_{\text{gpv}} < 1 \quad \Rightarrow \quad m_{\text{chg}}^* = f(p_{\text{rec3}}, T_{\text{rec3}}, p_{\text{gp}}, y_{\text{gpv}}, A_{\text{gpv}}, \dots) \quad (\text{A.27})$$

The mass flow  $m_{\text{chg}}^*$  entering the cell wheel through the gas pocket channel may be approximated by  $m_{\text{gpv}}^*$ , since the gas pocket volume is very small and its dynamics may be neglected.

$$m_{\text{chg}}^* \approx m_{\text{gpv}}^* \quad (\text{A.28})$$



## Appendix B

# Derivation of the Euler Equations

The law of the **conservation of mass** states that the change in total mass in a control volume of length  $[x_a, x_b]$  and with the cross-section  $A$  (see Fig. B.1) during a time interval  $[t_1, t_2]$  is equal to the net mass passing through the boundaries of the control volume in the same time interval:

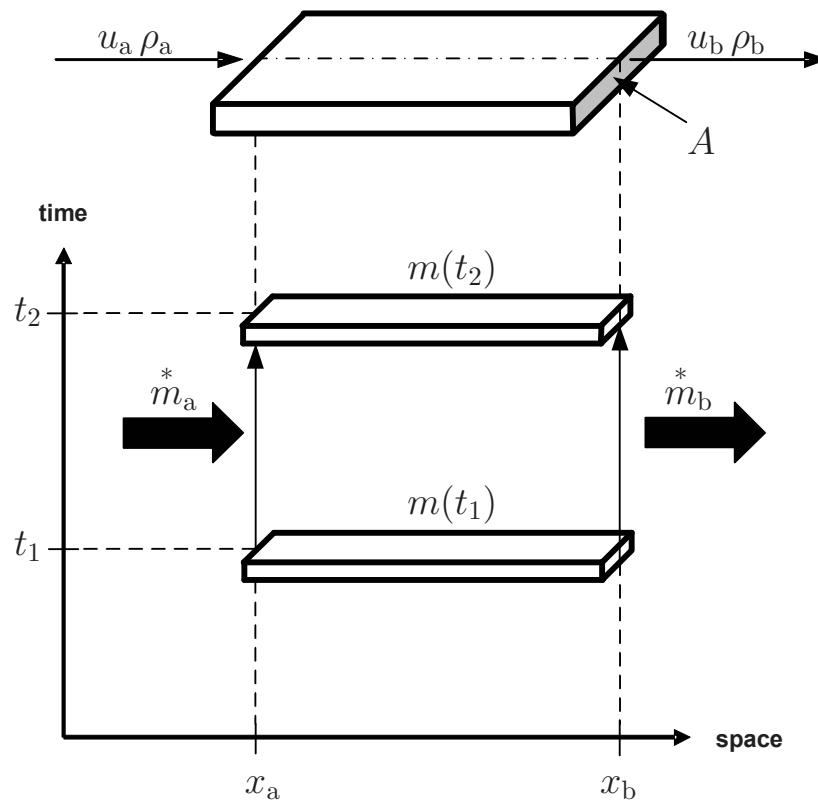


**Figure B.1:** Mass balance over a control volume and over a certain time interval

$$m(t_2) - m(t_1) = \dot{m}_a^* \cdot (t_2 - t_1) - \dot{m}_b^* \cdot (t_2 - t_1) \quad (\text{B.1})$$

or rather

$$\begin{aligned} \rho(t_2) \cdot (x_b - x_a) \cdot A - \rho(t_1) \cdot (x_b - x_a) \cdot A &= \dots \\ \rho_a \cdot u_a \cdot A \cdot (t_2 - t_1) - \rho_b \cdot u_b \cdot A \cdot (t_2 - t_1) \end{aligned} \quad (\text{B.2})$$

If both sides are divided by the surface  $A$ , this equation also can be written in the integral form:

$$\int_{x_a}^{x_b} \rho(t_2) - \rho(t_1) \, dx = - \int_{t_1}^{t_2} \rho_b \cdot u_b - \rho_a \cdot u_a \, dt \quad (\text{B.3})$$

or

$$\int_{x_a}^{x_b} \int_{t_1}^{t_2} \frac{\partial \rho}{\partial t} \, dt \, dx = - \int_{t_1}^{t_2} \int_{x_a}^{x_b} \frac{\partial(\rho \cdot u)}{\partial x} \, dx \, dt \quad (\text{B.4})$$

or, more simply

$$\frac{\partial \rho}{\partial t} + \frac{\partial(\rho \cdot u)}{\partial x} = 0 \quad (\text{B.5})$$

The law of the **conservation of momentum** similarly states that the change in total momentum in  $[x_a, x_b]$  in the time interval  $[t_1, t_2]$  is equal to the net momentum flow through the boundaries of  $[x_a, x_b]$  plus the net momentum change due to the pressure on the boundaries of  $[x_a, x_b]$ :

Total momentum in  $[x_a, x_b]$  at  $t_1$  and  $t_2$ :

$$\begin{aligned} M(t_1) &= \rho(t_1) \cdot u(t_1) \cdot A \cdot (x_b - x_a) \\ M(t_2) &= \rho(t_2) \cdot u(t_2) \cdot A \cdot (x_b - x_a) \end{aligned} \quad (\text{B.6})$$

Momentum flow through boundaries at  $x_a$  and  $x_b$ :

$$\begin{aligned} \dot{M}_a^* &= \rho_a u_a^2 A \\ \dot{M}_b^* &= \rho_b u_b^2 A \end{aligned} \quad (\text{B.7})$$

Momentum change due to the pressure on the boundaries at  $x_a$  and  $x_b$ :

$$\begin{aligned} \dot{M}_a^* &= p_a A \\ \dot{M}_b^* &= p_b A \end{aligned} \quad (\text{B.8})$$

Hence, the conservation of momentum reads as follows:

$$\begin{aligned} & [\rho(t_2) \cdot u(t_2) - \rho(t_1) \cdot u(t_1)] \cdot (x_b - x_a) \cdot A = \\ & (\rho_a u_a^2 - \rho_b u_b^2) \cdot A \cdot (t_2 - t_1) + \\ & (p_a - p_b) \cdot A \cdot (t_2 - t_1) \end{aligned} \quad (\text{B.9})$$

Rewritten in the conservation form (B.9) becomes:

$$\frac{\partial(\rho \cdot u)}{\partial t} + \frac{\partial(\rho \cdot u^2)}{\partial x} + \frac{\partial p}{\partial x} = 0 \quad (\text{B.10})$$

The law of the **conservation of energy** is stated in terms of the *specific total energy per unit mass*  $e_T$  (internal energy plus specific kinetic energy): The change in total energy in  $[x_a, x_b]$  in the time interval  $[t_1, t_2]$  is equal to the net energy flow through the boundaries of  $[x_a, x_b]$  plus the net energy change due to the pressure on the boundaries of  $[x_a, x_b]$  in the time interval  $[t_1, t_2]$  (see Fig. B.1): Total energy in the control volume  $[x_a, x_b]$  (cross-section  $A$ ) at  $t_1$  and  $t_2$ :

$$\begin{aligned} E(t_1) &= \rho(t_1) \cdot e_T(t_1) \cdot A \cdot (x_b - x_a) \\ E(t_2) &= \rho(t_2) \cdot e_T(t_2) \cdot A \cdot (x_b - x_a) \end{aligned} \quad (\text{B.11})$$

Energy flow through boundaries at  $x_a$  and  $x_b$ :

$$\begin{aligned} \dot{E}_a^* &= \rho_a u_a e_{T,a} A \\ \dot{E}_b^* &= \rho_b u_b e_{T,b} A \end{aligned} \quad (\text{B.12})$$

Energy change due to pressure on boundaries at  $x_a$  and  $x_b$ :

$$\begin{aligned} \dot{E}_a^* &= p_a u_a A \\ \dot{E}_b^* &= p_b u_b A \end{aligned} \quad (\text{B.13})$$

Hence, the conservation of energy reads as follows:

$$\begin{aligned} & [\rho(t_2) \cdot e_T(t_2) - \rho(t_1) \cdot e_T(t_1)] \cdot (x_b - x_a) \cdot A = \\ & (\rho_a u_a e_{T,a} - \rho_b u_b e_{T,b}) \cdot A \cdot (t_2 - t_1) + \\ & (p_a u_a - p_b u_b) \cdot A \cdot (t_2 - t_1) \end{aligned} \quad (\text{B.14})$$

Rewritten in the conservation form (B.14) becomes:

$$\frac{\partial(\rho \cdot e_T)}{\partial t} + \frac{\partial(\rho \cdot u \cdot e_T)}{\partial x} + \frac{\partial(p \cdot u)}{\partial x} = 0 \quad (\text{B.15})$$



## Appendix C

# Basic Equations of the Linear Wave Theory

The data on the gas dynamics used in this model are modeled on the basis of the linear wave theory, where the characteristics (i.e. shock position over time) are represented by straight lines (Sauer, 1960). Assuming a perfect gas behavior, the basic relations for the linear, one-dimensional gas dynamics again follow from mass, energy, and impulse balances (see also Appendix B). The relations are formulated for a narrow adiabatic pipe (Fig. C.1). Assuming a frame of reference that is moving with the speed of the shock, the unsteady shock propagation thus becomes a *steady-state* problem.

The shock is propagating through zone  $z_0$  where the state of the fluid is known:  $u_{z0}$ ,  $p_{z0}$ ,  $T_{z0}$ ,  $\rho_{z0}$ . Behind the shock, the pressure  $p_{z1}$  is the only known state. Fluid velocity  $u_{z1}$ , temperature  $T_{z1}$ , density  $\rho_{z1}$ , together with the shock velocity  $u_{ws}$ , are to be calculated using the equations that will be derived in this chapter.

### Governing equations

Moving the inertial system along the shock, the unsteady process is transformed into a steady-state problem.

**Transformation:** The fluid states in front and behind the shock are transformed from the fixed system to the moving system:

$$\begin{aligned} u_a &= u_{z1} - u_{ws} < 0, & u_b &= u_{z0} - u_{ws} < 0 \\ p_a &= p_{z1}, & p_b &= p_{z0} < p_{z1} \\ T_a &= T_{z1}, & T_b &= T_{z0} < T_{z1} \\ \rho_a &= \rho_{z1}, & \rho_b &= \rho_{z0} < \rho_{z1} \end{aligned} \tag{C.1}$$

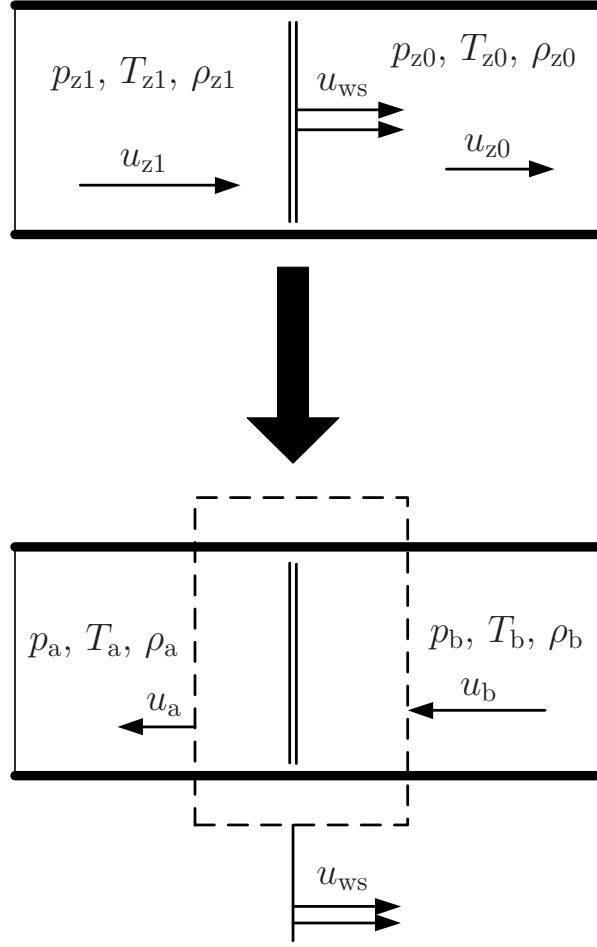


**Figure C.1:** One-dimensional shock wave propagation in a narrow pipe. The frame of reference is moving with the same speed as the shock. The unsteady shock propagation thus becomes a steady-state problem.

**Ideal gas law:** As mentioned earlier, the ideal gas law connects pressure, temperature, and density for a perfect gas.

$$\begin{aligned} p_a &= \rho_a R T_a \\ p_b &= \rho_b R T_b \end{aligned} \tag{C.2}$$

**Conservation of mass:** Unlike indicated by Eq. (B.2), no mass is stored in the control volume. Mass inflow and outflow through cross-section  $A$  are balanced.

$$\rho_a u_a A = \rho_b u_b A \tag{C.3}$$

**Conservation of momentum:** No momentum is stored in the control volume. Momentum inflow and outflow plus momentum changes due to pressure on boundaries are balanced.

$$\rho_a u_a^2 A + p_a A = \rho_b u_b^2 A + p_b A \quad (\text{C.4})$$

**Conservation of energy:** No energy is stored in the control volume. Energy inflow and outflow plus energy changes due to pressure on boundaries are balanced.

$$\rho_a u_a e_{T,a} A + p_a u_a A = \rho_b u_b e_{T,b} A + p_b u_b A \quad (\text{C.5})$$

The specific total energy  $e_T$  combines the internal energy per mass  $e$ , i.e. the microscopic movement of the molecules, plus the macroscopic movement of the fluid.

$$e_T = e + \frac{u^2}{2} = c_v T + \frac{u^2}{2} \quad (\text{C.6})$$

The specific total enthalpy  $h_T$  additionally considers the potential energy per mass, i.e. the pressure on the boundaries.

$$h_T = e + \frac{p}{\rho} + \frac{u^2}{2} = c_p T + \frac{u^2}{2} \quad (\text{C.7})$$

Hence, Eq. (C.5) can be written as

$$\rho_a u_a A \left( c_v T_a + \frac{u_a^2}{2} + \frac{p_a}{\rho_a} \right) = \rho_b u_b A \left( c_v T_b + \frac{u_b^2}{2} + \frac{p_b}{\rho_b} \right) \quad (\text{C.8})$$

or

$$\rho_a u_a A \left( c_p T_a + \frac{u_a^2}{2} \right) = \rho_b u_b A \left( c_p T_b + \frac{u_b^2}{2} \right) \quad (\text{C.9})$$

or, replacing  $T$  by Eq. (C.2):

$$\rho_a u_a A \left( \frac{c_p}{R} \frac{p_a}{\rho_a} + \frac{u_a^2}{2} \right) = \rho_b u_b A \left( \frac{c_p}{R} \frac{p_b}{\rho_b} + \frac{u_b^2}{2} \right) \quad (\text{C.10})$$

## Derivation of the Shock Equations

The governing equations (C.3), (C.4), and (C.10) may be simplified and summarized as

$$\begin{aligned}\rho_a u_a &= \rho_b u_b \\ \rho_a u_a^2 + p_a &= \rho_b u_b^2 + p_b \\ \frac{c_p p_a}{R \rho_a} + \frac{u_a^2}{2} &= \frac{c_p p_b}{R \rho_b} + \frac{u_b^2}{2}\end{aligned}\tag{C.11}$$

Eliminating  $\rho_a$  by using Eq. (C.3) yields:

$$\rho_b u_b u_a + p_a = \rho_b u_b^2 + p_b\tag{C.12}$$

$$\frac{c_p p_a u_a}{R \rho_b u_b} + \frac{u_a^2}{2} = \frac{c_p p_b}{R \rho_b} + \frac{u_b^2}{2}\tag{C.13}$$

Eliminating  $u_a$  yields:

$$\frac{c_p p_a}{R \rho_b} \left( \frac{p_b - p_a}{\rho_b u_b^2} + 1 \right) + \frac{1}{2} \left( \frac{p_b - p_a}{\rho_b u_b} + u_b \right)^2 = \frac{c_p p_b}{R \rho_b} + \frac{u_b^2}{2}\tag{C.14}$$

Isolating  $u_b$  yields:

$$\begin{aligned}u_b^2 &= \frac{p_a}{\rho_b} \left( \frac{2c_p - R}{2c_p - 2R} \right) + \frac{p_b}{\rho_b} \left( \frac{R}{2c_p - 2R} \right) = \\ &= \frac{p_a}{\rho_b} \frac{1}{2} \left( \frac{R}{c_p - R} + \frac{2c_p - 2R}{c_p - R} \right) + \frac{p_b}{\rho_b} \frac{1}{2} \left( \frac{R}{c_p - R} \right)\end{aligned}\tag{C.15}$$

Considering the relations between the ratio of specific heats  $\kappa$ , specific gas constant  $R$ , and the specific heats  $c_p$  and  $c_v$  yields:

$$\begin{aligned}\kappa &:= \frac{c_p}{c_v} \equiv \frac{c_p}{c_p - R} \\ \rightarrow \kappa - 1 &= \frac{R}{c_p - R}\end{aligned}\tag{C.16}$$

Eq. (C.15) can be written as:

$$\begin{aligned}u_b^2 &= \frac{p_a}{\rho_b} \left( \frac{\kappa + 1}{2} \right) + \frac{p_b}{\rho_b} \left( \frac{\kappa - 1}{2} \right) = \\ &= \frac{p_b}{2\rho_b} \left( \frac{p_a}{p_b} (\kappa + 1) + \kappa - 1 \right)\end{aligned}\tag{C.17}$$



Substituting the **pressure ratio** over the shock by

$$\pi_s := \frac{p_a}{p_b} \equiv \frac{p_{z1}}{p_{z0}} > 1 \quad (\text{C.18})$$

the fluid velocity over boundary  $b$  ( $u_b$ ) can be isolated as follows:

$$u_b = \pm \sqrt{\frac{p_b}{2\rho_b}} \sqrt{\pi_s (\kappa + 1) + \kappa - 1} \quad (\text{C.19})$$

Assuming that  $u_b < 0$  and using the transformation of Eq. (C.1), , the **shock velocity**  $u_{ws}$  relative to a fixed coordinate system may be written as follows:

$$\begin{aligned} u_{ws} &= u_{z0} - u_b = \\ &= u_{z0} + \sqrt{\frac{p_b}{2\rho_b}} \sqrt{\pi_s (\kappa + 1) + \kappa - 1} = \\ &= u_{z0} + \sqrt{\frac{RT_{z0}}{2}} \sqrt{\pi_s (\kappa + 1) + \kappa - 1} \end{aligned} \quad (\text{C.20})$$

Note that for weak disturbances, the shock velocity may be approximated by the speed of sound. Relative to a stagnant fluid the **speed of sound** is (see also Chapter D):

$$a := \sqrt{\kappa RT} \quad (\text{C.21})$$

For  $\pi_s \approx 1$  (weak disturbance), the relative shock wave velocity becomes:

$$\begin{aligned} u_{ws} &= \sqrt{\frac{RT}{2}} \sqrt{o(1) (\kappa + 1) + \kappa - 1} \\ &\approx \sqrt{\frac{RT}{2}} \sqrt{2\kappa} = \sqrt{RT\kappa} = a \end{aligned} \quad (\text{C.22})$$

The relation for the **fluid acceleration** over the shock wave

$$\Delta u_s := u_{z1} - u_{z0} = (u_a + u_{ws}) - (u_b + u_{ws}) = u_a - u_b \quad (\text{C.23})$$

can be derived by isolating  $u_a$  from Eq. (C.12) and using:

$$u_a = \frac{p_b - p_a}{\rho_b u_b} + u_b = \left( \frac{p_b}{p_b} - \frac{p_a}{p_b} \right) \frac{p_b}{\rho_b u_b} + u_b = (1 - \pi_s) \frac{p_b}{\rho_b u_b} + u_b \quad (\text{C.24})$$

Hence,

$$\Delta u_s = (1 - \pi_s) \frac{p_b}{\rho_b u_b} \quad (\text{C.25})$$

Presuming that  $\Delta u_s > 0$  and inserting  $u_b$  from Eq. (C.19) we obtain:

$$\begin{aligned} \Delta u_s &= (\pi_s - 1) \frac{p_b}{\rho_b} \frac{1}{\sqrt{\frac{p_b}{2\rho_b}} \sqrt{\pi_s(\kappa + 1) + \kappa - 1}} = \\ &= \sqrt{\frac{2p_b}{\rho_b}} \frac{\pi_s - 1}{\sqrt{\pi_s(\kappa + 1) + \kappa - 1}} = \\ &= \sqrt{2RT_b} \frac{\pi_s - 1}{\sqrt{\pi_s(\kappa + 1) + \kappa - 1}} \end{aligned} \quad (\text{C.26})$$

Hence, the **fluid velocity** behind the shock wave ( $u_{z1}$ ) can be written as:

$$u_{z1} = u_{z0} + \sqrt{2RT_{z0}} \frac{\pi_s - 1}{\sqrt{\pi_s(\kappa + 1) + \kappa - 1}} \quad (\text{C.27})$$

The density and temperature ratios over the shock wave follow from mass the balance equation (C.3), and from Equations (C.19) and (C.25).

$$\begin{aligned} \frac{\rho_b}{\rho_a} &= \frac{u_a}{u_b} = \frac{u_b - \Delta u_s}{u_b} = \frac{u_b - \Delta u_s}{u_b} = 1 - \frac{\Delta u_s}{u_b} = \\ &= 1 - \frac{\sqrt{\frac{2p_b}{\rho_b}} \frac{\pi_s - 1}{\sqrt{\pi_s(\kappa + 1) + \kappa - 1}}}{\sqrt{\frac{p_b}{2\rho_b}} \sqrt{\pi_s(\kappa + 1) + \kappa - 1}} = \\ &= 1 - \frac{2(\pi_s - 1)}{\pi_s(\kappa + 1) + \kappa - 1} = \\ &= \frac{[\pi_s(\kappa + 1) + \kappa - 1] - 2(\pi_s - 1)}{[\pi_s(\kappa + 1) + \kappa - 1]} = \\ &= \frac{\pi_s(\kappa - 1) + \kappa + 1}{\pi_s(\kappa + 1) + \kappa - 1} \end{aligned} \quad (\text{C.28})$$

Hence, with

$$\rho_{z0} \equiv \rho_b \quad \text{and} \quad \rho_{z1} \equiv \rho_a \quad (\text{C.29})$$

the **density** in zone  $z_1$  follows as

$$\rho_{z1} = \rho_{z0} \frac{\pi_s(\kappa + 1) + \kappa - 1}{\pi_s(\kappa - 1) + \kappa + 1} \quad (\text{C.30})$$

Since

$$\frac{\rho_a}{\rho_b} = \frac{\frac{p_a}{RT_a}}{\frac{p_b}{RT_b}} = \frac{p_a}{p_b} \frac{T_b}{T_a} = \pi_s \frac{T_b}{T_a} \quad (\text{C.31})$$

and

$$T_{z0} \equiv T_b \quad \text{and} \quad T_{z1} \equiv T_a \quad (\text{C.32})$$

the **temperature** in zone  $z_1$  follows as:

$$T_{z1} = T_{z0} \pi_s \frac{\pi_s(\kappa - 1) + \kappa + 1}{\pi_s(\kappa + 1) + \kappa - 1} \quad (\text{C.33})$$

The basic equations of the linear wave theory, indexed with  $z_0$  for the **uncompressed** fluid in front of the shock wave, and with  $z_1$  for the **compressed** fluid behind the shock wave are summarized in the following listing:

- Pressure ratio over the shock wave  $s$ :

$$\pi_s = \frac{p_{z1}}{p_{z0}}$$

- Sound velocity in the fluid in front of the shock wave:

$$a_{z0} = \sqrt{\kappa R T_{z0}} = \sqrt{\kappa \frac{p_{z0}}{\rho_{z0}}}$$

- Shock velocity, relative to a fixed coordinate system:

$$u_{ws} = u_{z0} + \sqrt{\frac{RT_{z0}}{2}} \sqrt{\pi_s(\kappa + 1) + \kappa - 1}$$

- Fluid velocity behind the shock wave:

$$u_{z1} = u_{z0} + \sqrt{2RT_{z0}} \frac{\pi_s - 1}{\sqrt{\pi_s(\kappa + 1) + \kappa - 1}}$$

- Density behind the shock wave:

$$\rho_{z1} = \rho_{z0} \pi_s \frac{\pi_s(\kappa + 1) + \kappa - 1}{\pi_s(\kappa - 1) + \kappa + 1}$$

- Temperature behind the shock wave:

$$T_{z1} = T_{z0} \pi_s \frac{\pi_s(\kappa - 1) + \kappa + 1}{\pi_s(\kappa + 1) + \kappa - 1}$$

## Appendix D

# The Speed of Sound

The speed of sound is the speed at which small disturbances propagate through a substance measured with respect to the movement of the substance. The state change over the disturbance may be described by the second law of thermodynamics for a closed system,

$$T ds = dh - v dp \quad (\text{D.1})$$

where the enthalpy  $h$  includes the microscopic movement of the molecules and the potential energy

$$h = c_p T + \frac{p}{\rho} \quad (\text{D.2})$$

and  $v$  designates the specific volume:

$$v = \frac{1}{\rho} = \frac{R T}{p} \quad (\text{D.3})$$

Equation (D.1) then may be written as:

$$ds = \frac{1}{T} (dh - v dp) = \frac{1}{T} \left( c_p dT - \frac{R T}{p} dp \right) = c_p \frac{dT}{T} - R \frac{dp}{p} \quad (\text{D.4})$$

The total derivative of the gas law

$$p = \rho R T \quad (\text{D.5})$$

follows as

$$dp = d\rho R T + \rho R dT \quad (\text{D.6})$$

Division by  $\rho RT$  (or  $p$ ) yields:

$$\frac{dp}{p} = \frac{d\rho}{\rho} + \frac{dT}{T} \quad (\text{D.7})$$

Equation (D.7) inserted in Eq. (D.4) thus becomes:

$$\begin{aligned} ds &= c_p \left( \frac{dp}{p} - \frac{d\rho}{\rho} \right) - R \frac{dp}{p} = \\ &= \frac{dp}{p} (c_p - R) - c_p \frac{d\rho}{\rho} = \\ &= \frac{dp}{p} c_v - c_p \frac{d\rho}{\rho} \end{aligned} \quad (\text{D.8})$$

For small disturbances, the process may be assumed to be isentropic ( $ds = 0$ ). Equation (D.8) may then be rewritten as:

$$\begin{aligned} \frac{dp}{p} c_v &= c_p \frac{d\rho}{\rho} \\ \frac{dp}{p} &= \frac{c_p}{c_v} \frac{d\rho}{\rho} \\ \frac{dp}{p} &= \kappa \frac{d\rho}{\rho} \\ \frac{dp}{d\rho} &= \kappa \frac{p}{\rho} \end{aligned} \quad (\text{D.9})$$

The fraction  $dp/d\rho$  relates the pressure change to the density change. Its unit is  $[\text{m}^2/\text{s}^2]$ . It may be interpreted as the square of the propagation speed of the disturbance. The speed of sound  $a$  is therefore defined as:

$$a^2 := \frac{dp}{d\rho} = \kappa \frac{p}{\rho} = \kappa R T \quad (\text{D.10})$$

# Bibliography

- Akbari**, P., Nalim, R., and Müller, N. (2004). A Review of Wave Rotor Technology and its Applications. *2004 ASME International Mechanical Engineering Conference, Anaheim, CA, ASME Paper IMECE2004-60082*.
- Amstutz**, A. (1991). *Geregelte Abgasrückführung zur Senkung der Stickoxid- und Partikelemissionen beim Dieselmotor mit COMPREX-Aufladung*. Diss. ETH No. 9421, ETH Zürich.
- Baehr**, H. (1992). *Thermodynamik*. 8. Auflage, Springer Verlag.
- Berchtold**, M. (1959). The COMPREX Diesel Supercharger. *SAE Transaction, Vol. 67 (1959), pp. 5-13*.
- Berchtold**, M. (1961). Druckwellenaufladung für kleine Fahrzeug-Dieselmotoren. *Schweizerische Bauzeitung 79, No. 46, pp. 801-808*.
- Berchtold**, M. and Gardiner, F. (1958). The COMPREX: A New Concept of Diesel Supercharging. *ASME Paper 58-GTP-16*.
- Berchtold**, M. and Gull, H. (1960). Road Performance of a COMPREX Supercharged Diesel Truck. *SAE Transactions, Vol. 68 (1960), pp. 367-378*.
- Boris**, J. and Book, D. (1973). Flux-Corrected Transport. *Journal of Computational Physics 11, pp. 38-69*.
- Brand**, D. (2005). *Control-Oriented Modeling of NO Emissions of SI Engines*. Diss. ETH No. 16037, ETH Zürich.
- Cortona**, E. (2000). *Engine Thermomanagement for Fuel Consumption Reduction*. Diss. ETH No. 13862, ETH Zürich.

- Croes, N.** (1979). Die Wirkungsweise der Taschen des Druckwellenladers COMPREX. *MTZ Motortechnische Zeitschrift*, Vol. 40, No. 2, pp. 91-97.
- Doerfler, P.** (1975). COMPREX Supercharging of Vehicle Diesel Engines. *SAE Paper 750335*.
- Endres, H.** (1985). COMPREX<sup>®</sup>-Aufladung schnelllaufender direkteinspritzender PKW-Dieselmotoren. Diss. der Technischen Hochschule Aachen, Deutschland.
- Eriksson, L.** (2002). Mean Value Models for Exhaust Temperatures. *SAE Technical Paper, 2002-01-0374*.
- Eriksson, L.** (2004). Chepp – a CHemical Equilibrium Program Package for Matlab. *SAE Technical Paper, 2004-01-1460*.
- Eriksson, L., Nielsen, L., Brugard, J., Bergström, J., Pettersson, F., and Andersson, P.** (2001). Modeling and Simulation of a Turbocharged SI Engine. *3rd IFAC Workshop, "Advances in Automotive Control", 2001, pp. 379ff.*
- Fraokowiak, M., Iancu, F., Potrzebowski, A., Akbari, P., Müller, N., and Piechna, J.** (2004). Numerical simulation of unsteady-flow processes in wave rotors. *2004 International Mechanical Engineering Conference, Anaheim, CA, ASME Paper IMECE2004-60973*.
- Frei, S.** (2004). *Performance and Driveability Optimization of Turbocharged Engine Systems*. Diss. ETH No. 15510, ETH Zürich, Switzerland.
- Guzzella, L. and Martin, R.** (1998). Das SAVE-Motorkonzept. *MTZ Motortechnische Zeitschrift, Vol. 59*.
- Guzzella, L. and Onder, C.** (2004). *Introduction to Modeling and Control of Internal Combustion Engine Systems*. Springer-Verlag, ISBN 3-540-22274-x.
- Guzzella, L., Wenger, U., and Martin, R.** (2000). IC-Engine Downsizing and Pressure-Wave Supercharging for Fuel Economy. *SAE Technical Paper, 2000-01-1019*.



- Gyarmathy, G.** (1983). How does the COMPRES<sup>®</sup> Pressure-Wave Supercharger Work? *SAE Technical Paper, 830234*.
- Gygax, J.** and Schneider, G. (1988). Betriebserfahrungen mit dem Druckwellenlader COMPRES im Opel Senator. *MTZ Motortechnische Zeitschrift, Vol. 49, No. 9*.
- Heywood, J.** (1988). *Internal Combustion Engine Fundamentals*. Automotive Technology Series. McGraw-Hill International Editions, I. Title, II. Series.
- Hiereth, H.** (1989). Car Tests with a Free-Running Pressure-Wave Charger – a Study for an Advanced Supercharging System. *SAE Paper 890453*.
- Hoepke, E.** (1988). COMPRES-Druckwellenlader von BBC in Dieselfahrzeugen. *MTZ Motortechnische Zeitschrift, Vol. 44, No. 9*.
- Hörler, H.** (1969). *Abschätzung der Verluste in Instationär-Gasdynamischen Kanal-Trommel-Drucktauschern*. Diss. ETH No. 4402, ETH Zürich.
- Iancu, F., Piechna, J., and Müller, N.** (2005). Numerical Solutions for Ultra-Micro Wave Rotors ( $U\mu$ WR). *35th AIAA Fluid Dynamics Conference, AIAA Paper 2005-5034, Toronto*.
- Janssens, J.** (1992). *Simulation of the Unsteady Non-homentropic Flow in Pressure-Wave Machinery using the Massflow Defect Concept*. Diss. University Leuven, Belgium.
- Jenny, E.** (1993). *Der BBC-Turbolader: Geschichte eines Schweizer Erfolgs*. Birkhäuser Verlag, ISBN 3-7643-2719-7.
- Krebs, R., Szengel, R., Middendorf, H., Fleiss, M., and Laumann, A.** (2005). Neuer Ottomotor mit Direkteinspritzung und Doppelaufladung von Volkswagen. *MTZ Motortechnische Zeitschrift, Vol. 66, No. 11*.
- Laney, C.** (1998). *Computational Gasdynamics*. Cambridge University Press, ISBN 0-512-57069-7.

- Lax**, P. and Wendroff, B. (1960). Systems of Conservation Laws. *Communications of Pure and Applied Mathematics, Vol. 13*: 217-237.
- Mayer**, A. (1981). COMPREX-Superchargers for Vehicle Diesel Engines. *Diesel and Gas Turbine Worldwide, Part 1, April 1981, Part 2, June 1981*.
- Mayer**, A. (1988). COMPREX-Supercharging eliminates Trade-off of Performance, Fuel Economy and Emissions. *SAE Technical Paper Series 881152, August 8-11*.
- Mayer**, A. and Kirchhofer, H. (1985). The COMPREX-Pressure Wave Supercharger in Passenger Car Applications. *International Journal of Vehicle Design, Vol. 6, No. 1, pp. 1-23*.
- Mayer**, A., Nashar, I., and Perewusnyk, J. (1990). COMPREX with Gas Pocket Control. *Institution of Mechanical Engineers (Great Britain), C405/032*.
- Meyer**, A. (1947a). Recent Developments in Gas Turbines. *Journal of Mechanical Engineering, 69, No. 4, pp. 273-277*.
- Meyer**, A. (1947b). Swiss Develop New Gas Turbine Units. *Electrical World, 127, pp. 38-40*.
- Nalim**, M. R. (2000). Longitudinally Stratified Combustion in Wave Rotors. *Journal of Propulsion and Power, 0748-4658, Vol. 16 No. 6, pp. 1060-1068*.
- Niederberger**, A. S. P. (2006). *Investigations of Thermoacoustic Oscillations: Modeling, Identification and Control*. Diss. ETH No. 16550, ETH Zürich.
- Pauli**, E. and Amstutz, A. (1989). Regelstrategie des COMPREX-aufgeladenen Dieselmotors zur Emissionsminimierung. *Sonderdruck MTZ, Motortechnische Zeitschrift*.
- Paxson**, D. E. (1995a). Comparison between Numerically Modeled and Experimentally Measured Wave-Rotor Loss Mechanisms. *Journal of Propulsion and Power, 0748-4658, Vol. 11 No. 5, pp. 908-914*.

- Paxson, D. E.** (1995b). A Numerical Model for Dynamic Wave Rotor Analysis. *Proceedings of the 31st Joint Propulsion Conference and Exhibit, San Diego, CA, July 10-12, 1995, AIAA-1995-2800.*
- Paxson, D. E.** (1996). Numerical Simulation of Dynamic Wave Rotor Performance. *Journal of Propulsion and Power, 0748-4658, Vol. 12 No. 5, pp. 949-957.*
- Pfiffner, R.** (2001). *Optimal Operation of CVT-Based Powertrains.* Diss. ETH No. 14136, ETH Zürich.
- Pfiffner, R., Weber, F., Amstutz, A., and Guzzella, L.** (1997). Modeling and Modelbased Control of Supercharged SI engines with Minimal Fuel Consumption. *Proceedings of the 16th American Control Conference - ACC, Albuquerque, NM.*
- Piechna, J.** (1998a). Comparison of Different Methods of Solution of Euler Equations in Application to Simulation of the Unsteady Processes in Pressure Wave Superchargers. *The Archive of Mechanical Engineering, Vol. XLV, Nr. 2 pp. 87-106.*
- Piechna, J.** (1998b). Numerical Simulation of the COMPREX Type of Supercharger: Comparison of Two Models of Boundary Conditions. *The Archive of Mechanical Engineering, Vol. XLV, No. 3, pp. 233-250.*
- Piechna, J., Akbari, P., Iancu, F., and Müller, N.** (2004). Radial-Flow Wave Rotor Concepts, Unconventional Designs and Applications. *2004 International Mechanical Engineering Conference, Anaheim, CA, ASME Paper IMECE2004-59022.*
- Piechna, J. and Lisewski, P.** (1998). Numerical Analysis of Unsteady Two-Dimensional Flow Effects in the COMPREX Supercharger. *The Archive of Mechanical Engineering, Vol. XLV, No. 4, pp. 341-351.*
- Real, R.** (1946). The 3000 kW Gas Turbine Locomotive Unit. *Brown Boveri Review, 33, No. 10, pp. 270-271.*

- Sauer, R.** (1960). *Einführung in die theoretische Gasdynamik*. Technische Hochschule München, dritte, verbesserte Auflage, Springer-Verlag.
- Schruf, G.** and Kollbrunner, T. (1984). Application and Matching of the COMPREX Pressure-Wave Supercharger to Automotive Diesel Engines. *SAE Paper 840133*.
- Seippel, C.** (1942). Drucktauscher, z.B. für Kältemaschinen. *Swiss Patent 229280*.
- Seippel, C.** (1946). Pressure Exchanger. *U.S. Patent 2,399,394*.
- Selerowicz, W.** and Piechna, J. (1999). COMPREX Type Supercharger as a Pressure-Wave Transformer-Flow Characteristics. *The Archive of Mechanical Engineering, Vol. XLVI, No. 1, pp. 57-77*.
- Sod, G.** (1985). *Numerical Methods in Fluid Dynamics*. Cambridge University Press.
- Soltic, P.** (2000). *Part-Load Optimized SI Engine Systems*. Diss. ETH No. 13942, ETH Zürich.
- Spring, P.,** Guzzella, L., and Onder, C. (2003). Optimal Control Strategy for a Pressure-Wave Supercharged SI Engine. *Technical Paper ICES2003-645, Proceedings of ICE03, 2003 Spring Technical Conference of the ASME Internal Combustion Engine Division, Salzburg*.
- Spring, P.,** Piechna, J., and Onder, C. (2004). Modeling and Validation of a Pressure-wave Supercharger using a Finite-difference Method. *2004 International Mechanical Engineering Conference, Anaheim, CA, ASME Paper IMECE2004-59533*.
- Tatsutomi, Y.,** Yoshizu, K., and Komagamine, M. (1990). Der Dieselmotor mit Comprex-Aufladung für den Mazda 626. *MTZ Motortechnische Zeitschrift, Vol. 51, No. 3*.

- Taussig**, R. and Hertzberg, A. (1984). Wave Rotors for Turbomachinery. *Winter Annual Meeting of the ASME, edited by J.F. Sladky, Machinery for Direct Fluid-Fluid Energy Exchange, AD-07, pp. 1-7.*
- Traupel**, W. (1988). *Thermische Turbomaschinen, thermodynamisch- strömungstechnische Berechnungen, Band 1.* Springer-Verlag.
- Weber**, F. (2001). *Mean Value Modeling of a Pressure-Wave Supercharger Including Exhaust Gas Recirculation Effects.* Diss. ETH No. 14265, ETH Zürich.
- Weber**, F. and Guzzella, L. (2000). Control Oriented Modeling of a Pressure Wave Supercharger. *SAE Technical Paper, 2000-01-0567.*
- Weber**, F., Guzzella, L., and Onder, C. (2002). Modeling of a Pressure Wave Supercharger Including External Exhaust Gas Recirculation. *IMECHE Journal of Automobile Engineering, Vol. 216, No. D3, pp. 217-235.*
- Woschni**, G. (1967). A Universally Applicable Equation for the Instantaneous Heat Transfer Coefficient in the Internal Combustion Engine. *SAE Trans., Vol. 76, No. 670931, pp. 3065-3083.*
- Woschni**, G. (1970). Die Berechnung der Wandverluste und der thermischen Belastung der Bauteile von Dieselmotoren. *MTZ Motortechnische Zeitschrift, Vol. 30, Nr. 12, pp. 491-499.*
- Wunsch**, A. (1970). Aufladung von Fahrzeugdieselmotoren mit dem Abgasturbolader und mit der Druckwellenmaschine Comprex. *MTZ Motortechnische Zeitschrift, Vol. 31, Nr. 1.*
- Zehnder**, G. and Mayer, A. (1984). COMPRES<sup>®</sup> Pressure-Wave Supercharging for Automotive Diesels – State of the Art. *SAE Paper 840132.*
- Zehnder**, G., Mayer, A., and Mathews, L. (1989). The Free Running COMPRES. *SAE Paper 890452.*

# Index

## Symbols

$\alpha_{cas}$ , 12, 89  
 $n_{pws}$ , 12, 89  
 $y_{gpv}$ , 12, 95  
 $y_{th1}$ , 12, 104  
 $y_{th2}$ , 12, 95

## A

abbreviations, xiii  
**abstract**, ix  
acronyms, xiii  
Amstutz curve, 78

## C

cause-and-effect diagram, 16  
    simplified, 24  
closed-loop simulation, 81  
comparison of supercharging devices, 4  
**conclusions**, 105  
conservation of  
    energy, 38, 119  
    energy (steady state), 123  
    mass, 38, 117  
    mass (steady state), 122  
    momentum, 38, 118  
    momentum (steady state), 123  
contents, vi  
contributions of the thesis, 20  
control  
     $n_{pws}$ ,  $\alpha_{cas}$ , 89  
     $y_{th1}$ , 104  
     $y_{th2}$ ,  $y_{gpv}$ , 95  
    driveability, 95  
    efficiency, 89  
    emissions, 104  
    **control system design**, 87  
controller I  
    design, 89  
    realization, 89  
    scheme, 91

    verification, 92

controller II  
    design, 95  
    realization, 96  
    scheme, 98  
    verification, 99

controller III  
    design, 104  
    scheme, 104

conventions  
    abbreviations, acronyms, xiii  
    capitalizations, xix  
    derivatives, xix  
curriculum vitae, 141  
CX64, 109  
    technical data, 111

## D

downsizing and supercharging  
    chart, 3  
    concept, 1  
driveability, 4, 15, 17, 95  
DT1 element, 96

## E

EA111/HX95, 109  
    closed-loop simulation, 81  
    modeling, 23  
    technical data, 111  
EGR  
    definition, 6  
    influence on engine torque, 32  
    model, 76, 77  
    rate versus scavenging rate, 32  
    rate, definition, 76, 113  
    typical load steps, 18  
engine  
    technical data, 111  
    test rig, 109  
engine system

- cause/effect diagram, 16
- control-oriented structure, 13
- description, 10, 11
- general structure, 10
- input/output behavior, 17
- modeling, 23
- simplified cause/effect diagram, 24
- typical load steps, 18
- engine system modeling
  - engine mass flow, 29
  - engine outlet temperature, 33
  - engine torque model, 30
  - flow restriction, 27
  - general remarks, 23
  - intercooler, 29
  - overview, 23
  - receivers, 25
- Euler equations, 39
  - derivation, 117
- experiments
  - experimental setup**, 109
  - reference data, 111
- experiments, test bench engine, 110

## F

FDMdl

- boundary conditions, 43
- dispersion errors, 43
- finite-difference modeling**, 37
- governing equations, 37
- h-s diagram, 48
- input/output definitions, 59
- leakage mass flows, 55
- left boundary conditions, 45
- pressure distribution, 50
- results, 49
- sensitivities
  - versus fitting parameters, 54
  - versus pressures, 53
  - versus temperatures, 54
- space-time discretization, 40
- temperature distribution, 51
- validation, 57
  - with EA111/HX95, 60
  - with SAB360/CX64, 61

## G

- GOL, 109
  - picture, 110

## H

- HX95, technical data, 111

## I

- ideal gas law, 38, 122
- introduction, 1
  - contributions of the thesis, 20
  - DS concept, 1
  - engine system, 11
  - model-based control, 11
  - motivation of the thesis, 20
  - PWS, 7
  - structure of the thesis, 22

## L

- Lax-Wendroff method, 40
  - space-time grid, 41
- leakage, 55
- linear wave theory
  - derivation, 121
  - governing equations, 121
  - summary, 64

## M

- mass flows
  - chart, 14
  - definitions, 13
- mechanical supercharger, 2
- model
  - engine mass flow, 29
  - engine outlet temperature, 33
  - engine torque, 30
  - flow restriction, 27
  - general remarks, 23
  - intercooler, 29
  - overview, 23
  - PWS, 35
  - PWS (FDMdl), 37
  - PWS (MVMdl), 63
  - receiver, 25
  - Willans line, 31
- motivation of the thesis, 20
- MVMdl



- “Amstutz curve”, 78
- EGR effects, 76
- high-pressure part, 68
- linear wave theory, 64
- mean-value modeling**, 63
- polytropic exponent, 65
- six basic modes, 69
- validation with EA111/HX95, 71

## N

- nomenclature, xiii
  - abbreviations, acronyms, xiii
  - capitalizations, xix
  - derivatives, xix
  - subscripts, xvii
  - symbols, xv

## O

- outlook, 105

## P

- PWS
  - finite-difference modeling, 37
  - introduction, 7
  - mean-value modeling, 63
  - modeling, 35
  - schematic overview, 9
- PWS modeling, 35

## R

- reference data, 111

## S

- SAB360, 109
  - FDMdl validation, 61
  - technical data, 111
- Sankey diagram, 14
- SAVE, 109
- scavenging
  - definition, 9
  - four phases, 86
  - mass flow, definition, 112
  - process, 79
- scavenging rate
  - definition, 112
- shock equations, derivation, 123
- simulation

- closed-loop, 81
  - results, 82, 83
- speed of sound, derivation, 129
- structure of the thesis, 22
- subscripts, xvii
- superchargers
  - comparison, 4
  - driveability, 4
  - efficiency, 2
- symbols, xv

## T

- table of contents, vi
- technical data, 111
- test rig, picture, 110
- transient EGR, 18
- turbocharger, 2, 109
- typical load steps, 18

## V

- VW GOL, 58, 109, 110

## W

- Willans line, 31

## Z

- Zusammenfassung, xi



# Curriculum Vitae

## Personal Data

Name: Peter Spring  
Date of birth: June 2, 1973  
Parents: Eduard and Vreni Spring-Eicher

## Education and Experience

|           |   |
|-----------|---|
| 1980–1984 | Primary school in Reutigen BE, Switzerland  |
| 1984–1989 | Secondary school in Wimmis BE, Switzerland  |
| 1989–1993 | Gymnasium in Thun BE, Switzerland   |
| 1993      | Matura certificate, type C  |
| 1993–1994 | Military service  |
| 1994–1999 | Studies in Mechanical Engineering, ETH Zürich, Switzerland  |
| 1999–2000 | Diploma thesis at <i>LuK Getriebesysteme GmbH</i> , Bühl, Germany. Subject: Vehicle modeling for hardware-in-the-loop testbench |
| 2000      | Diploma (M.S.) as <i>Dipl. Masch.-Ing. ETH</i>  |
| 2000–2006 | Doctoral student, teaching and research assistant at the Measurement and Control Laboratory, ETH Zürich, Switzerland            |